Sap Flow and Heat Transport in Trees: An Asymptotic and Numerical Study

by

Bebart Maisar Janbek

B.Sc., University of Jordan, 2000
M.Sc., University of Jordan, 2003

Thesis Submitted in Partial Fulfillment of the
Requirements for the Degree of
Doctor of Philosophy

in the
Department of Mathematics
Faculty of Science

© Bebart Maisar Janbek 2017
SIMON FRASER UNIVERSITY
Fall 2017

All rights reserved.
However, in accordance with the *Copyright Act of Canada*, this work may be reproduced without authorization under the conditions for "Fair Dealing." Therefore, limited reproduction of this work for the purposes of private study, research, education, satire, parody, criticism, review and news reporting is likely to be in accordance with the law, particularly if cited appropriately.

Approval

Name:	**Bebart Maisar Janbek**
Degree:	**Doctor of Philosophy (Mathematics)**
Title:	***Sap Flow and Heat Transport in Trees: An Asymptotic and Numerical Study***
Examining Committee:	**Chair:** Paul Tupper Professor

John Stockie
Senior Supervisor
Professor _____

Weiran Sun
Supervisor
Assistant Professor _____

David Muraki
Internal Examiner
Professor _____

Huaxiong Huang
External Examiner
Professor
Department of Mathematics and Statistics
York University _____

Date Defended: October 12, 2017

Abstract

Transport of fluid and heat inside a tree, and the interchange of water and energy between the tree and the environment, are topics that have been and continue to be areas of active research in plant physiology, agriculture and environmental studies. Many models have been proposed to describe the flow of sap inside the tree, and to connect it to the driving transpiration rate, with various levels of complexity, and with different levels of abstraction. Most existing models are 1D models and many only attempt to get numerical results, without much analysis. For our work, we adopt a porous medium model that has been verified experimentally [Chuang et al., Ecological Modelling, 191(3):447-468, 2006]. We generalize this 1D model to a 3D axisymmetric geometry, where flow is transpiration driven and has anisotropic and spatially dependent hydraulic conductivity. Through asymptotic analysis, we derive approximate solutions that produce the axial and radial trunk sap fluxes for a given transpiration function. We validate the analytical solutions using a second order finite difference scheme. Next we use our solution formulas to tackle the inverse problem of determining spatial and temporal components of transpiration given a discrete set measurements of the trunk sap flux. Finally, we compare our results to some experimental data on radial variations of sap flux.

As for the heat transport problem, previous work related to trees discuss special cases of the problem, while giving detailed accounts and specific formulas of the boundary conditions, like wind and solar radiation effects. Most of this work does not include the possible effects of advection owing to sap flux, and does not discuss the effects of spatial variation in saturation on the thermal diffusivity. Assuming local thermal equilibrium for porous media, we propose a simple advection-diffusion model, with general boundary conditions, and derive Fourier-Bessel series solutions for the various possible cases suggested by dimensionless parameters.

Keywords: tree sap flow; heat transport; porous medium model; 3D axisymmetry; partial differential equations; asymptotic analysis; inverse problem; advection-diffusion; series solution

Dedication

To my parents Maisar and Nisrin, for whom I owe everything.

Acknowledgements

First, I would like to thank my supervisor for his infinite patience during my PhD program, especially for allowing me some room to develop in areas outside my thesis topic. I would like to thank Dr. David Muraki for helpful hints that started me on the asymptotic analysis of the sap flow problem. I would also like to thank Dr. Weiran Sun for some helpful ideas for the heat flow section.

Table of Contents

Approval ii

Abstract iii

Dedication iv

Acknowledgements v

Table of Contents vi

List of Tables ix

List of Figures x

I Sap Flow 1

1 Introduction 2

1.1 Sap Ascent . . . 2

1.2 Tree Hydraulic Transport Physics . . . 4

1.3 Biology and Tree Anatomy . . . 5

1.4 Review of Mathematical Models for Sap Flow . . . 6

2 Governing Equations 8

2.1 Chuang's Model . . . 8

2.2 Measurement Units . . . 10

2.3 Axisymmetric Model for Sap Flow in a Tapered Cylinder . . . 11

2.4 Coefficient Functions from Chuang et al. . . . 14

3 Numerical Method 19

3.1 Coordinate Transformation . . . 19

3.2 Finite Difference Discretization . . . 20

3.3 Validation of Numerical Scheme . . . 23

4 Asymptotic Series Solution 24

4.1 Nondimensionalization . . . 25
4.2 Asymptotic Expansion for the General Case . . . 28
4.3 Constant Transpiration, Steady State Solution: Connection with Circuit Models . . . 31
4.4 Time Periodic Transpiration Constant Scalar Conductivity . . . 32
4.5 Steady State, Constant Transpiration and Constant Scalar Conductivity . . . 36
4.6 Numerical Validation . . . 38
4.7 Heartwood Region . . . 41
4.8 Interpretation and Measurement of Dimensionless Parameters . . . 41
4.8.1 Relaxation Time . . . 42
4.8.2 Physical Relevance of the Dimensionless Parameters and Order of Magnitude Relationships . . . 42
4.8.3 Parameter Estimation . . . 44
4.9 Additional Special Cases . . . 44
4.9.1 Anisotropic Hydraulic Conductivity . . . 44
4.9.2 Case $\eta \not\sim 1$ . . . 49
4.9.3 Branching from Tree Crown . . . 49

5 The Inverse Problem: Estimating Transpiration from Sap Flux Measurements 53
5.1 Measurements of Relevant Physical Quantities . . . 53
5.2 Deriving the Linear Algebraic System . . . 54
5.3 Optimizing to Determine the Transpiration Function . . . 56

6 Experimental Verification 60
6.1 Norway Spruce . . . 60
6.2 Douglas fir . . . 60

7 Conclusion 64
7.1 Future Work . . . 64

II Heat Transport 66

8 Background: Heat Transport in Trees 67

9 Governing Equations for Heat Transport 70
9.1 Boundary Conditions . . . 70
9.2 Model for Heat Advection-Diffusion in a Tree with Spatially Dependent Saturation . . . 73
9.3 Non-Dimensionalized Heat Transport Equations . . . 77

10 Fourier-Bessel Series Solutions **80**
10.1 Steady Heat Transport with Constant Transpiration 80
10.1.1 Advection and Diffusion Comparable in Magnitude 82
10.1.2 Advection Dominated Heat Transport 87
10.1.3 Diffusion Dominated Heat Transport 91
10.1.4 Comparing the Three Cases 91
10.2 Time Varying Cases Asymptotic Analysis 92
10.2.1 Advection-Diffusion with Time-Dependent Boundary Conditions . . 92
10.2.2 Diffusion-Dominated Heat Transport with Time-Dependent Boundary Condition 94
10.3 Saturation Dependent Thermal Diffusivities 97

11 Numerical Simulations **98**
11.1 Brief Algorithm Description 98
11.2 Numerical Verification of Asymptotics 98
11.3 Large Variation of Vertical Velocity 99

12 Conclusion **103**

Bibliography **104**

Appendix A Correction Term for the Advection-Diffusion Case **109**

List of Tables

Table 2.1 Variables and parameters used in the governing equations. Values are for the "base case" used in the asymptotic analysis, while certain parameters from additional simulations are given in square brackets. . . 9

Table 3.1 Grid refinement study. The order of convergence is estimated as the base-2 logarithm of the ratio of successive grids errors. Errors are estimated based on the solution from a 500×500 grid. 23

Table 9.1 Variables and parameters used in the governing equations for the heat transport problem. Any parameters not listed here are instead in Table 2.1. 74

List of Figures

Figure 1.1 Water transport in the xylem [70]: water moves through the tracheids and the vessel elements in the xylem to the leaves. The water encounters much less resistance in the vertical direction than in the radial direction where it has to move through the pits. 3

Figure 1.2 Stem anatomy [71] with the non-conductive heartwood and the conductive sapwood (mostly comprised of xylem tissue). 3

Figure 2.1 The left figure shows the tree trunk and its sapwood as a tapered annular cylinder (exponentially decaying radius case). The right figure shows a vertical cross section with the boundary conditions for the sap flow model. 11

Figure 2.2 (a) Transpiration vertical profile function $f(z)$ specified in (2.17) (b) leaf transpiration flux function $E(t)$ specified in (2.15). Both functions are used in most of the simulations for the sap flow (unless otherwise indicated), with $E_0 = 3.94 \times 10^{-8}$, $\alpha = 1.42$ and $\gamma = 0$, and the rest of the parameters as shown in Table 2.1. 16

Figure 3.1 Discrete grid point locations in transformed coordinates, with points indexed as (r_i, z_k). Saturation is approximated at cell centers (red circles) and velocity components on cell edges (blue triangles). The discrete equations involve saturations at cell corners (magenta diamonds, approximated using an average of cell-centered values) so that the difference equations for $ds_{i,k}/dt$ correspond to a full nine-point stencil involving the neighbouring saturation points denoted in red. 21

Figure 4.1 Comparison between numerical (plots) and asymptotic estimates (formulas) of relaxation times given by (4.54) and spatial travel between $z = 0.5z_0$ and $z = 0.8z_0$ in (4.47) for a transient disturbance at the top of the tree ($E_0 = 3.94 \times 10^{-8}$, $\kappa = 1$, $a = 1.42$ and $\gamma = 0$). (a) Shifted and rescaled version of original $f(z)$ so that the leaves are concentrated at the upper portion of the tree. (b) Transient disturbance $E(t)$ corresponding to an extreme weather event. (c) Saturation variation as the transpiration is changed with time for $\eta = 4.77$: at $t = 0$ the tree is fully hydrated with no transpiration, at $t = 1$ days constant transpiration is applied, and at $t = 3$ days a Fourier mode $m = 1$ is applied. (d) Zoomed portion of (c) showing the relaxation from zero transpiration to positive transpiration. (e) Zoomed portion of (c) showing the shift in time between two corresponding peaks at two heights. (f) Similar to (e) but for the case of $\eta = 14.3$ (obtained by scaling r_0, z_0 and ψ_o by 3). 37

Figure 4.2 Asymptotic and numerical solutions for constant transpiration and isotropic conductivity. (a,b) Comparison of vertical velocity v_z and saturation s (both are averaged across the radius). (c) Log ratio of the velocity components, $\log_{10}|v_r/v_z|$. (d) Velocity field arrows and flow streamlines. Parameters are chosen as in Table 2.1 with $E(t) \equiv E_o = 3.94 \times 10^{-8}$, $\kappa = 1$, $\alpha = 1.42$ and $\gamma = 0$; the asymptotic result is based on the first two terms in the steady-state solution for the isotropic case $\kappa = 1$. 39

Figure 4.3 L1-norm of difference between numerical and asymptotic solutions relative to the numerical solution within the asymptotic regime where $\mu \sim \phi \sim \zeta \sim \delta$ 40

Figure 4.4 Saturation (s) profiles during a 24-hour period, showing the horizontally-averaged numerical solution and asymptotic approximation. For purposes of clarity the profiles over one daily cycle are separated into two roughly 12-hour periods (a,b), since the saturation decreases over the first half day after which it increases again. Here the stem has a taper $\alpha = 1.42$ and a transpiration flux average $E_0 = 3.94 \times 10^{-8}$ (with $\kappa = 1$ and $\gamma = 0$). 40

Figure 4.5 Simulations of radial velocity v_r (SI units) shown at various times throughout a diurnal cycle at the middle of the sapwood region, $r = R(z)(\gamma + 1)/2$. Results are shown for three values of heartwood fraction $\gamma = 0, 0.5, 0.75$ and other parameters as in Table 2.1 except $\kappa = 1$. 41

Figure 4.6 Effect of anisotropy for (a) $\kappa = \zeta$, (b) $\kappa = \zeta^2$ on the computed radially-averaged saturation during a diurnal cycle in a tapered stem with $\alpha = 1.42$, $E_0 = 3.94 \times 10^{-8}$ and $\gamma = 0$. 45
Figure 4.7 Effect of anisotropy ($\kappa = 1$, ζ, ζ^2) on the computed velocity in a non-tapered stem with $\alpha = 0$ and $\gamma = 0$. The vertical velocity profiles are simulated numerically using a constant transpiration rate $E_0 = 3.9375 \times 10^{-8}$, and depicted at heights labelled A–E on the left plot of Figure 2.2. 48
Figure 4.8 Same as Figure 4.7 for a tapered stem with $\alpha = 1.42$. 48
Figure 4.9 Transpiration flux spatial dependence function $f(z)$ resulting from the modification (4.57) for a non-tapered stem with $\alpha = 0$ and $\gamma = 0$. The time constant transpiration rate is $E_o = 3.94 \times 10^{-8}$. 50
Figure 4.10 Effect of anisotropy ($\kappa = 1$, ζ, ζ^2) on the computed velocity in a non-tapered stem with $\alpha = 0$ and $\gamma = 0$. The vertical velocity profiles are simulated numerically using a constant transpiration rate $E_o = 3.94 \times 10^{-8}$, and depicted at heights labelled A–E on Figure 4.9. The curves for heights A–C are superimposed for the left and middle plots. 51
Figure 4.11 Effect of anisotropy ($\kappa = 1$, ζ, ζ^2) on the computed velocity in a non-tapered stem with $\alpha = 0$ and $\gamma = 0$. The radial velocity profiles are simulated numerically using a constant transpiration rate $E_o = 3.94 \times 10^{-8}$, and depicted for $f(z)$ in Figure 4.9. 52

Figure 5.1 (a) transpiration vertical profile function $f(z)$, (b) leaf transpiration flux function $E(t)$ (right). We start from a known $f(z)$ and $E(t)$ (red), we then add 3% noise and attempt to recover the functions (blue). 58
Figure 5.2 (a) transpiration vertical profile function $f(z)$, (b) leaf transpiration flux function $E(t)$ (right). We start from a known $f(z)$ and $E(t)$ (red), we then add 10% noise and attempt to recover the functions (blue). 59

Figure 6.1 Comparison of 3D numerical simulations with the experimental data in Chuang et al. [12] for Norway spruce. Vertical sap flux from simulations (Sim) and experiments (Exp) at two different times, converted to SI units. 61

Figure 6.2 Average axial pressure gradient (calculated between the bottom and top of the tree) versus the radial pressure gradient simulation results at $z = 1$ m through a diurnal cycle, for parameter values (a) $K_z = 3.22 \times 10^{-5}$ and $K_r = 1.13 \times 10^{-8}$ [19], and (b) one tenth of these values. Hourly pressure gradients up till noon (blue circles) and in the afternoon (red circles). Note the clockwise cycle (not as prominent in the left plot). 63

Figure 6.3 Experimental results from Domec [19] at two different days with the similar parameter values as the ones used to generate Figure 6.2. . 63

Figure 9.1 (a) Diffusivity saturation dependence for the radial/angular $D_r = D_\theta$ (blue) and vertical D_z (red) diffusion components, using formulas (9.9) and (9.8) and the values in Table 9.1. (b) Zoom in of the radial/angular diffusivity which varies over a much small range than the vertical diffusivity. 75

Figure 9.2 The boundary conditions for the heat transport problem: the Dirichlet boundary condition at the bottom, and the outgoing heat fluxes from the lateral side and the top of the tree. The upper boundary condition will be dropped out from our model when considering the asymptotic solutions. 76

Figure 10.1 Steady state temperature distribution for the advection-diffusion case, for an axisymmetric lateral heat flux $W(z) = 1/2\,(1 + \cos(\pi(z-1)))$ and a Dirichlet bottom boundary temperature $N = J_0(\gamma_0)$. Here $W_0 = 100, 200, 400$ (left to right), $N_0 = 1$, $h = 5, 10, 20$, $k = 0.32$, $r_0 = 0.129/2$, $z_0 = 6.7$, $M_2 = 1$. Here the lowest eigenvalue $\gamma_0 = 1.26, 1.60, 1.91$. $r_0 h/k = 1.01, 2.02, 4.03$. This simulates the sun affecting the upper part of the tree. 87

Figure 10.2 Steady state temperature distribution for the advection-diffusion case, for an axisymmetric lateral heat flux $W(z) = 0$ and a Dirichlet bottom boundary temperature $N = J_0(\gamma_0)$. Here $W_0 = 0$ (left to right), $N_0 = 5$, $h = 5, 10, 20$, $k = 0.32$, $r_0 = 0.129/2$, $z_0 = 6.7$, $M_2 = 1$. Here the lowest eigenvalue $\gamma_0 = 1.26, 1.60, 1.91$. $r_0 h/k = 1.01, 2.02, 4.03$. 88

Figure 10.3 Steady state temperature distribution for the advection-diffusion case, for the lateral heat flux $W(\theta, z) = 1/2\,(1 - \cos(\pi z))\cos(\theta)$ and a Dirichlet bottom boundary temperature $N = r^2 W(\theta, 0)$. Here $W_0 = 100, 400$ (left to right), $N_0 = C_0 u_0$ (so that $\tilde{N} = 0$), $h = 5$, $k = 0.32$, $r_0 = 0.129/2$, $z_0 = 6.7$, $M_2 = 1$. Here the lowest eigenvalue $\gamma_0 = 1.26, 1.91$. $r_0 h/k = 1.01, 4.03$. (top) Horizontal cross-sections at $z = jz_0/8$ for $j = 1, ..., 8$. (bottom) vertical cross-sections at $\theta = j\pi/8$ for $j = 0, 1, ..., 7$. 89

Figure 10.4 Steady state temperature distribution for the advection-diffusion case, for the lateral heat flux $W(\theta, z) = 1/2\,(1 - \cos(\pi z))\cos(\theta)\cos(2\pi t)$ and a Dirichlet bottom boundary temperature $N = r^2 W(\theta, 0)$. $W_0 = 100$, $N_0 = C_0 u_0$ (so that $\tilde{N} = 0$), $h = 5$, $k = 0.32$, $r_0 = 0.129/2$, $z_0 = 6.7$, $M_2 = 1$, $M_0 = 1$. The lowest eigenvalue $\gamma_0 = 1.26$. $r_0 h/k = 1.01$. (a) Horizontal cross-section at $z = z_0/2$. (b) Vertical cross-sections at $\theta = 0$. We assume that the initial transient behaviour has passed, and we are in a time periodic regime. 95

Figure 11.1 Numerical solution when $\chi = 0$ for the time varying $W = 1/2\,(1 - \cos(2\pi z))\sin(2\pi t)$ and $N = 0$. 99

Figure 11.2 Difference between numerical and asymptotic solutions relative to the numerical solution when $\chi = 0$ for the time varying $W = 1/2\,(1 - \cos(2\pi z))\sin(2\pi t)$ and $N = 0$. 100

Figure 11.3 L1-norm of difference between numerical and asymptotic solutions relative to the numerical solution when $\chi = 0$ for the time varying $W = 1/2\,(1 - \cos(2\pi z))\sin(2\pi t)$ and $N = 0$. 100

Figure 11.4 Vertical velocity component profile for $\chi = 1$ case. This represents the situation where there is a larger leaves concentration at the lower part of the tree. 101

Figure 11.5 Effect of large variations in vertical velocity profile ($\chi = 1$) on temperature distribution time variation for the advection-diffusion case ($M_3 = 1$). 102

Part I

Sap Flow

Chapter 1

Introduction

1.1 Sap Ascent

Transport of sap in trees is a problem that has puzzled scientists and plant physiologists for a long time. In particular, "the ability of trees to suck water from the soil to the roots, through the stem to the leaves, sometimes to heights of over a hundred meters, is remarkable given the absence of any mechanical pump" [8]. The short version of the most widely available explanation goes as follows [63]: water is lost from the leaves as an unintended consequence of the shared path between diffusion of the essential precursor for photosynthesis (CO_2) from the atmosphere into the leaves, and the water evaporation and diffusion from leaves to the atmosphere due to the vapour pressure deficit. As water evaporates from the leaves, the water-air interface retreats into the hydrophilic leaf cell wall interstices, where it is highly curved and thus has a high surface tension. This tension force is in turn transmitted through the water continuum to the xylem in the branches and stem (see Figures 1.2 and 1.1), and subsequently to the roots, thus creating the force necessary to pull sap from the roots to the leaves [50]. Part of this water is provided from the internal capillary storage of the tree during the day [72, 23], especially when there is a high evaporative demand; this storage is replenished during the night when transpiration is at a minimum. Sometimes the tension is so high that it causes air to leak into the tracheids in the xylem, thus causing an embolus to form. The compartmentalization and redundancy of the tree vascular system helps in isolating these emboli and providing alternate routes for sap flow [15]. Trees have different ways of mitigating the effects of embolism: one mechanism is to create a local pressure to dissolve the embolus, while another is to grow new conductive tissue during the subsequent growth season.

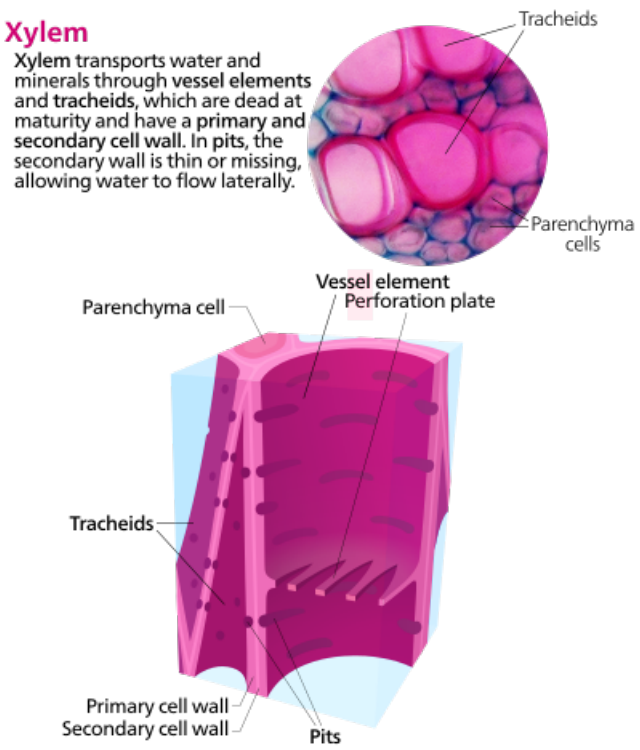

Figure 1.1: Water transport in the xylem [70]: water moves through the tracheids and the vessel elements in the xylem to the leaves. The water encounters much less resistance in the vertical direction than in the radial direction where it has to move through the pits.

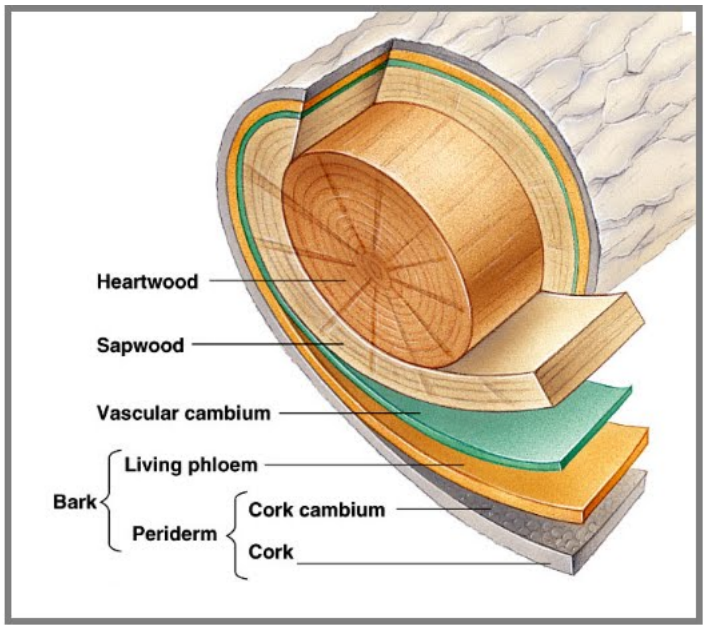

Figure 1.2: Stem anatomy [71] with the non-conductive heartwood and the conductive sapwood (mostly comprised of xylem tissue).

1.2 Tree Hydraulic Transport Physics

Many forces are related to the hydraulic flow of sap in the tree. First, note that sap exists under negative pressure in the stem, so that in order for the sap to flow in the xylem, the cohesive forces that bind water molecules together should be strong enough to withstand the transpiration pull effect. Indeed, pure water can withstand very high tension forces of the order of $10 - 100$ [MPa], well above the forces that exist in plants [54]. These same cohesion forces are responsible for surface tension force, which is relevant wherever a water-air interface exists in constricted spaces; the pressure difference across a meniscus owing to surface tension has the form

$$P_T = \frac{\gamma}{R_M},$$

where γ [N/m] is the surface tension in the leaves, and R_M [m] is the meniscus radius. As water recedes into the mesophyll cell walls in the leaves, the resulting surface tension force is enough to pull water upward from the roots even in the tallest trees. This force also acts in the tracheids especially in the pit margo where it prevents air movement from embolized tracheids into neighbouring tracheids, thus maintaining sap flow. This force may also explain the form of the pressure-saturation relationship near full saturation: as residual water in embolized tracheids is gradually lost, the water-air interface recedes into the tapering ends of the tracheid, thus creating more resistance to loss.

Another force at play is gravitational force, which is especially important in tall trees. Yet another force that is relevant here is the elastic force, which acts in the tracheids and prevents them from collapsing under tension force; this force also acts in the trunk within living cells such as parenchyma cells and in the bark because the elasticity of cell walls acts against osmotic forces (this may be a factor in the pressure-saturation relationship, especially in angiosperms). Osmotic forces act in the roots, where the active concentration of minerals in the stele creates an osmotic pressure difference between the soil and root, which may be relevant for transport to leaves in smaller plants; the same force acts between xylem and phloem, where the active loading of sugars in the phloem creates a pressure difference that drives sugar transport.

Finally, note that the vapour pressure difference between the vapour saturated air space inside the leaves and outside air is the driving force for transpiration.

To summarize, we consider trees that are tall enough so that the osmotic push from the roots is insignificant, and for which the gravitational effects are significant. We discard details of the interaction of xylem conductive tissue with other tissues in the trunk, and use instead empirically derived relationships between the pressure and saturation. In our model, we do not consider the effect of growth, although this may be relevant on longer time scales. Nor do we consider the coupling between flow in the xylem and phloem. Elastic forces in the tracheid wall are neglected because the wall is stiff (due to lignification), and

thus these forces do not affect the flow volume. We neglect details of the leaves' interaction with the surrounding air and instead consider the outflow rate as a given, similar to Chuang et al [12]. In fact, our outflow boundary condition is specified on the trunk boundary so that the branches are not explicitly included as part of the model geometry. Finally, we do not consider high tensions or large deviations from full saturation at which embolism form since this is not always a reversible process and its mechanism is still not well understood [7].

1.3 Biology and Tree Anatomy

We will focus on conifers in explaining the concepts at play in our model, as they have a simpler architecture as porous media, which is a central central feature of the model we will adopt for sap flow. This can be seen in the simplicity of the conductive tissue, which is mainly constructed of tracheids, with rare occurrences of parenchyma and other cell types, as shown in Figure 1.1. The tracheids are dead longitudinally-oriented cells, that are comprised of a cell wall and an empty lumen; they are connected to each other through pits (small pores) that allow water conduction but restrict the movement of air from embolized neighbouring tracheids (due to high surface tension forces that need to be overcome). The distribution of pits in the cell wall are such that the hydraulic conductivity in the longitudinal direction is orders of magnitude higher than in the radial direction [13, 53]. Some tracheids may be embolized and this is hypothesized [72] to act as a water storage, thus the concept of capacitance comes into play. The tracheids taper at both ends, and as water is lost from an embolized tracheid, it recedes into the tapered ends so that the surface tension force increases until it balances the negative pressure in neighbouring tissue (which decreases in magnitude due to released water from the embolized tracheid). When the pressure in neighbouring tissue increases, the water enters the embolized tracheids and the water-air interface surface tension decreases until it balances the new neighbouring pressure. This process is reversible although there is the slow dynamics of air dissolving in water and air released from water until it reaches zero pressure (atmospheric pressure). Cavitation is another mechanism that releases water into the transpiration stream, although it is less reversible and usually occurs under more severe conditions like drought of freezing, when the tension is too high to overcome the pit resistance to embolism. For example, in severe drought the transpiration demand is high while the soil water supply is deficient, which causes high water tensions to develop inside the stem enough to overcome the air-water surface tension in the pits and release the water in the cavitated tracheid (vessel) to the transpiration stream. In any case, the experiments of [65] provide support to the hypothesis of [72] that the embolized tracheids act as water storage compartments. In these experiments, the authors of [65] noticed that upon severely dehydrating conifer stem segments and then fully re-hydrating them, there was a higher water release per unit change in pressure

during subsequent tension application. This indicates that at the end of the dehydration-rehydration cycle there was a higher percentage of embolized tracheids that were able to act as water storage compartments. Moreover, the authors found that cavitation which is associated with acoustic emissions in the experiments, is rare at pressure tensions in a range of 0-2 [MPa] for the stems of the coniferous trees Thuja (cypress) and Tsuga (hemlock), which means that there is a large pressure range over which embolism formation can be ignored. Finally, it is worth noting that the concavity of the pressure saturation curves in [65] implies an ever decreasing amount of water release per unit decrease in pressure near full saturation.

The controversy surrounding embolism repair in conifers is discussed in [7]; the issue of whether embolism repair happens, and in which trees it occurs, is still not settled. If embolism occurs in conifers, it is probably not very successful because there is permanent loss of conductivity (for example, in the heartwood). Thus, in our work, we will assume that embolism is irreversible. Note that due to the stiffness of the lignified tracheid wall (which means that the geometry of the tracheid is fixed), the hydraulic conductivity of a tracheid is not expected to change until an embolism occurs. Since we consider only changes close to full saturation where embolism is not expected to occur, and since we are assuming that there is no embolism repair, the hydraulic conductivity is assumed to be independent of saturation and time; therefore, we only assume a given spatial variation in conductivity, which is due to previously embolized tracheids.

One more thing to note is that even though we restrict discussion for the most part to conifers, the model is applicable to other trees like angiosperms, although in this case we are not able to justify some of our model assumption as easily in terms of the anatomy and physiology; for example, water storage may be localized in the living tissue of the bark, or in the pith [23]. Another problem is the complexity of the tissue, which may consist of vessels, tracheids, fibers or even living parenchyma cells.

1.4 Review of Mathematical Models for Sap Flow

Many models have been proposed to explain the hydraulic phenomena occurring in trees such as the lag between transpiration and sap flow and the low pass filter action on the transpiration by the trunk flow. Some models [69, 37, 60] treat the tree stem using an electrical circuit analogy, as consisting of several electrical components connected in series and parallel, including resistors for the reciprocal of hydraulic conductivity, capacitors for water storage, inductors for momentum changes [55], voltages for pressures, and currents for sap velocities. The authors in [60] include stem growth and diurnal variations into their circuit model. These models are easy to apply but they have 3 main deficiencies. First, they are usually discrete models that lack spatial resolution. Second, they assume that capacitance, which is related to the storage capacity of the tree, is a constant. Third, they

require fitting of a typically large number of artificial parameters representing fictitious circuit components rather than actual hydrodynamic or physical parameters that represent the actual hydraulic properties of a tree and are more of computational models, that do not aid in understanding the flow problem.

Another class of models are the porous medium models in which the tree stem is assumed to be a porous medium typically governed by a partial differential equation (PDE) [12, 1], with a spatially dependent saturation or pressure, and with variable capacitance or nonlinear pressure-saturation relationship. These models range in complexity from simple macroscale models [12, 6] to more complex microscale models that include water-air interface dynamics [1, 2]. In terms of the geometry, some models only consider a 1D stem domain [12] while others consider also tree branches [6, 22] (it is worth mentioning that [22] assumes that the hydraulic conductivity decreases irreversibly due to cavitation). All these models consider individual trees, while at least one model tries to scale what is learned by considering each tree as a porous medium to forest scale [44]. Finally, the authors of [21] leverage their ability to acquire high resolution images of wood vessel structure to run detailed two phase Lattice-Boltzmann flow simulations. In general, these models are usually simulation based and no analysis has been performed on the model equations to aid in understanding. Second, the models are usually 1D and only consider vertical variations ignoring sometimes important variations in the radial direction.

In our work, we extend the model of Chuang et al. [12] to a more general 3D model of a tree trunk with axisymmetry, including radial variations in the model variables and the radial component of the sap velocity. This allows us to see the effects of anisotropy in the hydraulic conductivity on the model variables. We also perform a thorough asymptotic analysis of the model, connecting sap flow and saturation inside the tree trunk to the transpiration flux from the trunk surface. We analyze the forward problem of determining the sap flow in the trunk given the transpiration flux from the leaves. Then we use the resulting formulas to solve the inverse problem of determining the transpiration flux (both the spatial and temporal components) given a discrete set of measurements of the sap flow inside the trunk. Throughout, we use a finite difference numerical scheme to solve the governing equations, which serves two purposes: to verify our asymptotic analysis, and to consider cases for which we are not able to obtain an asymptotic solution.

Chapter 2

Governing Equations

In this chapter, we state the model equations and boundary conditions for sap flow in a tapered cylinder. We start with the model equations for the 1D case in Section 2.1 which were derived in Chuang et al. [12] for Norway spruce and verified experimentally. We extend the model to the case of a 3D axisymmetric tree stem with taper in Section 2.3, that incorporates the radial variations within the stem. We do this extension in a way that replicates the 1D model vertical variations in the vertical component of velocity and saturation, thus maintaining the link to the experimental results in [12], while also providing insight into the radial variations in velocity (both radial and vertical components) and saturation. Finally, we elaborate in Section 2.4 on the functional relationships used in the model, where we attempt to state the most general forms of parameters for which the analysis performed in subsequent chapters is valid.

2.1 Chuang's Model

Here we briefly describe the 1D model of Chuang et al. [12], who assumed that sap flow inside the stem from roots to leaves follows an unsaturated porous medium model, with three phases: solid (the stem structures), liquid (sap) and gaseous (air). The essential variable under consideration is the saturation $s(z,t)$ which is the local volume fraction of the sap, where z [m] is the height and t [s] is the time. In this model, the stem wood is assumed to have spatially homogeneous physical properties. Furthermore, owing to the 1D geometry, the radial and angular variations of saturation are neglected and only a vertical dependence is assumed. The flow inside the stem is assumed to be driven by two forces: one is the gravitational force acting downwards, and the other is a saturation dependent pressure force $\psi(s)$ [m] that pulls sap upwards towards the leaves. Thus the flow velocity has only a vertical component $v_z(z,t)$ [m/s] that has only a vertical spatial dependence and is given by Darcy's law

$$v_z = -K(s)\frac{\partial}{\partial z}\left(\psi(s) + z\right), \tag{2.1}$$

Table 2.1: Variables and parameters used in the governing equations. Values are for the "base case" used in the asymptotic analysis, while certain parameters from additional simulations are given in square brackets.

Symbol	Description	Units	Value or Formula
Independent and dependent variables:			
r	radial distance	m	
z	vertical distance	m	
t	time	s	
$s(r,z,t)$	sap volume fraction or saturation	–	
$S(r,z,t)$	dimensionless saturation deficit function	–	
$v_r(r,z,t)$	radial sap velocity	m/s	
$v_z(r,z,t)$	vertical sap velocity	m/s	
Solution-dependent and solution-independent functions:			
$E(t)$	transpiration rate per unit leaf area	$\mathrm{m}^3/\mathrm{m}^2\mathrm{s}$	(2.15)
$f(z)$	leaf area per unit trunk area (shading effect)	$\mathrm{m}^2/\mathrm{m}^2$	(2.17)
$\mathbb{K}$	hydraulic conductivity tensor	m/s	(2.4)
$K_{r,z}$	hydraulic conductivity components	m/s	(2.19)
$\ell(z)$	leaf area per unit height	m^2/m	(2.13)
$R(z)$	tree radius (in case of a varying radius)	m	(2.20)
$\lambda(z)$	sunlight shading effect	–	(2.14)
$\psi(s)$	pressure head	m	(2.18)
Dimensional parameters:			
E_0	$E(t)$ daily average	$\mathrm{m}^3/\mathrm{m}^2\mathrm{s}$	1×10^{-9} $\left[3.94\times10^{-8}\right]$
g	gravitational acceleration	$\mathrm{m/s}^2$	9.8
K_0	maximum vertical hydraulic conductivity	m/s	5.36×10^{-7}
ℓ_0	leaf specific area	m	15.3
p_0	fitting parameter for K	m	694
r_0	maximum tree radius (at base)	m	0.0645
z_0	tree height	m	6.7
τ	number of seconds per day	s	8.64×10^4
ρ	sap density	$\mathrm{kg/m}^3$	1000
ψ_0	parameter in $\psi(s)$	m	2.93×10^5
Dimensionless parameters:			
f_0	maximum of $f(z)$		2.6
n	fitting parameter for ψ		400
s_0	maximum sap volume fraction		0.574
α	exponential stem taper rate		0 or 1.42
β	fitting parameter for K		3.5
γ	ratio of inner to outer radius		0 $[0-0.75]$
δ	maximum relative saturation variation		$O(10^{-1})$ $\left[O(10^{-2})\right]$
ζ	stem aspect ratio $=\frac{r_0}{z_0}$		0.0096
η	temporal change parameter$=\left(\frac{2\pi z_0^2 s_0 n}{\tau K_0 \psi_0}\right)$		4.77
κ	max. radial to vertical hydraulic conductivities		$10^{-4}, 10^{-2}, 10^{0}$
μ	gravity parameter $=\frac{z_0 n}{\psi_0}$		0.0091
ϕ	transpiration parameter $=\frac{2f_0E_0}{K_0}\frac{\mu}{\zeta}$		0.0092 [0.363]

where $K(s)$ [m/s] is the saturation-dependent hydraulic conductivity. Notice that both pressure head $\psi(s)$ and hydraulic conductivity $K(s)$ have no explicit spatial dependence owing to the assumption of spatial homogeneity of the wood physical properties. In order to close the model equations, Chuang et al. [12] relied on the continuity equation

$$\frac{\partial s}{\partial t} = \frac{1}{A}\left(A v_z\right) - Q_{1D},$$

where $A(z)$ is the stem cross section area at height z, and Q_{1D} [1/s] is the transpiration rate from the leaves per unit stem volume (see Section 2.4 for details).

To complete the problem specification, suitable boundary and initial conditions are required. At the base of the tree ($z = 0$) we assume that there is a reservoir of root water available for uptake from the soil, which we impose via a Dirichlet condition

$$s|_{z=0} = s_0. \tag{2.2}$$

At the top of the stem ($z = z_0$) the vertical sap flux v_z must be zero, which can be expressed using a Neumann condition

$$1 + \psi' \left.\frac{\partial s}{\partial z}\right|_{z=z_0} = 0. \tag{2.3}$$

In the absence of any detailed measurements of water distribution within a tree stem, we take the initial saturation to be some constant value between 0 and s_0; however, this assumption is inconsequential for our analysis since we assume time periodic boundary conditions and neglect transient behavior.

2.2 Measurement Units

There are many variations in the literature of the meaning of the physical quantities we use, which warrants a brief discussion. Darcy's law in its most simple form (in the absence of gravity) states that

$$V_Q = -\frac{K_D \Delta P}{\rho \nu L}$$

where V_Q [m/s] is Darcy's velocity, K_D [m^2] is the specific hydraulic conductivity, ΔP [Pa] is the pressure difference, ν [m^2/s] is the kinematic viscosity, L [m] is the length, and ρ [kg/m^3] is the density. The units of K_D change if a mass flow rate is used instead. Lumping K_D and ν gives the hydraulic conductivity $K_C = K_D/\nu$ [s], then using $K = gK_C$ [m/s] and the pressure head difference $\Delta\psi = P/\rho g)$ [m], where g [m^2/s] is gravitational acceleration,

we get

$$V_Q = -\frac{K\Delta P}{L}$$

where the differential form in the presence of gravitational force is given in (2.1). Finally, water content is either given as a volumetric content [m^3/m^3] or as a mass content [kg/m^3]; it also also given as a percentage of the maximum empty space in a porous medium (or relative water content).

2.3 Axisymmetric Model for Sap Flow in a Tapered Cylinder

In this section, we extend the 1D model from the previous section to the case of an axisymmetric porous medium with angular symmetry, as depicted in Figure 2.1. This means that

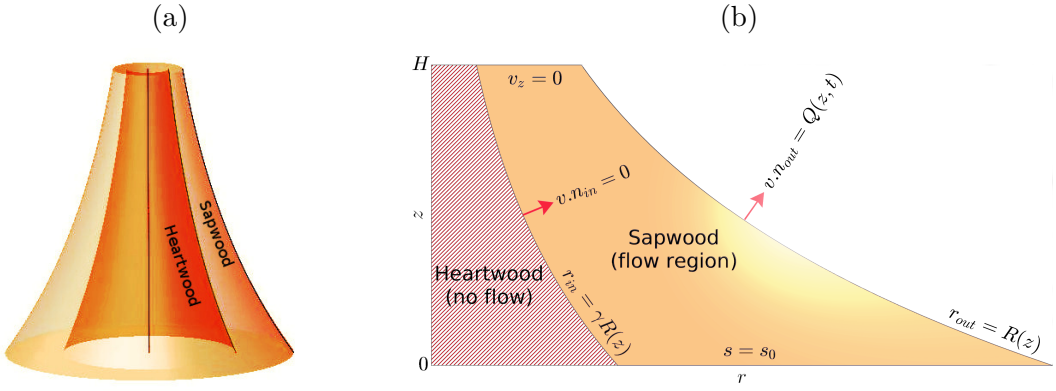

Figure 2.1: The left figure shows the tree trunk and its sapwood as a tapered annular cylinder (exponentially decaying radius case). The right figure shows a vertical cross section with the boundary conditions for the sap flow model.

the saturation $s(r, z, t)$ now has both vertical z [m] and radial r [m] dependencies. It also means that the flow velocity has both a radial $v_r(r, z, t)$ [m/s] and a vertical $v_z(r, z, t)$ [m/s] component, where both components have radial and vertical spatial dependencies. The flow is similarly driven by pressure gradients and the gravity so the flow velocity v is

$$v = -K(r, z)\nabla(\psi(s) + z),$$

where $\mathbb{K}$ is the hydraulic conductivity tensor

$$\mathbb{K}(r, z) = \begin{bmatrix} K_r(r, z) & 0 \\ 0 & K_z(r, z) \end{bmatrix}, \tag{2.4}$$

which is symmetric and positive definite, and ψ is the pressure head. Here we assume that K_r is nonzero and that $\mathbb{K}$ has an explicit spatial dependence and no saturation dependence

(contrast with the model in Section 2.1). The reason for adopting this point of view is explained further in Section 2.4. The velocity components in cylindrical coordinates are

$$v_r = -\left(K_r \frac{\partial \psi}{\partial r}\right), \qquad v_z = -\left(K_z \frac{\partial \psi}{\partial z} + K_z\right). \tag{2.5}$$

Now the continuity equation is

$$\frac{\partial s}{\partial t} = -\nabla \cdot v, \tag{2.6}$$

which in cylindrical coordinates becomes

$$\frac{\partial s}{\partial t} = \frac{1}{r}\frac{\partial}{\partial r}\left(rK_r \frac{\partial \psi}{\partial r}\right) + \frac{\partial}{\partial z}\left(K_z \frac{\partial \psi}{\partial z}\right) + \frac{\partial K_z}{\partial z}. \tag{2.7}$$

A tree can have a complicated geometry, with the trunk splitting into several major branches and with these branches dividing into smaller branches. Some trees like conifers have a main trunk with no major branches, and with small branches carrying the leaves emanating from the trunk surface. We will focus on the latter case, taking the domain as the tree trunk and relegating the effect of branches to a pre-assigned flux from the trunk surface that has spatial and temporal t variations but does not depend on saturation. Nonetheless, this case could be generalized to by considering the branches as "mini-trunks" and attaching these mini-trunks to the main trunk (this approach is not touched upon here since it requires a full 3D model including angular variation).

Note that many trees experience a reduction in sap conductivity in the innermost portions of the tree trunk as they grow, due to embolism formation and other factors. For this inner heartwood portion, the boundary is assumed to follow the same functional relation as the lateral trunk surface, so that the domain has the annular cylindrical form

$$\gamma R(z) \leqslant r \leqslant R(z) \qquad \text{for} \qquad 0 \leqslant z \leqslant z_0, \tag{2.8}$$

where z_0 [m] is the tree height, $R(z)$ [m] is the tree radius at height z and $0 \leq \gamma < 1$ is the heartwood portion of the tree radius that is nonconductive.

Now turning to the boundary conditions, the lateral surface of the trunk at $r = R(z)$ is assigned a time-periodic and height-dependent transpiration flux, taking into account the effect of sun exposure on transpiration through leaf density and shading $f(z)$, and diurnal variation $E(t)$ [m/s], to get

$$v \cdot \hat{n}|_{r=R(z)} = Q_{3D}, \tag{2.9}$$

where $\hat{n}$ is the unit outward pointing surface normal and

$$Q_{3D} = f(z)E(t)$$

(see Section 2.4 for the actual specification of the functions f and E). This is in contrast to the source transpiration term Q_{1D} in Chuang's model in Section 2.1.

The inner tree boundary at $r = \gamma R(z)$ is assigned zero flux because fluid cannot penetrate the heartwood:

$$v \cdot \hat{n}|_{r=\gamma R(z)} = 0, \tag{2.10}$$

and the upper boundary is also assigned zero flux

$$v_z|_{z=z_0} = 0. \tag{2.11}$$

We assume that the soil has an adequate supply of water so that the bottom of the trunk at $z = 0$ is fully saturated

$$s|_{z=0} = s_0, \tag{2.12}$$

where s_0 is the porosity of the medium, or the maximum allowed saturation level. This can be relaxed to any fixed saturation level s_0 without much change in the analysis, provided that the saturation level is not too low to the degree of forming embolisms (theoretically, since we are assuming embolized tracheids never recover, and since the lumen radius of tracheids is of the order of tens of micrometers, the saturation should be slightly lower than full saturation to allow the pressure to be a few kilopascals lower than atmospheric pressure and to counter act the surface tension forces inside the lumen that act to collapse the air bubble). A graphical summary of the boundary conditions is provided in Figure 2.1.

To summarize, the reasons for extending Chuang's model into a 3D axisymmetric model are:

- Our extension to 3D permits flow in the radial direction and also accounts for potentially large differences in the radial and axial conductivities.
- We include radial variations in certain physical parameters, in particular in the conductivities which typically decrease with sapwood depth and increase with stem height.
- We incorporate a non-conducting heartwood zone that corresponds to a more realistic annular geometry.
- Transpiration flux is incorporated as a radially-directed outflow through the tree surface, rather than simply a volume-averaged quantity as in the 1D model.
- This model is a natural first step towards developing a fully 3D model that incorporates radially-dependent features such as directional solar heating, non-uniform stem shape and actual branching geometries.

2.4 Coefficient Functions from Chuang et al.

Here we provide details about parameter estimates and functional relationships used in our model that are specific to the Norway spruce data considered in [12]. All symbols are listed in Table 2.1 along with their units and values, which are chosen to match the data as much as possible. Notice that a couple of parameters have two values listed: the transpiration average $E_0 = 3.94 \times 10^{-8}$ [m/s] is used in all the simulations and figures, and approximates the data measured in [12] on the particular days they took the measurements, whereas $E_0 = 1 \times 10^{-9}$ [m/s] is used in our asymptotic analysis, which represents the transpiration on cloudy humid day (i.e. under conditions not favorable for transpiration). The corresponding values for ϕ are 0.363 and 0.0092. The values used in the asymptotic analysis correspond to the case $\mu = \phi$, which says that both transpiration and gravity are significant, while the values in [12] correspond to the case $\mu \ll \phi$ so that transpiration is much more significant. One more parameter that has multiple values is γ, with [12] using $\gamma = 0$ in their model, which is the value we use in our asymptotic analysis and most of the figures except where we otherwise specify.

The relationship between our model transpirational flux and Chuang's model transpiration rate can be derived by considering a thin horizontal cylindrical slice of the tree of height dr

$$2\pi r Q_{3D} = \pi r^2 Q_{1D} dr,$$

which simplifies to

$$Q_{3D} = \frac{R(z)}{2} Q_{1D}.$$

The paper uses experimental data for the Norway spruce tree (Picea abies) to derive functional forms for R, ψ, f and E. These particular functional forms are not critical for most of our analysis although we use them for our simulations to verify the analysis and extract the essential properties of these functions that we rely on in our analysis.

For the effect of sun exposure on transpiration, the authors of [12, Fig. 4] propose the following formula for the leaf area density [m^2/m]

$$\ell(z) = \ell_0 \operatorname{sech}^2\left(6\frac{z}{z_0} - 2.4\right) \tag{2.13}$$

The effect of shading $\lambda(z)$ is derived from a rough fit to data in [12, Fig. 5]

$$\lambda(z) = \frac{1}{\pi} \arctan\left(63\left(\frac{z}{z_0}\right) - 50\right) + 0.53, \tag{2.14}$$

Similarly, the diurnal variation $E(t)$, which is the leaf transpiration flux in the absence of shading, is assumed to consist of the first three terms of a Fourier series

$$E(t) = E_o \Re\left[1 + d_1 e^{\frac{2\pi i t}{\tau}} + d_2 e^{\frac{4\pi i t}{\tau}}\right], \tag{2.15}$$

where time t is measured starting at midnight on the first day, $\tau = 86,400$ [s] is the diurnal period, and $E_o = 3.94 \times 10^{-8}$ [m/s] is the amplitude of the transpiration flux. The complex fitting parameters $d_1 = -0.9118 - 0.0494\text{i}$ and $d_2 = -0.0446 + 0.1861\text{i}$ are obtained by taking the discrete Fourier transform of the data obtained from digitizing [12, Fig. 7]. The right plot of Figure 2.2 shows the resulting $E(t)$. In our asymptotic analysis, we will assume that $E(t)$ has a general Fourier expansion

$$E(t) = E_0 \Re \left[\sum_{m=0}^{\infty} d_m e^{\frac{2\pi m i t}{\tau}} \right], \tag{2.16}$$

where E_0 is the average leaf transpiration flux (without shading effects) and $d_0 = 1$. Transferring the effect of transpiration flux from a source in the continuity equation (as in [12]) to a boundary condition at $r = R(z)$, we get the spatial component of the transpiration

$$f(z) = \frac{\ell(z)\lambda(z)}{2\pi \bar{R}(z)}, \tag{2.17}$$

where

$$\bar{R}(z) = \left(\frac{0.0645}{r_0} \right) R(z).$$

The left plot of Figure 2.2 shows the resulting $f(z)$, which we use in the simulations for illustration purposes except where we specify explicitly a different form; otherwise for the purpose of our asymptotic analysis, we assume a general positive and smooth function $f(z)$.

According to Chuang et al. [12], the pressure head has the form

$$\psi(s) = \psi_0 \left[1 - \left(\frac{s_0}{s} \right)^{\frac{1}{n}} \right], \tag{2.18}$$

where $\psi_0 = 2.93 \times 10^5$ [m] is a scaling parameter, and $n = 400$ is a fitting parameter. This is similar to the van Genuchten model commonly used to describe capillary pressure in soil and rock [62] and has also been applied to drying of lumber [32]. Note that pressure head is a negative quantity because $s < s_0$, reflecting the understanding in the sap hydraulics literature that sap within a tree stem is under tension. The most important characteristics of this curve, some of which we use in our analysis, and especially near full saturation, are:

- ψ is an increasing function of s otherwise we get a negative diffusion coefficient in (2.7).
- ψ is concave downwards, because it becomes ever harder to extract moisture from the tissue surrounding the xylem, as water recedes into the interstices of cell walls, and the cell plasma becomes more concentrated (osmotic pressure).

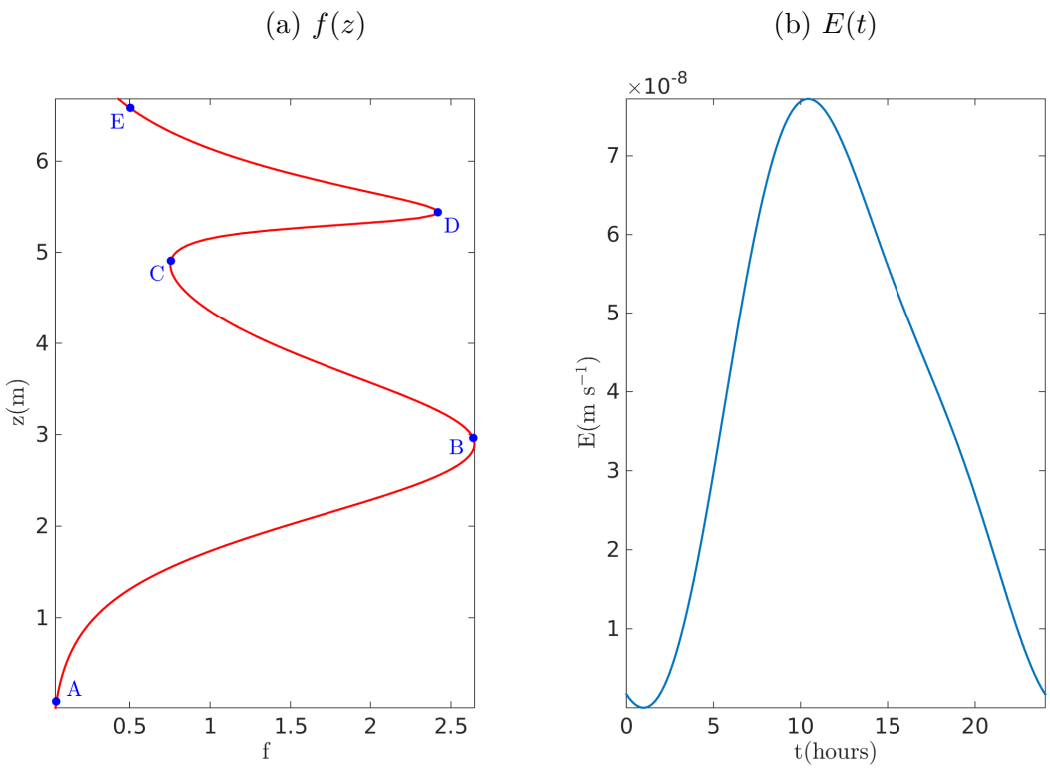

Figure 2.2: (a) Transpiration vertical profile function $f(z)$ specified in (2.17) (b) leaf transpiration flux function $E(t)$ specified in (2.15). Both functions are used in most of the simulations for the sap flow (unless otherwise indicated), with $E_0 = 3.94 \times 10^{-8}$, $\alpha = 1.42$ and $\gamma = 0$, and the rest of the parameters as shown in Table 2.1.

- ψ varies smoothly and does not have sudden abrupt changes in its gradient. Abrupt jumps and hysteresis may occur only due to embolism, which we assume does not happen due to the small saturation variations.

For our analysis, we assume a general $\psi(s)$ in the form of a Taylor expansion that captures these properties as in (4.2).

Now, for the conductivity, the vulnerability curve Chuang et al. use is

$$K(s) = K_0 e^{-\left(-\frac{\psi(s)}{p_0}\right)^{\beta}}, \tag{2.19}$$

where $K_0 = 5.36 \times 10^{-5}$ [m/s] is the hydraulic conductivity at maximum saturation, and $p_0 = 694$ [m] and $\beta = 3.5$ are fitting parameters. It is worth noting that this sigmoidal curve is nearly flat close to full saturations because the main cause of loss of hydraulic conductivity is embolism formation, and this does not occur unless the saturation drops well below the full saturation level s_0. If we assume that tree has been exposed to embolism in the past, due for example to drought, but is not currently experiencing these harsh conditions that cause embolism formation, then we can assume that the hydraulic conductivity has an explicit spatial dependence and no saturation dependence. Furthermore, since the radial flow goes through tiny pits connecting xylem elements, and through few radial parenchyma cells, while the vertical flow goes through the xylem lumen for the most part, the hydraulic conductivity in the vertical direction K_z is larger than the hydraulic conductivity in the radial direction K_r. Thus for our model, we assume a general tensorial hydraulic conductivity, with explicit spatial dependence and no saturation dependence, as given in (2.4); however, to get an explicit solution for saturation in the time varying case (see Section 4.4), we assume that K is a constant near full saturation.

Finally, in Chuang et al. [12], and for the purpose of simplifying the analysis, the tree radius variation with height is chosen to be

$$R(z) = r_0 e^{-\alpha\left(\frac{z}{z_0}\right)}, \tag{2.20}$$

where the tapering parameter $\alpha = 1.42$ controls the radius decay rate, and $r_0 = 0.0645$ [m] is the tree radius at $z = 0$ [m]. This can be written as

$$R(z) = r_0 R^*\left(\frac{z}{z_0}\right), \tag{2.21}$$

where R^* is a function of order $O(1)$. This later form is sufficient to proceed with the asymptotic analysis, but to get a closed form solution for the time varying case, we eventually use (2.20), which is the only function with the simplifying property that R'/R is constant, which we use to simplify the analytic solution equations; the exponential form is also used to illustrate our numerical results. It is worth mentioning here that there is an

extensive literature on more complicated functional fits to the diameter-versus-height relationship [35, 46, 48], from which we conclude that a wide range of coniferous and deciduous tree species have a small enough taper rate that such an exponential function provides a reasonable approximation to stem shape.

Chapter 3

Numerical Method

In this chapter we develop a numerical scheme for solving the equations in the previous chapter based on a cell-centered finite volume approximation. We perform a convergence study to validate the scheme and run simulations to illustrate the effects of varying the heartwood fraction γ on radial velocity. This numerical scheme will be used to validate our asymptotic results and to investigate cases not covered by the asymptotics.

3.1 Coordinate Transformation

To simplify the discrete equations, it is helpful to first transform the radial coordinate for the tapered annular cylindrical domain. We therefore transform the annular sapwood domain in which flow occurs

$$\gamma R(z) \leqslant r \leqslant R(z) \qquad \text{for} \qquad 0 \leqslant z \leqslant z_0,$$

using the transformation

$$\tilde{r} = \frac{r}{R(z)},$$

while keeping the vertical coordinate z untouched. The resulting transformed coordinates $\tilde{r}$, z describe a right circular region

$$\gamma \leqslant \tilde{r} \leqslant 1 \qquad \text{and} \qquad 0 \leqslant z \leqslant z_0,$$

which can be conveniently discretized on a fixed rectangular grid in $\tilde{r}, z$. Spatial derivatives are transformed according to the rules

$$\frac{\partial}{\partial r} = \frac{1}{R(z)}\frac{\partial}{\partial \tilde{r}} \qquad \text{and} \qquad \frac{\partial}{\partial z} = -C\tilde{r}\frac{\partial}{\partial \tilde{r}} + \frac{\partial}{\partial z},$$

where

$$C = \frac{R'}{R} = -\frac{a}{z_0},$$

is a constant owing to the special exponential form assumed for $R(z)$ in (2.20).

Next, applying the coordinate transformation to the velocity expression components yields turn into

$$v_r = -\frac{D_r}{R(z)}\frac{\partial s}{\partial \tilde{r}} \qquad \text{and} \qquad v_z = -K_z + C\tilde{r}D_z\frac{\partial s}{\partial \tilde{r}} - D_z\frac{\partial s}{\partial z},$$

where

$$D_r = K_r\psi'(s) \qquad \text{and} \qquad D_z = K_z\psi'(s).$$

Here, K_r and K_z can be either equal and saturation dependent as in [12] or else they can be spatially dependent as in our model. We use a general saturation dependent hydraulic conductivity $K(s)$ in order to compare to the experimental data in [12] (see Section 6.1).

The final continuity equation becomes

$$\frac{\partial s}{\partial t} = -\nabla \cdot v = -\frac{1}{R(z)\tilde{r}}\frac{\partial\left(\tilde{r}v_r\right)}{\partial \tilde{r}} + C\tilde{r}\frac{\partial v_z}{\partial \tilde{r}} - \frac{\partial v_z}{\partial z},$$

which we emphasize is now posed on a rectangular domain for which standard finite difference schemes can be easily applied.

3.2 Finite Difference Discretization

Next we discretize the velocity and continuity equations using a cell centered finite difference scheme. The domain is divided into a regular grid with $\Delta\tilde{r}$ as the radial step size, and Δz as the vertical step size. The saturation values are calculated at the cell centers, and the velocities are calculated at the cell edge centers. The derivatives are approximated using centered differences and fractional indices indicate edge centers (one half index) or cell corners (both indices are shifted by half). The saturations at edge centers and cell corners are approximated using the arithmetic mean of the two cells sharing the edge or the four cells sharing the corner. The discretization stencil with nodes labelled by corresponding indices is shown in Figure 3.1.

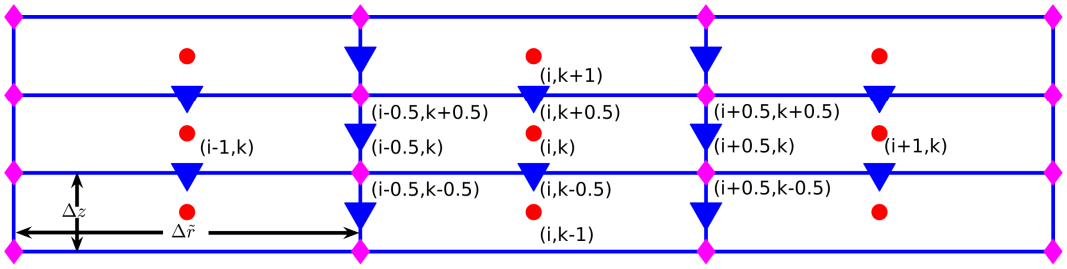

Figure 3.1: Discrete grid point locations in transformed coordinates, with points indexed as (r_i, z_k). Saturation is approximated at cell centers (red circles) and velocity components on cell edges (blue triangles). The discrete equations involve saturations at cell corners (magenta diamonds, approximated using an average of cell-centered values) so that the difference equations for $ds_{i,k}/dt$ correspond to a full nine-point stencil involving the neighbouring saturation points denoted in red.

The outcome of the discretization is

$$
\begin{aligned}
(v_r)_{i+\frac{1}{2},k} &= -\left(\frac{(D_r)_{i+\frac{1}{2},k}}{R_k\Delta\tilde{r}}\right)(s_{i+1,k}-s_{ik})\,,\\
(v_z)_{i+\frac{1}{2},k} &= -\left[(K_z)_{i+\frac{1}{2},k}-\left(\frac{C\tilde{r}_{i+\frac{1}{2}}(D_z)_{i+\frac{1}{2},k}}{\Delta\tilde{r}}\right)(s_{i+1,k}-s_{ik})\right.\\
&\qquad\left.+\left(\frac{(D_z)_{i+\frac{1}{2},k}}{\Delta z}\right)\left(s_{i+\frac{1}{2},k+\frac{1}{2}}-s_{i+\frac{1}{2},k-\frac{1}{2}}\right)\right],\\
(v_z)_{i,k+\frac{1}{2}} &= -\left[K_{i,k+\frac{1}{2}}-\left(\frac{C\tilde{r}_i(D_z)_{i,k+\frac{1}{2}}}{\Delta\tilde{r}}\right)\left(s_{i+\frac{1}{2},k+\frac{1}{2}}-s_{i-\frac{1}{2},k+\frac{1}{2}}\right)\right.\\
&\qquad\left.+\left(\frac{(D_z)_{i,k+\frac{1}{2}}}{\Delta z}\right)(s_{i,k+1}-s_{ik})\right].
\end{aligned}
$$

As for the continuity equation, the discretization is

$$
\begin{aligned}
\frac{\partial s_{ik}}{\partial t} = &-\frac{1}{\tilde{r}_i R_k\Delta\tilde{r}}\left(\tilde{r}_{i+\frac{1}{2}}(v_r)_{i+\frac{1}{2},k}-\tilde{r}_{i-\frac{1}{2}}(v_r)_{i-\frac{1}{2},k}\right)+\frac{C\tilde{r}_i}{\Delta\tilde{r}}\left((v_z)_{i+\frac{1}{2},k}-(v_z)_{i-\frac{1}{2},k}\right)\\
&-\frac{1}{\Delta z}\left((v_z)_{i,k+\frac{1}{2}}-(v_z)_{i,k-\frac{1}{2}}\right)
\end{aligned}
$$

Now in order to treat the boundaries, the continuity equation is integrated over the boundary cell, and the divergence theorem is used to get

$$
\frac{\partial s}{\partial t} = -\frac{1}{|\Omega|}\oint_{\partial\Omega} v\cdot\hat{n}\;dA,
$$

where s here is the average of saturation over the cell volume Ω, and dA is the area element over the cell boundary surface $\partial\Omega$. This integral can be approximated by considering the average of the velocity on each edge of the cell and approximating the curved portions of

the boundaries as straight lines (surfaces in 3D). This results in

$$\frac{\partial s}{\partial t} \approx -\frac{1}{|\Omega|} \sum_{j^{th}side} (\vec{v}_j \cdot \hat{n}_j)\, A_j.$$

Now the (r, z) coordinates of the corners of the cell (i, j) are calculated as follows: first the z coordinates of the bottom (B) and top (T) corners are given by

$$(z_B)_{ik} = z_k - \frac{\Delta z}{2} \qquad \text{and} \qquad (z_T)_{ik} = z_k + \frac{\Delta z}{2},$$

then the r coordinates of the corners of the cell are calculated using

$$\begin{aligned} (r_{BR})_{ik} &= \left(\tilde{r}_i + \frac{\Delta \tilde{r}}{2}\right) R((z_B)_{ik}), & (r_{TR})_{ik} &= \left(\tilde{r}_i + \frac{\Delta \tilde{r}}{2}\right) R((z_T)_{ik}), \\ (r_{BL})_{ik} &= \left(\tilde{r}_i - \frac{\Delta \tilde{r}}{2}\right) R((z_B)_{ik}), & (r_{TL})_{ik} &= \left(\tilde{r}_i - \frac{\Delta \tilde{r}}{2}\right) R((z_T)_{ik}), \end{aligned}$$

where r_{BR}, r_{TR}, r_{BL} and r_{TL} are the bottom right, top right, bottom left and top left radii of the cell corners. The areas of the top (A_T), the bottom (A_B), the left (A_L) and the right (A_R) surfaces are given by the following formula

$$\begin{aligned} A_B &= \pi(r_{BR}^2 - r_{BL}^2), & A_L &= \pi(r_{TL} + r_{BL})\sqrt{(r_{BL} - r_{TL})^2 + (\Delta z)^2}, \\ A_T &= \pi(r_{TR}^2 - r_{TL}^2), & A_R &= \pi(r_{TR} + r_{BR})\sqrt{(r_{BR} - r_{TR})^2 + (\Delta z)^2}, \end{aligned}$$

where r_{RT}, r_{RB}, r_{LT} and r_{LB} are the radii of the corners of the cross-section of the cell (or edges of bounding surfaces intersections in 3D). The volume of the cell is given by

$$|\Omega| = \frac{1}{3}\pi \Delta z \left[\left(r_{RT}^2 + r_{RB} r_{RT} + r_{RB}^2\right) - \left(r_{LT}^2 + r_{LB} r_{LT} + r_{LB}^2\right)\right].$$

To calculate the velocities at the lower boundary of the domain, fictitious cells are added to the lower boundary, and the saturations s_{i0} in the fictitious cells are calculated by linearly extrapolating using the Dirichlet BC at the boundary cell edge $s = s_0$ to get

$$s_{i0} = 2s_0 - s_{i1},$$

where s_{i1} are the saturations at the lower boundary. The velocity at the bottom surface of the lower boundary cell is calculated as for a typical interior cell.

For time stepping, the Matlab ODE solver ode15s is used. We provide the sparsity pattern of the Jacobian matrix and use tolerance values `ABSTOL` = `RELTOL` = 1×10^{-10}.

Table 3.1: Grid refinement study. The order of convergence is estimated as the base-2 logarithm of the ratio of successive grids errors. Errors are estimated based on the solution from a 500×500 grid.

No. of cells	ℓ_1-error	Order
31×31	2.2910×10^{-5}	–
63×63	4.0361×10^{-6}	2.5049
125×125	9.7881×10^{-7}	2.0439
250×250	2.4615×10^{-7}	1.9915

3.3 Validation of Numerical Scheme

The numerical scheme exhibits a numerical convergence rate of order 1.99 which is consistent with the expected order 2. The order of convergence is computed by taking successively finer grids, and comparing to the finest grid while computing to steady state. Errors are estimated using the L1 norm difference between the solution on the current grid and the solution on the finest grid as a surrogate for the exact solution. This was done for the case of $\alpha = 1.42$. The results are shown in Table 3.1.

Chapter 4

Asymptotic Series Solution

In this chapter, we apply methods from asymptotic analysis to develop approximate solutions for the $3D$ model from Section 2.3 under various conditions. We first nondimensionalize the governing equations in Section 4.1 to obtain four dimensionless parameters that capture certain aspects of the model behaviour. Next we perform a regular asymptotic expansion of the saturation in terms of the small dimensionless parameter ζ (stem aspect ratio) to derive simpler linear differential equations for the saturation in Section 4.2. This yields a general solution for the constant transpiration steady state case in Section 4.3 as well as a solution for the time-varying constant hydraulic conductivity case in Section 4.4 (where we expand the time component of the transpiration $E(t)$ in terms of Fourier modes). The ratio of radial to vertical velocities is discussed in Section 4.5. The physical meaning of the model parameters and direct measurements are discussed in Section 4.8. Anisotropic hydraulic conductivity effects are discussed in Section 4.9.1, where steady state leading order solutions are derived. We also discuss the situation where the branches are concentrated within a crown region (more consistent with deciduous tree species) and for which interpretations are easier to reach in Section 4.9.3.

It is worth mentioning here that the following analysis, at least for the steady state, bears some resemblance to the work of Kevorkian for the problem of heat conduction in a long rod of circular cross section [33, Chapter 4]. Our analysis has been performed for a general radius variation with height and a general hydraulic conductivity although for the time varying solution the specific exponential form (2.20) and a constant scalar K are assumed at the last step in order to solve the resulting ODE and for a general leaf distribution $f(z)$ and transpiration $E(t)$ functions. Both the steady state and the time periodic solutions have been obtained using two terms in the asymptotic expansion.

4.1 Nondimensionalization

As a preparatory step, we begin by writing the governing equations and boundary conditions in dimensionless form, which allows comparison of the order of magnitude of terms in the equations through the resulting dimensionless parameters. First, a brief clarification on notation: when we state $A \sim B$, we mean that two quantities are of the same order of magnitude, while $A = O(B)$ means that A is of the same order as B but is also allowed to be lower. In the following, we make the fundamental assumption the the expansion parameter ζ from (4.4) is fixed and $\zeta \ll 1$. We also assume that the conductivities K_r and K_z are the same order of magnitude and are never equal to zero. The vertical variations of saturation and vertical velocity in this case are also relevant to the more physical case when $K_r \ll K_z$, which is discussed in Section 4.9.1. In addition, we set $\gamma = 0$ in (2.8) so that sap flows throughout the entire tree trunk (see Section 6.1 for a discussion of $\gamma > 0$). We further assume the order of magnitude estimate for $\eta \sim 1$ form (4.13) which is motivated by experimental data fits in Chuang et al. [12], although we consider other cases in Section 4.9.2.

We proceed by nondimensionalizing the main equation (2.7), and the boundary conditions (2.9), (2.10), (2.11) and (2.12). We use the following nondimensionalizations of the variables

$$\begin{aligned} &r = r_0 r^*, && z = z_0 z^*, && f = f_0 f^*, && s = s_0\,(1 - \delta S)\,, \\ &E = E_0 E^*, && t = \frac{\tau}{2\pi} t^*, && R = r_0 R^*, && K_r = \kappa K_0 K_r^*, \\ &K_z = K_0 K_z^*, \end{aligned} \tag{4.1}$$

where r_0 is the maximum stem radius at the base, z_0 is the stem height, f_0 is the maximum of f, s_0 is the maximum saturation, E_0 is the average value of E, $\tau = 86400$ [s] is the number of seconds in a day (unless we are considering longer time intervals), K_0 is the maximum vertical conductivity, and κ is the ratio of the maximum of K_r to the maximum of K_z. We assume that saturation inside the stem near full saturation, thus we incorporate a small parameter δ into the definition for saturation deficit S, emphasizing that δ will eventually cancel out in the final dimensional solutions.

Expanding pressure head ψ in a Taylor series in δ yields

$$\psi(S) = -\delta \bar{\psi}_0 S \left[1 + \frac{1}{2}\psi_1 \delta S + \frac{1}{6}\psi_2 \delta^2 S^2 + \cdots\right], \tag{4.2}$$

where

$$\bar{\psi}_0 = \frac{\psi_0}{n}, \qquad \psi_1 = \frac{n+1}{n} = 1 + \frac{1}{n} \sim 1, \qquad \psi_2 = \left(\frac{n+1}{n}\right)\left(\frac{2n+1}{n}\right) = 2 + O\left(\frac{1}{n}\right) \sim 1,$$

Taking the derivative with respect to s and noting that $\frac{d}{ds} = -\frac{1}{\delta s_0}\frac{d}{dS}$

$$\frac{d}{ds}\left(\psi(S)\right) = \frac{\bar{\psi}_0}{s_0}\left[1 + \psi_1\delta S + \frac{1}{2}\psi_2\delta^2 S^2 + \cdots\right].$$

Note that we only need the first two terms in the Taylor expansion of the derivative of ψ, so we will discard any indication of the remaining terms to reduce clutter.
Substituting (4.2) into the main equation (2.7) and nondimensionalizing using (4.1) we get

$$\eta\zeta^2\frac{\partial S}{\partial t} = \kappa\frac{1}{r}\frac{\partial}{\partial r}\left(rK_r\left(1+\psi_1\delta S\right)\frac{\partial S}{\partial r}\right) + \zeta^2\frac{\partial}{\partial z}\left(K_z\left(1+\psi_1\delta S\right)\frac{\partial S}{\partial z}\right) - \left(\frac{\mu\zeta^2}{\delta}\right)\frac{\partial K_z}{\partial z}, \quad (4.3)$$

where the superscript $*$ is dropped from all dimensionless variables from now on, and we will clearly mention when we return to dimensional variables. The three dimensionless parameters that appear in equation (4.3) are

$$\zeta = \frac{r_0}{z_0}, \qquad \mu = \frac{nz_0}{\psi_0}, \qquad \eta = \frac{2\pi n s_0 z_0^2}{\tau K_0 \psi_0}, \quad (4.4)$$

which will appear frequently in the analysis below. Notice that the most striking and obvious feature of our problem is the small aspect ratio of the domain

$$\zeta \ll 1,$$

which we adopt as the key parameter for our asymptotic expansions.

The top (2.11) and bottom (2.12) boundary conditions yield after nondimensionalizing and series expansion

$$S(r,0,t) = 0, \quad (4.5)$$

$$\left(1+\psi_1\delta S\right)\frac{\partial S}{\partial z} = \frac{\mu}{\delta}. \quad (4.6)$$

If we assume that the derivatives are of $O(1)$ then

$$\frac{\mu}{\delta} = \frac{\text{gravity force}}{\text{saturation dependent force}} = O(1). \quad (4.7)$$

We will assume that

$$\mu \sim \delta \quad (4.8)$$

so that the gravity contribution is important in (4.6), noting that the gravity term would shift to lower order terms in the solution for the case of $\mu \ll \delta$. As for the boundary

condition (2.9) at $r = R(z)$,

$$\kappa n_r \left(K_r \frac{\partial S}{\partial r} \right) + n_z \left(\zeta K_z \frac{\partial S}{\partial z} - \frac{\mu\zeta}{\delta} K_z \left(1 - \psi_1 \delta S\right) \right) = \frac{\zeta^2 \phi}{2\delta} f(z) E(t) \left(1 - \psi_1 \delta S\right), \qquad (4.9)$$

where the normal vector components are

$$n_r = \frac{1}{\sqrt{1 + (R'(z))^2}} \qquad \text{and} \qquad n_z = \frac{-R'(z)}{\sqrt{1 + (R'(z))^2}}.$$

The dimensionless parameter ϕ appearing in equation (4.9) is defined by

$$\phi = \frac{2 f_0 E_0}{K_0} \frac{\mu}{\zeta} \qquad (4.10)$$

Note that the appearance of ζ in the denominator is not a problem since μ is of similar order, as is shown in Table 2.1, and as will see later on in the order of magnitude relationship (4.27).

Substituting $R(z) = r_0 R^* \left(\frac{z}{z_0}\right)$ where $R^* = O(1)$, we get $R'(z) = \zeta (R^*(z^*))'$, and then expanding in terms of ζ, the normal vector components become

$$\begin{aligned} n_r &= \frac{1}{\sqrt{1 + (R'(z))^2 \zeta^2}} = 1 - \frac{1}{2}(R'(z))^2 \zeta^2 + \cdots, \\ n_z &= \frac{-R'(z)\zeta}{\sqrt{1 + (R'(z))^2 \zeta^2}} = -R'(z)\zeta \left(1 - \frac{1}{2}(R'(z))^2 \zeta^2 + \cdots\right), \end{aligned}$$

where the * superscript is dropped as already mentioned. Employing the above approximations and nondimensionalizing using (4.1), the result is the dimensionless boundary equation

$$\begin{aligned} \kappa \left(1 - \frac{1}{2}(R'(z))^2 \zeta^2\right) \left(K_r \frac{\partial S}{\partial r}\right) & \\ - \zeta R'(z) \left(1 - \frac{1}{2}(R'(z))^2 \zeta^2\right) \left(\zeta K_z \frac{\partial S}{\partial z} - \frac{\mu\zeta}{\delta} K_z \left(1 - \psi_1 \delta S\right)\right) & \\ = \frac{\zeta^2 \phi}{2\delta} f(z) E(t) \left(1 - \psi_1 \delta S\right), & \qquad (4.11) \end{aligned}$$

where ϕ is given in equation (4.10) and where we have also expanded $\frac{1}{\psi(s)}$ as a series in δS as we did for ψ.

See Section 4.8.2 for a detailed interpretation of the physical meaning of the dimensionless parameters in (4.4) and (4.10).

4.2 Asymptotic Expansion for the General Case

Here we will proceed with our asymptotic analysis for the dimensionless equations obtained in the previous section, assuming a general spatial dependence in hydraulic conductivity and a general tree radius function $R(z)$. The outcome of our analysis will be a set of one-dimensional differential equations. Following that in sections (4.3), (4.4) and (4.5), we will consider special cases for which we can obtain closed form solutions for these differential equations.

We start by assuming a regular expansion of S in terms of ζ

$$S = S_0 + S_1\zeta + S_2\zeta^2 + S_3\zeta^3 + \cdots \tag{4.12}$$

We will employ the order of magnitude assumption

$$\eta \sim 1, \tag{4.13}$$

and other cases will be considered later in section 4.9.2. Note that we will need to consider the expansion up to order ζ^3, because in order to obtain a reasonably accurate solution, we need to determine S_0 and S_1, which cannot be determined without the next two terms S_2 and S_3. In addition, having S_1 will allow us to calculate the radial component of sap velocity.

Substituting (4.12) into (4.3) yields the leading order equation

$$\frac{1}{r}\frac{\partial}{\partial r}\left(rK_r\frac{\partial S_0}{\partial r}\right) = 0.$$

Assuming that K_r is never equal to zero, this equation implies that the leading order term S_0 is independent of the radial coordinate, or

$$S_0 = S_0(z,t).$$

The next order equation of order ζ yields the same result

$$\frac{1}{r}\frac{\partial}{\partial r}\left(rK_r\frac{\partial S_1}{\partial r}\right) = 0,$$

so that similarly

$$S_1 = S_1(z,t). \tag{4.14}$$

Note that due to the absence of radial dependence of S_0 and S_1, the boundary condition (4.11) at $r = R(z)$, and if we assume that derivatives are of $O(1)$, we have the following order of magnitude relationship:

$$\frac{\phi}{\delta} = O(1). \tag{4.15}$$

We will assume that

$$\phi \sim \delta \tag{4.16}$$

so that the effect of transpiration on the trunk saturation is observable, whereas the transpiration effect is shifted to lower order terms in the case of $\phi \ll \delta$. Note that assumption (4.16) together with the earlier assumption $\mu \sim \delta$ in (4.7) implies $\phi \sim \mu$. Now for the case of *Picea abies* parameter values in [12], and for the particular level of transpiration on the days the measurements were made, we actually have $\mu \ll \phi$; however, we know that transpiration varies according to the surrounding weather conditions, thus we shouldn't restrict ourselves to any particular order of magnitude for ϕ. In fact, our choice of $\mu \sim \phi$ to develop our asymptotics produces a solution that is a good approximation of the solution for the other case of $\mu \ll \phi$, as we will see later on in Section 4.6.

Moving on to higher order terms, for the order ζ^2 equation we have

$$\kappa \frac{1}{r}\frac{\partial}{\partial r}\left(rK_r\frac{\partial S_2}{\partial r}\right) = f_2(r,z,t), \tag{4.17}$$

where

$$f_2(r,z,t) = \eta\frac{\partial S_0}{\partial t} - \frac{\partial}{\partial z}\left(K_z\frac{\partial S_0}{\partial z}\right) + \frac{\mu}{\delta}\frac{\partial K_z}{\partial z},$$

so that after integrating once and substituting $r = R(z)$ we obtain

$$\kappa RK_r\frac{\partial S_2}{\partial r} = -\int_0^R r f_2(r,z)dr = \frac{\eta}{2}R^2\frac{\partial S_0}{\partial t} - \int_0^R r\frac{\partial}{\partial z}\left(K_z\frac{\partial S_0}{\partial z}\right)dr + \frac{\mu}{\delta}\int_0^R r\frac{\partial K_z}{\partial z}dr.$$

Applying the boundary condition at $r = R(z)$ yields

$$\kappa RK_r\frac{\partial S_2}{\partial r} = RR'K_z\frac{\partial S_0}{\partial z} - \frac{\mu}{\delta}RR'K_z + \frac{\phi}{2\delta}fRE, \tag{4.18}$$

and then combining the last two equations gives

$$RR'K_z\frac{\partial S_0}{\partial z} - \frac{\mu}{\delta}RR'K_z + \frac{\phi}{2\delta}fRE = \frac{\eta}{2}R^2\frac{\partial S_0}{\partial t} - \int_0^R r\frac{\partial}{\partial z}\left(K_z\frac{\partial S_0}{\partial z}\right)dr + \frac{\mu}{\delta}\int_0^R r\frac{\partial K_z}{\partial z}dr.$$

After simplification this equation reduces to

$$\frac{\phi}{2\delta}fRE = \frac{\eta}{2}R^2\frac{\partial S_0}{\partial t} - \frac{\partial}{\partial z}\int_0^R r\left(K_z\frac{\partial S_0}{\partial z}\right)dr + \frac{\mu}{\delta}\frac{\partial}{\partial z}\int_0^R rK_z dr,$$

and yet further to

$$\eta\frac{\partial S_0}{\partial t} - \frac{2}{R^2}\frac{\partial}{\partial z}\left[G(z)\frac{\partial S_0}{\partial z}\right] = \left(\frac{\phi}{\delta}\right)\frac{fE}{R} - \frac{\mu}{\delta}\frac{2}{R^2}\frac{dG(z)}{dz}, \tag{4.19}$$

where

$$G(z) = \int_0^R rK_z dr. \tag{4.20}$$

Now, the boundary condition (4.5) at $z = 0$ at order ζ is

$$S_0(z,t) = 0, \tag{4.21}$$

while the boundary condition (4.6) at $z = 1$ at order ζ is

$$\left.\frac{\partial S_0}{\partial z}\right|_{z=1} = \frac{\mu}{\delta}. \tag{4.22}$$

Next, we consider the order ζ^3 equation

$$\kappa\frac{1}{r}\frac{\partial}{\partial r}\left(rK_r\frac{\partial S_3}{\partial r}\right) = \eta\frac{\partial S_1}{\partial t} - \kappa\frac{\delta}{\zeta}\psi_1\frac{1}{r}\frac{\partial}{\partial r}\left(rK_rS_0\frac{\partial S_2}{\partial r}\right) - \frac{\partial}{\partial z}\left(K_z\frac{\partial S_1}{\partial z}\right) - \frac{\delta}{\zeta}\psi_1\frac{\partial}{\partial z}\left(K_zS_0\frac{\partial S_0}{\partial z}\right),$$

which upon integrating from 0 to r and evaluating at $r = R(z)$ becomes

$$\begin{aligned}\kappa RK_r\frac{\partial S_3}{\partial r} =& \eta\frac{\partial}{\partial t}\int_0^R rS_1dr - \kappa\frac{\delta}{\zeta}\psi_1RK_rS_0\frac{\partial S_2}{\partial r} - \int_0^R r\frac{\partial}{\partial z}\left(K_z\frac{\partial S_1}{\partial z}\right)dr \\ &- \frac{\delta}{\zeta}\psi_1\int_0^R r\frac{\partial}{\partial z}\left(K_zS_0\frac{\partial S_0}{\partial z}\right)dr.\end{aligned}$$

The corresponding boundary condition at $r = R(z)$ is

$$\kappa RK_r\frac{\partial S_3}{\partial r} = RR'K_z\frac{\partial S_1}{\partial z} + \frac{\mu}{\zeta}\psi_1RR'K_zS_0 - \frac{\phi}{2\zeta}\psi_1RfES_0.$$

Combining the last two equations and using (4.18), then simplifying yields

$$0 = \eta\frac{\partial}{\partial t}\int_0^R rS_1dr - \frac{\partial}{\partial z}\int_0^R r\left(K_z\frac{\partial S_1}{\partial z}\right)dr - \frac{\delta}{\zeta}\psi_1\frac{\partial}{\partial z}\int_0^R r\left(K_zS_0\frac{\partial S_0}{\partial z}\right)dr.$$

Using the fact that S_0 and S_1 have no radial dependence yields

$$\eta\frac{\partial S_1(z,t)}{\partial t} - \frac{2}{R^2}\frac{\partial}{\partial z}\left[G(z)\frac{\partial S_1(z,t)}{\partial z}\right] = -\frac{2}{R^2}H(z), \tag{4.23}$$

where

$$H(z) = -\frac{\delta}{\zeta}\psi_1\frac{\partial}{\partial z}\left[G(z)S_0\frac{\partial S_0}{\partial z}\right], \tag{4.24}$$

and $G(z)$ is as defined in (4.20).

The bottom boundary condition (4.5) at $z = 0$ at order ζ^2 gives

$$S_1(z,t) = 0, \tag{4.25}$$

while the boundary condition (4.6) at $z = 1$ at order ζ^2 gives

$$\left.\frac{\partial S_1}{\partial z}\right|_{z=1} = -\frac{\mu}{\zeta}\psi_1 \, S_0|_{z=1}\,, \tag{4.26}$$

where here the boundary condition forces the following order of magnitude relationship

$$\frac{\mu}{\zeta} = O(1) \tag{4.27}$$

assuming $\psi_1 \sim 1$ and that the derivatives are of $O(1)$ (since there are no steep changes in saturation as the simulations in Section 4.6 show). For the parameter values for *Picea abies* shown in (2.1), the relationship $\mu \sim \zeta$ actually holds.

4.3 Constant Transpiration, Steady State Solution: Connection with Circuit Models

In this section we consider the case when transpiration is constant in time ($E = 1$) so that the solution may be taken at steady state. The solution we obtain is also the time averaged solution for the time-varying periodic transpiration case. We start by integrating the S_0 equation (4.19) using the boundary condition (4.5) at $z = 0$ and (4.6) at $z = 1$, yielding

$$\bar{S}_0(z) = \frac{\phi}{2\delta}\int_0^z \left[\frac{1}{G(z')}\int_{z'}^1 f(w)R(w)dw\right]dz' + \frac{\mu}{\delta}z, \tag{4.28}$$

where $G(z)$ is defined in (4.20).

Similarly, solving (4.23) for constant transpiration and steady state and applying boundary conditions (4.5) at $z = 0$ and (4.26) at $z = 1$ gives

$$\bar{S}_1(z) = -\frac{\delta}{\zeta}\psi_1\int_0^z \bar{S}_0(z')\frac{\partial \bar{S}_0}{\partial z}(z')dz', \tag{4.29}$$

where $H(w)$ from (4.24) is evaluated at $\bar{S}_0$. The first term in $\bar{S}_0$ captures the transpiration effect and the second term captures the gravitational effects. The inner integral is the total transpiration rate above height z' per unit horizontal cross section area at x, which is just the sap flux rate.

Note that if we neglect the gravity term in $\bar{S}_0$, the remaining first term on the right of (4.28) can be thought of as a formula for a resistance circuit

$$\bar{S}_0(z) = \int_0^z \mathcal{I}(z')d\mathcal{R}(z'),$$

where

$$d\mathcal{R}(z') = \left[\int_0^{R(z')} K_z(r, z')dr\right]^{-1} dz',$$

is the resistance of tree slice between $z = z'$ and $z = z' + dz'$. As for

$$\mathcal{I}(z') = \frac{\phi}{2\delta}\int_{z'}^1 f(w)R(w)dw,$$

it is the cumulative transpiration rate from the surface of the trunk between $z = z'$ and $z = 1$. This establishes a connection to circuit models used in tree modeling.

4.4 Time Periodic Transpiration Constant Scalar Conductivity

In this section, we consider a time periodic transpiration function (i.e., where $E(t)$ is periodic) and a constant scalar hydraulic conductivity (i.e., in dimensionless variables, $\kappa = K_r = K_z = 1$). We assume further the exponential form for the trunk radius function $R(z)$ given in (2.20). This will allow us to get a closed form solution for the first two terms in the asymptotic expansion. We use the eventual solutions and numerical experiments to show how transpiration disturbances in one part of the tree propagate through the rest of the tree. Since κ does not appear in the differential equations (4.19) and (4.23) determining S_0 and S_1, any $\kappa \sim 1$ will give exactly the same result. We also assume that the boundary function R is given by (2.20).

Next, we decompose $E(t)$ into its Fourier modes as in (2.16), so that the dimensionless form is

$$E(t) = \Re\left[\sum_{m=0}^{\infty} d_m e^{imt}\right],$$

where $d_0 = 1$, and expand S_0 in terms of its Fourier modes

$$S_0(z, t) = \Re\left[\sum_{m=0}^{\infty} d_m S_0^m(z) e^{imt}\right]. \tag{4.30}$$

The equation for S_0^m is a linear nonhomogeneous ODE

$$\frac{d^2 S_0^m}{dz^2} - 2\alpha\frac{dS_0^m}{dz} - (i\eta m)\, S_0^m = H_0^m(z),$$

where

$$H_0^m(z) = \frac{1}{R^2(z)} \left[-\frac{\phi}{\delta} R(z) f(z) + \begin{cases} \frac{\mu}{\delta} \left(R^2(z)\right)' & ; m = 0 \\ 0 & ; m > 0 \end{cases} \right]. \tag{4.31}$$

The corresponding boundary conditions from (4.21) and (4.22) are

$$\left. \frac{dS_0^m}{dz} \right|_{z=1} = \begin{cases} \frac{\mu}{\delta} & ; m = 0 \\ 0 & ; m > 0 \end{cases}, \tag{4.32}$$

and

$$S_0^m(0) = 0. \tag{4.33}$$

The term S_0^0 has already been determined as the steady state solution $\bar{S}_0$ in (4.28), and in our case simplifies to

$$\bar{S}_0(z) = \int_0^z \frac{1}{R^2(z')} \left[\int_{z'}^1 \frac{\phi}{\delta} f(w) R(w) dw \right] dz' + \frac{\mu}{\delta} z.$$

Considering the homogeneous solution first, for $m > 0$, we get

$$S_{0,h}^m = A_0^{m+} e^{\varrho_m^+ z} + A_0^{m-} e^{\varrho_m^- z}, \tag{4.34}$$

where A_0^{m+} and A_0^{m-} are constants and

$$\varrho_m^{\pm} = \alpha \pm \sqrt{\alpha^2 + im\eta}.$$

Using variation of parameters, the particular solution is

$$S_{0,p}^m = \frac{1}{\varrho_m^+ - \varrho_m^-} \left(\left[\int_0^z H_0^m(z') e^{-\varrho_m^+ z'} dz' \right] e^{\varrho_m^+ z} - \left[\int_0^z H_0^m(z') e^{-\varrho_m^- z'} dz' \right] e^{\varrho_m^- z} \right). \tag{4.35}$$

Then applying the boundary conditions (4.33) yields the following simple relationship between the coefficients:

$$S_0^m|_{z=0} = 0 \implies A_0^{m+} = -A_0^{m-},$$

and the above boundary condition (4.32) leads to

$$A_0^{m-} = -A_0^{m+} = \frac{\int_0^1 \left[\varrho_m^+ \exp\left(\varrho_m^+ (1 - z')\right) - \varrho_m^- \exp\left(\varrho_m^- (1 - z')\right) \right] H_0^m(z')\, dz'}{(\varrho_m^+ - \varrho_m^-)[\varrho_m^+ \exp(\varrho_m^+) - \varrho_m^- \exp(\varrho_m^-)]}. \tag{4.36}$$

Proceeding to the next order in the asymptotic solution for S_1, a similar series expansion

$$S_1(z,t) = \Re \left[\sum_{m=0}^{\infty} d_m S_1^m(z) e^{imt} \right] \tag{4.37}$$

is substituted into (4.23), and (4.19) is used to simplify the right hand side involving S_0. The resulting equation involves three extra nonlinear terms that require individual Fourier series expansions:

$$(S_0)^2 = \Re\left[\sum_{m=0}^{\infty} d_m B_m(z) e^{imt}\right], \quad \left(\frac{\partial S_0}{\partial z}\right)^2 = \Re\left[\sum_{m=0}^{\infty} d_m C_m(z) e^{imt}\right],$$
$$S_0 E(t) = \Re\left[\sum_{m=0}^{\infty} d_m D_m(z) e^{imt}\right].$$

After some further simplification, the ODEs for $S_1^m(z)$ can be written as

$$\frac{d^2 S_1^m}{dz^2} - 2\alpha \frac{dS_1^m}{dz} - im\eta S_1^m = H_1^m(z), \tag{4.38}$$

which are identical to the $S_0^m(z)$ equations except that the right hand side is given by (4.19) as

$$H_1^m(z) = \frac{\psi_1 \delta}{\zeta}\left[\frac{2\alpha\mu}{\delta} S_0^m(z) - \frac{im\eta}{2} B_m(z) - C_m(z) + \frac{\phi f(z)}{\delta R(z)} D_m(z)\right]. \tag{4.39}$$

The corresponding boundary conditions from (4.25) and (4.26) are

$$S_1^m(0) = 0 \qquad \text{and} \qquad \frac{dS_1^m}{dz}(1) = -\frac{\mu\psi_1}{\zeta}\, S_0^m(1).$$

We have already obtained the first term ($m = 0$) in the S_1-series as (4.29) from the steady state solution, while for $m \geqslant 1$ we proceed as before by splitting

$$S_1^m = S_{1,h}^m + S_{1,p}^m, \tag{4.40}$$

where the homogeneous solution is

$$S_{1,h}^m = A_1^{m+} \exp(\varrho_m^+ z) + A_1^{m-} \exp(\varrho_m^- z), \tag{4.41}$$

and the particular solution $S_{1,p}^m$ is identical to (4.35) with H_0^m replaced by H_1^m. Finally, applying the boundary conditions yields the coefficients

$$A_1^{m-} = -A_1^{m+} = \frac{\mu\psi_1}{\zeta} \frac{S_0^m(1)}{\varrho_m^+ \exp(\varrho_m^+) - \varrho_m^- \exp(\varrho_m^-)} + \frac{\int_0^1 \left[\varrho_m^+ \exp\left(\varrho_m^+(1-z')\right) - \varrho_m^- \exp\left(\varrho_m^-(1-z')\right)\right] H_1^m(z')\, dz'}{\left(\varrho_m^+ - \varrho_m^-\right)\left(\varrho_m^+ \exp(\varrho_m^+) - \varrho_m^- \exp(\varrho_m^-)\right)}. \tag{4.42}$$

Next we want to put the leading order solution formulas in a more understandable form that shows how disturbances in transpiration travel along the stem. First define

$$F_0^m(z,t) = \exp\left((|P_m|\cos(\phi_{P_m}))z\right)\cos\left(|P_m|\sin(\phi_{P_m})z + mt + \phi_{A_0^1} + \phi_{d_m}\right)$$
$$G_0^m(z,t) = \exp\left((|P_m|\cos(\phi_{P_m}))z\right)\cos\left(|P_m|\sin(\phi_{P_m})z + mt - \phi_{P_m} + \phi_{d_m}\right)$$

where

$$A_0^{m+} = |A_0^{m+}|\exp\left(i\phi_{A_0^{m+}}\right) \qquad \text{and} \qquad d_m = |d_m|\exp^{i\phi_{d_m}}, \tag{4.43}$$

and

$$P_m = \frac{1}{2}\left(\varrho_m^+ - \varrho_m^-\right), \tag{4.44}$$

then the terms in the Fourier series expansion can be written in the alternate form:

$$\Re\left[d_m S_{0,h}^m(z)\exp\left(imt\right)\right] = |d_m||A_0^{m+}|\exp\left(\alpha z\right)\left[F_0^m(z,t) - F_0^m(-z,t)\right], \tag{4.45}$$

and

$$\Re\left[d_m S_{0,p}^m(z)\exp\left(imt\right)\right] = \\ -\left(\frac{\phi}{\delta}\right)\frac{|d_m|}{|P_m|}\exp\left(\alpha z\right)\int_0^z f(z')\left[G_0^m(z-z',t) - G_0^m(z'-z,t)\right]dz'. \tag{4.46}$$

Notice that in formulas for the saturation leading order term, there are two travelling waves moving in opposite directions for each mode m, and with equal speeds of magnitude

$$\left|\left(\frac{dz}{dt}\right)_m\right| = \frac{m}{|P_m|\sin\left(\phi_{P_m}\right)}. \tag{4.47}$$

We have thus arrived at a description of the leading order mode-dependent speed at which saturation effects of localized spatial and temporal variations in the transpiration are transmitted through the tree, as is illustrated in Figure 4.1: the relaxation time at $z = 0.5z_0$ is numerically given by 3.5 hours in Fig. 4.1c, while asymptotically given by 4.1 hours as we will see in Section 4.8.1; for $\eta = 4.77$ the numerical time shift is 1 hour in Fig. 4.1e, while the asymptotic estimate is 1.44 hours; similarly for $\eta = 14.3$ the numerical shift is 2.7 hour in Fig. 4.1f, while the asymptotic estimate is 2.86 hours. Larger η gives better agreement between the results of the numerical solution and asymptotic formulas). Discrepancies are due to the formulas being first order estimates and due to using formulas which are meant for periodic solutions to estimate properties of transient solutions in the case of spatial travel in (4.47). We have also captured the nonlinear effects of the pressure-saturation relationship on our time dependent solution. Note that although the saturation formulas have been developed for the constant isotropic hydraulic conductivity case where there is no

radial dependence, they still capture the solution in the moderately anisotropic case $\kappa \sim \zeta$, as we will see in Section 4.9.1.

4.5 Steady State, Constant Transpiration and Constant Scalar Conductivity

We next apply the results in the previous two sections to obtain first order approximations for the steady state transpiration case, where we also assume a constant isotropic hydraulic conductivity. For the special case considered here, and since $\bar{S}_0$ and $\bar{S}_1$ have no radial dependence, we need to consider the $\bar{S}_2$ equation (4.17) in order to obtain an expression for the radial velocity. Considering the steady state mode $m = 0$, (4.17) simplifies to

$$\frac{1}{r}\frac{\partial}{\partial r}\left(r\frac{\partial \bar{S}_2}{\partial r}\right) = -\frac{\partial^2 \bar{S}_0}{\partial z^2},$$

so that

$$\frac{\partial \bar{S}_2}{\partial r} = -\frac{r}{2}\frac{\partial^2 \bar{S}_0}{\partial z^2}.$$

Nondimensionalizing expression (2.5) for radial velocity in the case of constant scalar K yields

$$\bar{v}_r \approx \frac{K_0\delta}{\mu\zeta}\left(1 + \delta\psi_1 S\right)\frac{\partial S}{\partial r}.$$

which in contrast with the two leading order terms introduces a simple quadratic radial dependence in $\bar{S}_2$. Then, since $\bar{S}_2$ is the first term with radial dependence, this gives the leading order velocity term as

$$\bar{v}_r \approx -\left(\frac{K_0\delta}{2\mu}\right)\zeta r\frac{d^2\bar{S}_0}{dz^2} = -\left(\frac{K_0\phi\zeta}{2\mu}\right)\frac{r}{2}\frac{d}{dz}\left[\frac{1}{G(z)}\int_z^1 R(w)f(w)dw\right]. \tag{4.48}$$

which obeys the simple estimate

$$\bar{v}_r = O\left(\frac{K_0\zeta\phi}{2\mu}\right). \tag{4.49}$$

As for the vertical velocity component, the dimensionless expression from (2.1) is

$$\bar{v}_z \approx K_0\left(-1 + \frac{\delta}{\mu}\left(1 + \delta\psi_1 S\right)\frac{dS}{dz}\right),$$

and considering the leading order term, this becomes

$$\bar{v}_z = K_0\left(-1 + \frac{\delta}{\mu}\frac{d\bar{S}_0}{dz}\right) = \left(\frac{K_0\phi}{2\mu}\right)\frac{1}{\pi R^2(z)}\int_z^1 2\pi R(z')f(z')dz', \tag{4.50}$$

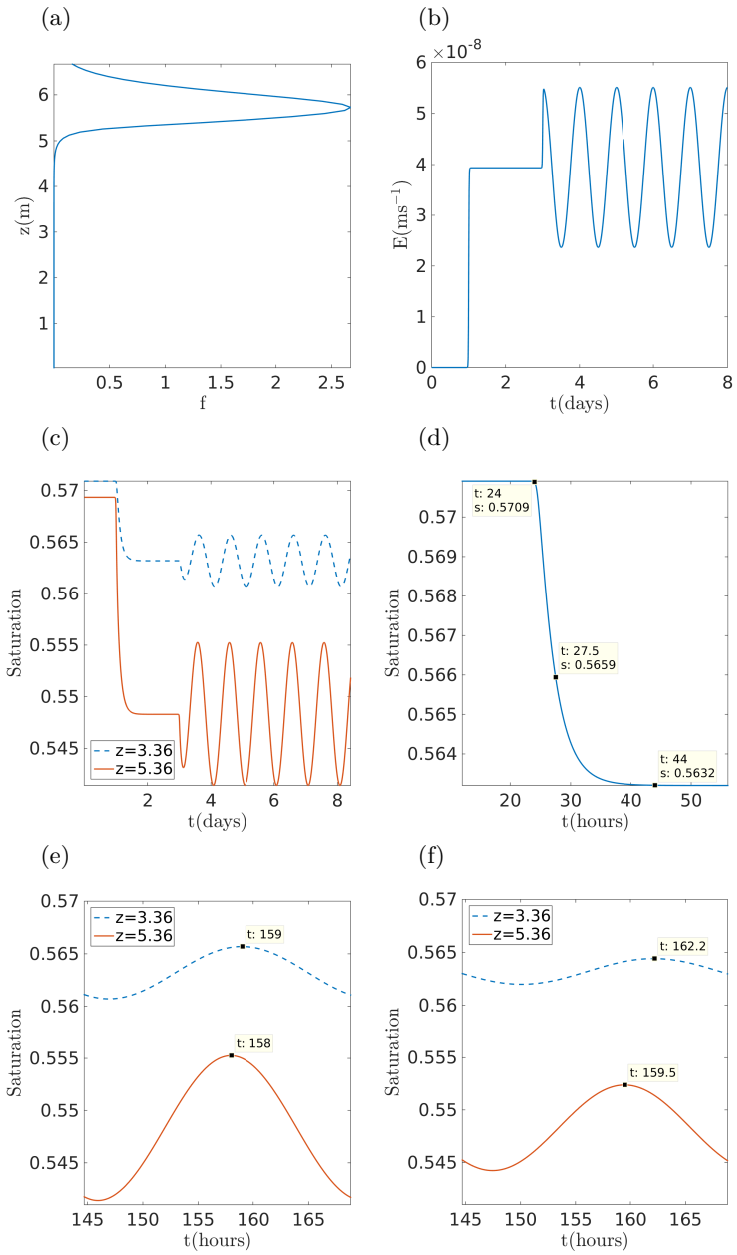

Figure 4.1: Comparison between numerical (plots) and asymptotic estimates (formulas) of relaxation times given by (4.54) and spatial travel between $z = 0.5z_0$ and $z = 0.8z_0$ in (4.47) for a transient disturbance at the top of the tree ($E_0 = 3.94 \times 10^{-8}$, $\kappa = 1$, $a = 1.42$ and $\gamma = 0$). (a) Shifted and rescaled version of original $f(z)$ so that the leaves are concentrated at the upper portion of the tree. (b) Transient disturbance $E(t)$ corresponding to an extreme weather event. (c) Saturation variation as the transpiration is changed with time for $\eta = 4.77$: at $t = 0$ the tree is fully hydrated with no transpiration, at $t = 1$ days constant transpiration is applied, and at $t = 3$ days a Fourier mode $m = 1$ is applied. (d) Zoomed portion of (c) showing the relaxation from zero transpiration to positive transpiration. (e) Zoomed portion of (c) showing the shift in time between two corresponding peaks at two heights. (f) Similar to (e) but for the case of $\eta = 14.3$ (obtained by scaling r_0, z_0 and ψ_o by 3).

so that to leading order

$$\bar{v}_z = O\left(\frac{K_0\phi}{2\mu}\right). \tag{4.51}$$

As a result, the ratio of velocities

$$\frac{v_{r0}}{v_{z0}} \sim \zeta \tag{4.52}$$

where v_{r0} and v_{z0} represent the velocities orders of magnitude in (4.49) and (4.51). This means that the velocity ratio has the same order of magnitude as the stem aspect ratio of the domain.

To illustrate these asymptotic results, we present in Figures 4.2a,b plots of the vertical velocity and saturation, determined using the two leading order terms in the steady state asymptotic solution. In both cases, the solution variables are averaged across the stem cross-section and the corresponding finite-volume numerical solution is included in order to demonstrate the close correspondence. The vertical velocity exhibits the characteristic double peak that is later observed for the variable-transpiration problem in Figure 6.1. To illustrate the relative magnitude of the velocity components, Figure 4.2c depicts the log of the ratio v_r/v_z. Except for a thin boundary layer adjacent to the top boundary the radial component is at least a factor of 100 smaller than the vertical component, which is consistent with our asymptotic estimate of $\bar{v}_r/\bar{v}_z$ in (4.52). The final plot in Figure 4.2d provides a clearer picture of the actual flow direction within the stem by depicting both streamlines and direction field arrows.

4.6 Numerical Validation

In order to validate the asymptotic results, we provide next a comparison between the asymptotic solutions developed in the previous sections and the numerical solution proposed in Chapter 3. Within the asymptotic regime where $\mu \sim \phi \sim \zeta \sim \delta$, the relative error between the numerical solution saturation deficit (i.e. $s_0 - s$) and the corresponding asymptotic value (using two terms in the asymptotic expansion) is of order $O(10^{-4})$ as shown in Figure 4.3, which is the order of the next missing correction term in the asymptotic solution. This gives us confidence in the validity of our asymptotic results and their convergence to the correct order.

As we shift outside of the asymptotic regime by increasing transpiration rate so that $\zeta \sim \mu \ll \phi$, we start seeing some small differences begin to appear as shown in Figure 4.4. Increasing the transpiration even further breaks the model validity, as we get tensions of the order of Megapascals, and at these tensions embolisms would start to form.

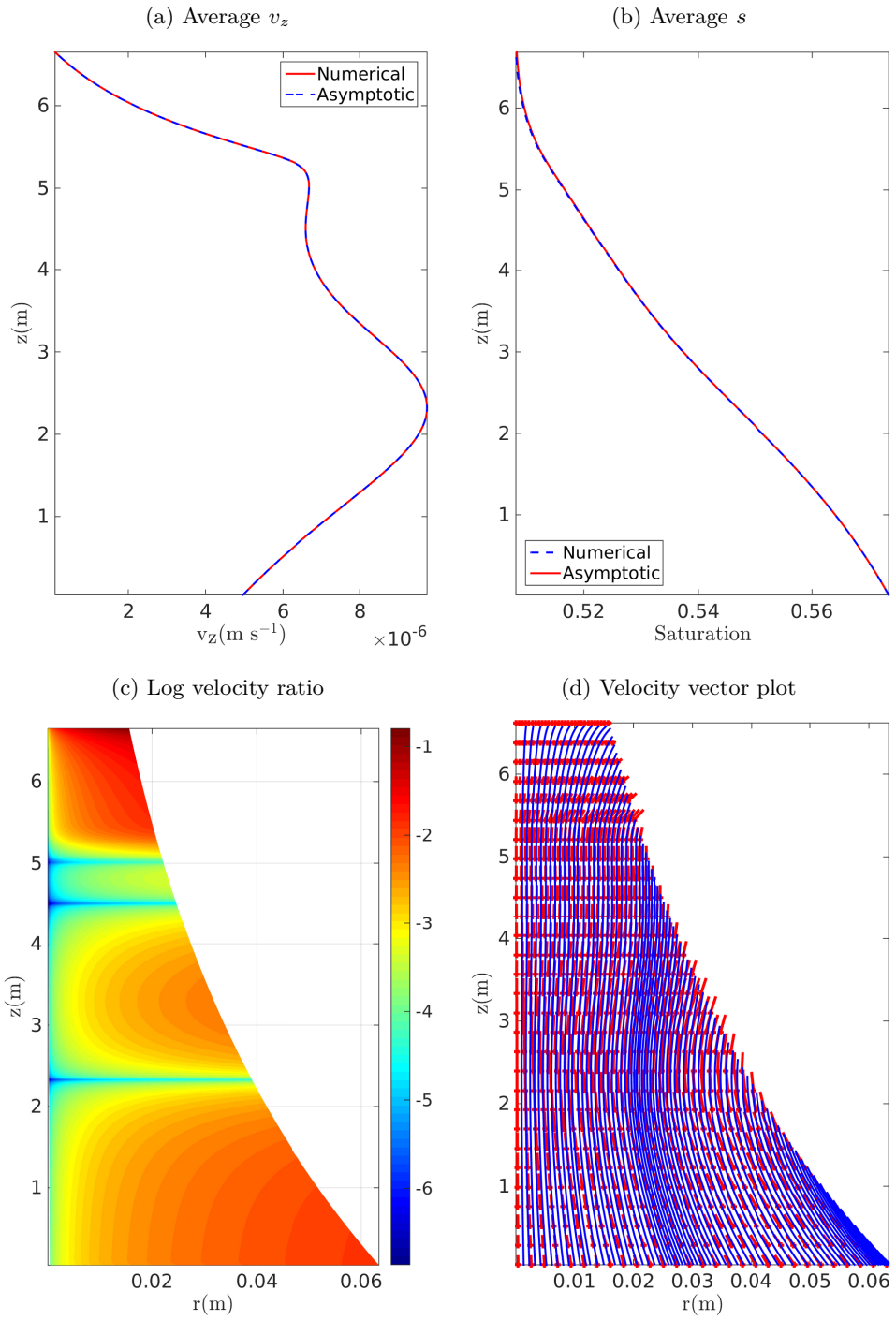

Figure 4.2: Asymptotic and numerical solutions for constant transpiration and isotropic conductivity. (a,b) Comparison of vertical velocity v_z and saturation s (both are averaged across the radius). (c) Log ratio of the velocity components, $\log_{10}|v_r/v_z|$. (d) Velocity field arrows and flow streamlines. Parameters are chosen as in Table 2.1 with $E(t) \equiv E_o = 3.94 \times 10^{-8}$, $\kappa = 1$, $\alpha = 1.42$ and $\gamma = 0$; the asymptotic result is based on the first two terms in the steady-state solution for the isotropic case $\kappa = 1$.

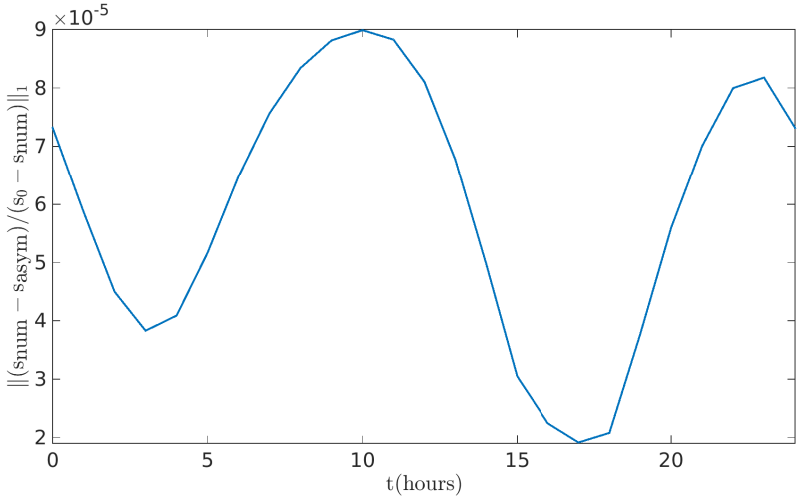

Figure 4.3: L1-norm of difference between numerical and asymptotic solutions relative to the numerical solution within the asymptotic regime where $\mu \sim \phi \sim \zeta \sim \delta$

(a) 3am to 2pm

(b) 2pm to 2am

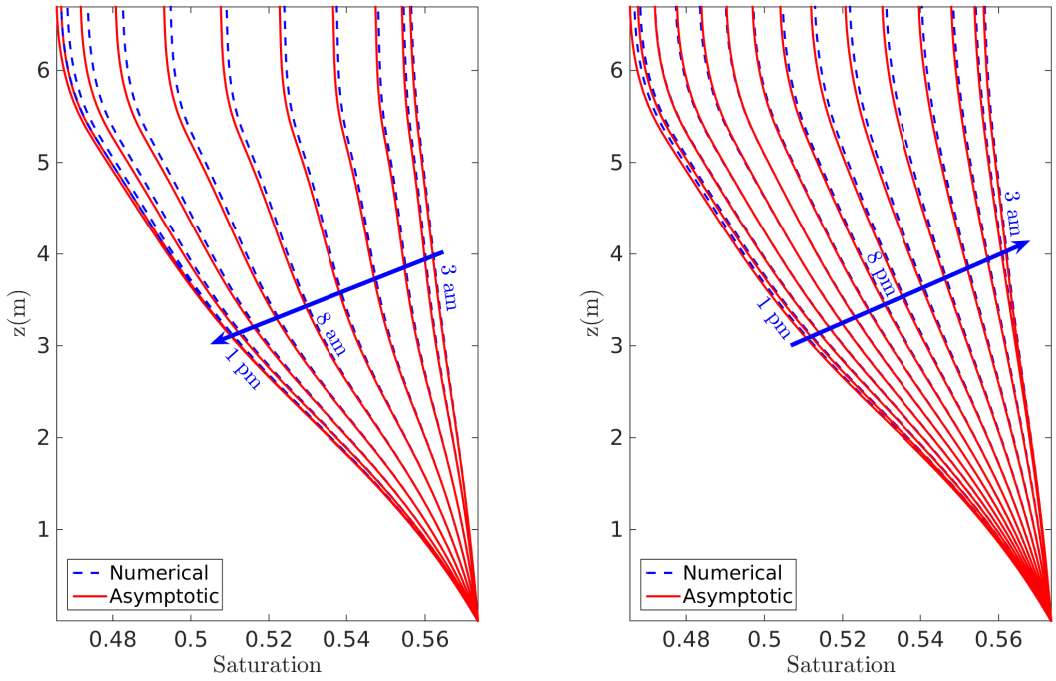

Figure 4.4: Saturation (s) profiles during a 24-hour period, showing the horizontally-averaged numerical solution and asymptotic approximation. For purposes of clarity the profiles over one daily cycle are separated into two roughly 12-hour periods (a,b), since the saturation decreases over the first half day after which it increases again. Here the stem has a taper $\alpha = 1.42$ and a transpiration flux average $E_0 = 3.94 \times 10^{-8}$ (with $\kappa = 1$ and $\gamma = 0$).

4.7 Heartwood Region

The primary reasons for developing this 3D sap flow model are to capture the radial velocity (as well as radial variations in the solution) and to investigate the impact of including a non-conducting heartwood region with $\gamma > 0$. With this in mind, we performed a series of three simulations with different heartwood thickness ($\gamma = 0$, 0.5 and 0.75) and plotted profiles of the computed radial velocities in equation (4.5). Two positive peaks appear in v_r which clearly derive from the local maxima in the transpiration flux, and these are offset by a comparatively large negative radial velocity at the tree base due to root influx. This is a geometric effect that mimics the inward radial tilt of sapwood vessels (which due to stem taper is largest at the base). The effect of this radially-inward flow is accentuated as the thickness of the annulus decreases (i.e., as γ increases) in order to maintain a total mass balance that matches the specified outward transpiration flux.

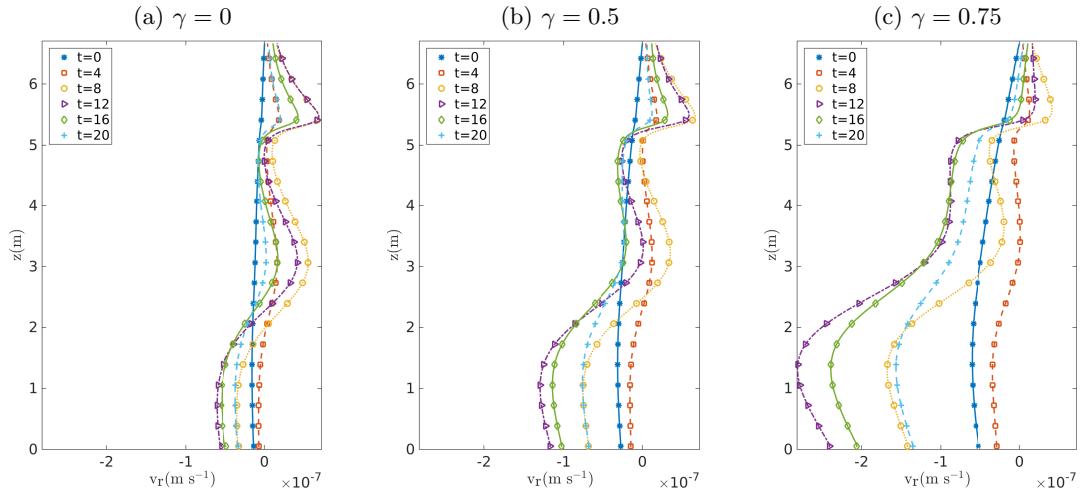

Figure 4.5: Simulations of radial velocity v_r (SI units) shown at various times throughout a diurnal cycle at the middle of the sapwood region, $r = R(z)(\gamma + 1)/2$. Results are shown for three values of heartwood fraction $\gamma = 0, 0.5, 0.75$ and other parameters as in Table 2.1 except $\kappa = 1$.

4.8 Interpretation and Measurement of Dimensionless Parameters

In this section, we provide physical meaning to some of the important dimensionless parameters in our model, and discuss the possibility of measuring them directly instead of measuring the individual dimensional parameters that constitute them. We start by deriving a formula for the relaxation time of the system, and then discuss how transpiration rate and gravity are related to the magnitude of stem water deficit.

4.8.1 Relaxation Time

Consider (4.19) for the special case of constant isotropic hydraulic conductivity ($\kappa = 1$) and exponentially varying boundary (2.20). If we consider the homogeneous part of (4.19) with the substitution $\hat{S}_0 = S_0 - \frac{\mu}{\delta} z$, then

$$\eta \frac{\partial \hat{S}_0}{\partial t} - \frac{1}{R^2} \frac{\partial}{\partial z} \left[R^2 \frac{\partial \hat{S}_0}{\partial z} \right] = 0,$$

with boundary conditions (4.5) and (4.6) becoming homogeneous

$$\hat{S}_0 \Big|_{z=0} = 0 \qquad \text{and} \qquad \frac{\partial \hat{S}_0}{\partial z} \Big|_{z=1} = 0. \tag{4.53}$$

Using separation of variables with $\hat{S}_0(z,t) = Z(z)T(t)$, we get

$$T' = -\frac{\lambda^2}{\eta} T \qquad \text{and} \qquad Z'' - 2\alpha Z' + \lambda^2 Z = 0,$$

where λ is the separation constant. The boundary conditions (4.53) become

$$Z(0) = 0 \qquad \text{and} \qquad Z'(1) = 0,$$

and the eigenvalues are

$$\lambda_k = \sqrt{\alpha^2 + \pi^2 \left(k + \frac{1}{2} \right)^2},$$

with the relaxation time for the slowest mode being

$$T_{relax} = \frac{\eta}{\left(\alpha^2 + \left(\frac{\pi}{2} \right)^2 \right)}. \tag{4.54}$$

For a comparison between the numerical and asymptotic estimates of the relaxation time see Figure 4.1c.

4.8.2 Physical Relevance of the Dimensionless Parameters and Order of Magnitude Relationships

We next highlight four dimensionless parameters that play a prominent role in the asymptotic solution derived in Sections 4.2, 4.3 and 4.4, and which also have straightforward physical interpretations.

Stem aspect ratio, ζ: This parameter plays a central role in the asymptotic analysis as the power series expansion parameter. One of our main conclusions is that the ratio of the radial and vertical velocity components is $\bar{v}_r / \bar{v}_z = O(\zeta)$, which is small regardless of

the conductivity ratio κ. Indeed, this is what allows us to assume $\kappa = 1$ in our asymptotic derivation and still obtain a solution whose leading order term is relevant to the anisotropic case.

Transpiration–flux ratio, $\chi = \phi/\delta$: This ratio appears in several key places throughout the asymptotic derivation wherever transpiration terms appear in the solution, including (4.11),(4.19) and (4.28). Substituting the parameter definitions into χ yields

$$\chi = \frac{2f_0E_0\mu}{K_0\zeta\delta} = \frac{(2\pi r_0 z_0)(f_0E_0)}{(\pi r_0^2)\left(K_0\delta\frac{\psi_0}{nz_0}\right)},$$

and based on the right-most expression χ may be interpreted as the ratio of transpiration flux through the stem surface to vertical sap flux through a circular stem cross-section. For the parameters of interest in this study $\chi \sim 1$, which reflects the balance that must exist between these two fluxes under "normal" daytime conditions. Other limits could nonetheless be considered, such as $\chi \ll 1$ for which the transpiration rate is insufficient to generate an appreciable change in saturation and hence the impact of transpiration will only be felt in higher order terms. On the other hand, imposing a higher transpiration rate with $\chi \gg 1$ could be viewed as shifting the tree into an embolism regime for which saturation is no longer a smooth function, violating a fundamental assumption in our model.

Gravity–saturation ratio, $\xi = \mu/\delta$: This ratio also appears in the governing equation (4.3) and the leading order saturation boundary condition (4.6). In terms of dimensional parameters, $\xi = \frac{nz_0}{\psi_0\delta}$, which can be viewed as a balance between the driving force due to gravity, and the corresponding (saturation-dependent) capillary forces acting on the pore scale in both stem and roots. At night when transpiration is a minimum these two forces must be in balance to prevent water loss into the soil, which is reflected in the fact that $\xi \sim 1$. Recall that our analysis requires $\mu \sim \zeta$ (when $\psi_1 \sim 1$, see (4.26)) which places a restriction on the model parameters. For example, if tree height and radius are scaled up by the same factor so that ζ remains fixed then the ratio ψ_0/n must also increase, meaning that larger trees may develop larger tensions for a given saturation deficit.

Time parameter, η: Consider the formulas for the travelling wave speed (4.47) and relaxation time (4.54) derived in Section 4.8.1. For simplicity, consider a tree with no taper ($\alpha = 0$) in which case the wave speed formula reduces to $(2m/\eta)^{1/2}$ and the relaxation time to $T_{relax} = 4\eta/\pi^2$. Clearly, the parameter η is intimately tied to the time variation of the solution both through the speed of propagation of saturation disturbances along the stem (with characteristic time proportional to $\eta^{1/2}$) and the time for decay of disturbances (proportional to η).

4.8.3 Parameter Estimation

In this subsection we will try to estimate model parameters using our asymptotic results for the case of an exponential boundary with constant isotropic hydraulic conductivity. In the following, we will assume that the geometric parameters ζ and α are available. Assuming the system relaxes relatively fast to the steady state in the absence of transpiration at night ($\eta = O(1)$), the slope of the dimensional saturation line will be equal to $-\frac{\mu}{z_0}$: from (4.28) and (4.1), with $\phi = 0$ (as there is no transpiration)

$$s = s_0 \left(1 - \delta \bar{S}_0\right) = s_0 \left(1 - \mu \frac{z}{z_0}\right).$$

Now for the relaxation parameter η, it can be estimated using (4.54), when there is no transpiration at nighttime, and the maximum of the saturation deficit decays to 63% of its value within a time period of duration roughly equal to T_{relax} (the same happens for the velocity). Next assuming K_0 is known from vulnerability curves, ϕ can be obtained if we estimate f_0 and E_0 (i.e. if we have $f(z)$ and $E(t)$). An estimate of the curves $f(z)$ and $g(z)$ given a few measurements of the vertical sap velocity component, made at several heights and at various times during the day is an interesting inverse problem that we consider in Section 5.

4.9 Additional Special Cases

4.9.1 Anisotropic Hydraulic Conductivity

Until this point, we considered the case where hydraulic conductivity is nearly isotropic with $\kappa \sim 1$. However, typical values of κ lie in the range $10^{-4} - 10^{-2}$ [13, 53]. Having said so, Note that the solution formulas for the vertical variation of saturation are still relevant for the anisotropic case, and they still approximate the radial average of the solution very well (at least in the moderate anisotropy case ($\kappa \sim \zeta$)), which is illustrated in Figure 4.6. Thus, we next consider two anisotropic cases $\kappa = \zeta$ and $\kappa = \zeta^2$ and show that the radial solution variations become significant when conductivity is highly anisotropic ($\kappa = \zeta^2$).

First, we should mention here that we are not claiming any dependence of the ratio of the hydraulic conductivities K_r and K_z on the tree aspect ratio ζ; we are merely considering the case where the ratio is small enough to produce a significant dependence of the vertical velocity v_z on the radial position. Second, this assumption may have merit since experiments done with air to measure the relative permeabilities in the radial and vertical directions [14] support it.

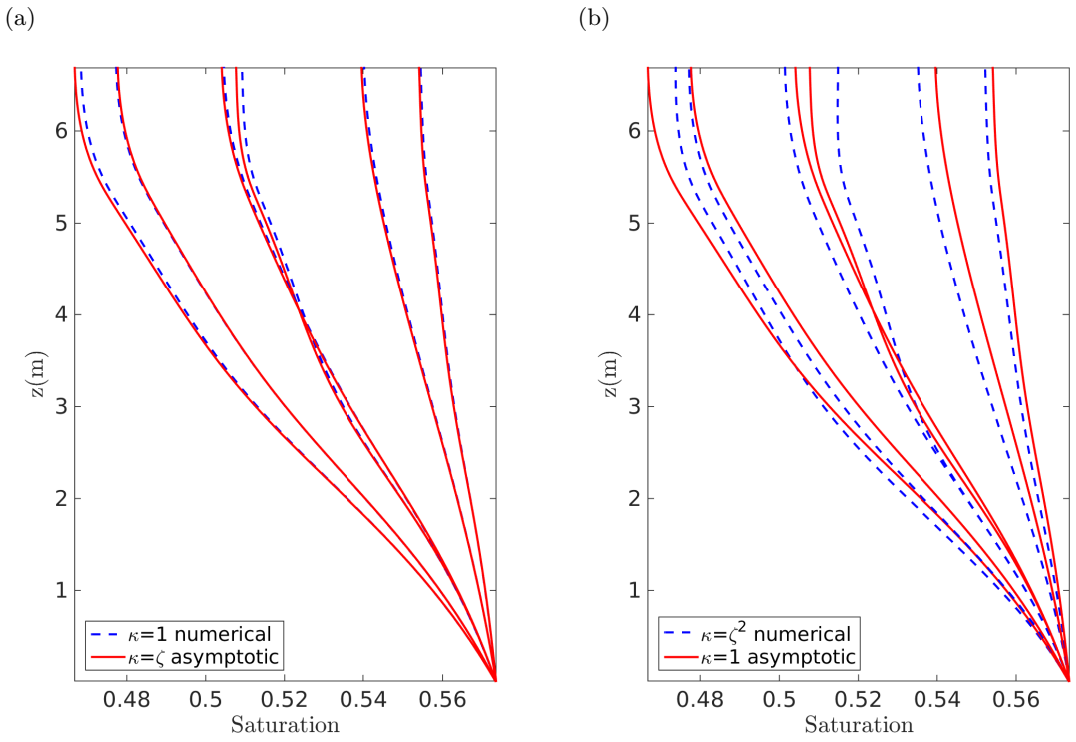

Figure 4.6: Effect of anisotropy for (a) $\kappa = \zeta$, (b) $\kappa = \zeta^2$ on the computed radially-averaged saturation during a diurnal cycle in a tapered stem with $\alpha = 1.42$, $E_0 = 3.94 \times 10^{-8}$ and $\gamma = 0$.

Constant Hydraulic Conductivity with $\kappa = \zeta$:

Considering the case of a moderate anisotropy with $\kappa = \zeta$, the main equation (4.3) becomes

$$\eta\zeta^2\frac{\partial S}{\partial t} = \zeta\frac{1}{r}\frac{\partial}{\partial r}\left(r\left(1+\psi_1\delta S\right)\frac{\partial S}{\partial r}\right) + \zeta^2\frac{\partial}{\partial z}\left(\left(1+\psi_1\delta S\right)\frac{\partial S}{\partial z}\right).$$

Considering the steady-state problem with constant transpiration for simplicity, and expanding using a regular asymptotic series as in (4.12), we get a leading order solution which is independent of r

$$\bar{S}_0 = \bar{S}_0(z),$$

where $\bar{S}_0(z)$ can be determined, and a correction term

$$\bar{S}_1(r,z) = -\frac{\partial^2 S_0}{\partial z^2}\left(\frac{r^2}{4}\right) + h(z),$$

for some $h(z)$ to be determined. Thus for the moderately anisotropic case we start seeing a radial dependence of the saturation in the first correction term.

Constant Hydraulic Conductivity with $\kappa = \zeta^2$:

In the case of a more extreme anisotropy with $\kappa = \zeta^2$, which is more typical of actual trees, (4.3) simplifies to

$$\eta\frac{\partial S}{\partial t} = \frac{1}{r}\frac{\partial}{\partial r}\left(r\left(1+\psi_1\delta S\right)\frac{\partial S}{\partial r}\right) + \frac{\partial}{\partial z}\left(\left(1+\psi_1\delta S\right)\frac{\partial S}{\partial z}\right).$$

Assuming for simplicity a cylindrical domain ($\alpha = 0$), and expanding S using a regular asymptotic series as in (4.12), we obtain the leading order heat equation

$$\eta\frac{\partial S_0}{\partial t} = \Delta S_0.$$

with boundary conditions

$$S_0|_{z=0} = 0, \qquad \left.\frac{\partial S_0}{\partial z}\right|_{z=1} = \frac{\mu}{\delta} \qquad \text{and} \qquad \left.\frac{\partial S_0}{\partial r}\right|_{r=1} = \frac{\phi}{2\delta}f(z).$$

Next using the transformation $\hat{S}_0 = S_0 - \frac{\mu}{\delta}z$, the result is the heat equation

$$\eta\frac{\partial \hat{S}_0}{\partial t} = \Delta \hat{S}_0.$$

with boundary conditions

$$\hat{S}_0\Big|_{z=0} = 0, \qquad \frac{\partial \hat{S}_0}{\partial z}\bigg|_{z=1} = 0 \qquad \text{and} \qquad \frac{\partial \hat{S}_0}{\partial r}\bigg|_{r=1} = \frac{\phi}{2\delta} f(z).$$

Considering the steady state case and using separation of variables, the resulting series solution is

$$\hat{S}_0 = \sum_{n=0}^{\infty} B_n \sin(\lambda_n z) I_0(\lambda_n r), \tag{4.55}$$

where I_0 is the zeroth order modified Bessel function of the first kind

$$B_n = \frac{\phi}{\delta}\left(\frac{1}{\lambda_n I_0'(\lambda_n)}\right)\int_0^1 f(z')\sin(\lambda_n z')dz' \qquad \text{and} \qquad \lambda_n = \frac{\pi}{2}(2n+1).$$

It should be noted here that the steady state case can be solved using the same method applied to the pressure head equation (2.7), without resort to any assumption about the magnitude of the saturation variation δ.

Numerical Results and Discussion:

The effect of anisotropy on the solution is investigated in Figure 4.7 where we compare the simulated vertical velocity profiles for $\kappa = \zeta^p$, using the three exponents $p = 0, 1, 2$ and taking 6 terms in the Fourier–Bessel series for $p = 2$. These results are computed assuming a tree with no taper ($\alpha = 0$) and a constant transpiration rate. For each value of κ, we plot v_z as a function of radius at five different heights corresponding to the points labelled A–E in Figure 2.2. For the isotropic or moderately anisotropic cases ($p = 0, 1$) the velocity remains essentially constant with radius, whereas the extreme case of $p = 2$ exhibits significant radial variations. This is consistent with our asymptotic results which show that radial dependence only enters the leading order solution when $\kappa = \zeta^2$, and may help to explain the radial dependence on velocity that was observed experimentally in [29, 52].

This sequence of simulations was then repeated for a tapered stem with $\alpha = 1.42$ and the corresponding velocity plots are presented in Figure 4.8. Here, we observe similar behaviour to the other cases except that the $\kappa = \zeta^2$ results have a more pronounced radial variation. Even for the the moderately anisotropic case ($\kappa = \zeta$), there is a slight radial dependence visible in the bottom-most v_z profile (location A). It is also interesting to note that introducing a taper with $\alpha = 1.42$ induces a significant drop in the vertical velocity near the tree base owing to the increase in sapwood cross-section there; this should be compared with the untapered case where the vertical velocity profiles increase monotonically with height.

We performed one further validation of our asymptotic results for the extreme case $\kappa = \zeta^2$ by comparing a numerical simulation with the series solution (4.55) truncated at 6 terms. The relative difference in the saturation deficit $s_0 - s = \delta S$ between the asymptotic

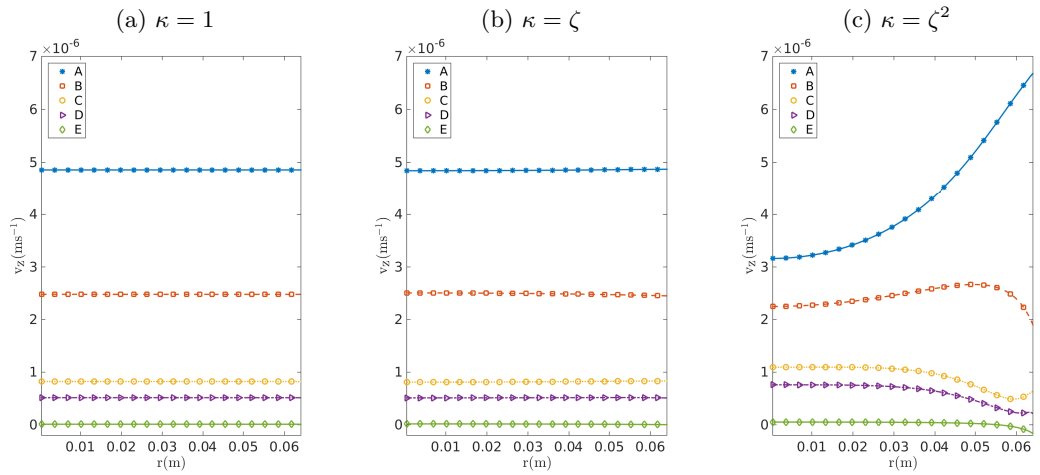

Figure 4.7: Effect of anisotropy ($\kappa = 1$, ζ, ζ^2) on the computed velocity in a non-tapered stem with $\alpha = 0$ and $\gamma = 0$. The vertical velocity profiles are simulated numerically using a constant transpiration rate $E_0 = 3.9375 \times 10^{-8}$, and depicted at heights labelled A–E on the left plot of Figure 2.2.

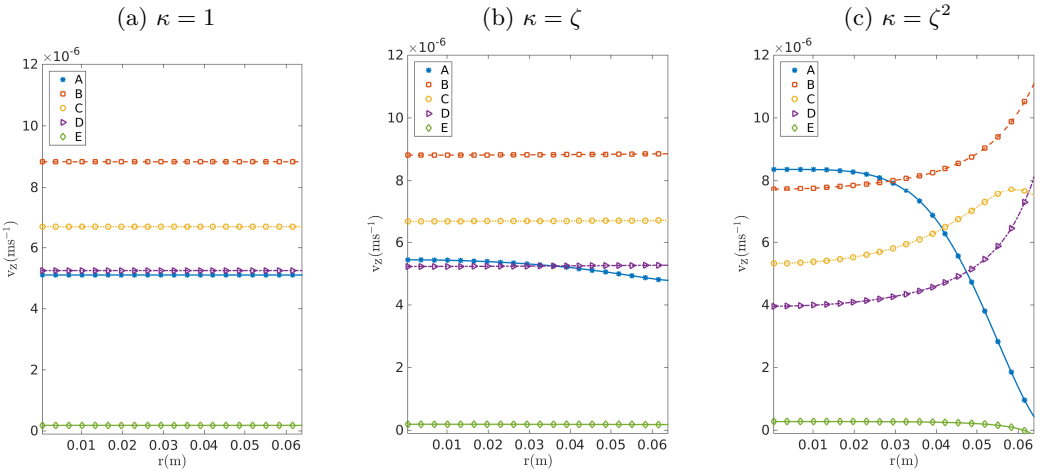

Figure 4.8: Same as Figure 4.7 for a tapered stem with $\alpha = 1.42$.

and numerical solutions is of order 10^{-2}, which is the same order as the missing correction term in the asymptotic expansion of S, as expected.

4.9.2 Case $\eta \not\sim 1$

Here, we consider the cases where the tree is much smaller or much larger than the Norway spruce in Table 2.1. Owing to the quadratic dependence of the time parameter η on height, we expect changes in height to have drastic effects on η value, and consequently a drastic effect on the relaxation time. Considering the same case as in Section 4.4, but with the assumption of $\eta \sim \zeta$ instead of $\eta \sim 1$, we get

$$S_0 = S_0(z, t),$$

where $\bar{S}_0(z)$ can be determined and

$$S_1^m(r, z) = im\eta\zeta \left(\frac{r^2}{4}\right) S_0^m(z) + h(z),$$

for mode $m > 0$ and for some $h(z)$ to be determined. Thus the time varying modes of the first correction now have radial dependence.

Assuming $\eta \ll 1$ is not as interesting as $\eta \sim 1$, as the resulting leading order term is then similar to the steady state case (4.28), except for the factor $E(t)$

$$\bar{S}_0(z) = \frac{\phi}{2\delta} E(t) \int_0^z \left[\frac{\int_{z'}^1 f(w)R(w)dw}{G(z')} dr \right] dz' + \frac{\mu}{\delta} z, \tag{4.56}$$

where $G(x)$ is defined in (4.20). This means that as the radius of the tree decreases, capacitative effects become negligible and resistance dominates. In other words, small tree branches may be assumed to be much more resistive than capacitative.

It should be noted here that we can always maintain $\eta \sim 1$ by modifying the time period τ, which means that for larger trees, τ should be larger, and thus the time variations become seasonal variations instead of daily variations. However, longer time periods can mean occurrence of both growth and embolism, in which case our model may not hold.

4.9.3 Branching from Tree Crown

Consider the case where branches emanate from the crown of the tree, with minimal branching along the tree stem. The reason for considering this situation, besides its physical relevance, is that it allows us to compare the effects of anisotropy on sap flow with the situation where the branches are spread out along the stem. For this case, we will assume the specific

functional forms

$$l(z) = \frac{1}{2}\left(1 + \frac{2}{\pi}\arctan\left(100\left(\frac{z}{z_0} - 0.8\right)\right)\right), \tag{4.57}$$
$$\lambda(z) = 1,$$

where we are assuming that there is no shading effect. Figure 4.9 shows the resulting transpiration function $f(z)$.

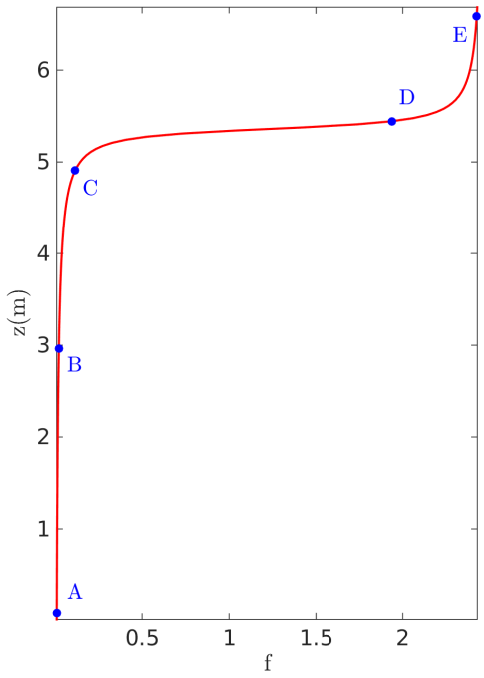

Figure 4.9: Transpiration flux spatial dependence function $f(z)$ resulting from the modification (4.57) for a non-tapered stem with $\alpha = 0$ and $\gamma = 0$. The time constant transpiration rate is $E_o = 3.94 \times 10^{-8}$.

Figure 4.10 shows a comparison between the vertical velocity component for the three cases of hydraulic conductivity $\kappa = 1, \zeta, \zeta^2$ for a cylindrical geometry. Notice the extreme radial change in the vertical velocity at the branching points C and D at the upper part of the tree for $\kappa = \zeta^2$. The other two cases $\kappa = 1, \zeta$ do not show much radial change. Figure 4.11 shows a comparison between the radial velocity component for the same three cases, where the radial velocity dependence on height is plotted at three depths 1/4, 1/2 and 3/4 along the stem. Notice the gradual increase in the radial velocity with height in the anisotropic case $\kappa = \zeta^2$ in comparison to the other two cases, where the radial velocity suddenly increases to its maximum at the start of branching. The reason for this is that in order to satisfy the transpiration demand at the tree upper part, there is easy access to the

water supply at greater depths in the isotropic case in comparison to the anisotropic case $\kappa = \zeta^2$.

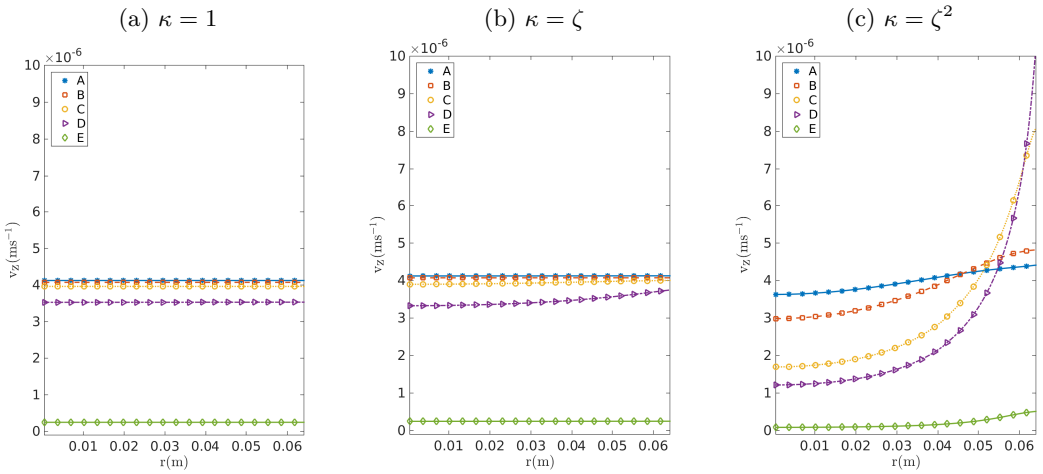

Figure 4.10: Effect of anisotropy ($\kappa = 1$, ζ, ζ^2) on the computed velocity in a non-tapered stem with $\alpha = 0$ and $\gamma = 0$. The vertical velocity profiles are simulated numerically using a constant transpiration rate $E_o = 3.94 \times 10^{-8}$, and depicted at heights labelled A–E on Figure 4.9. The curves for heights A–C are superimposed for the left and middle plots.

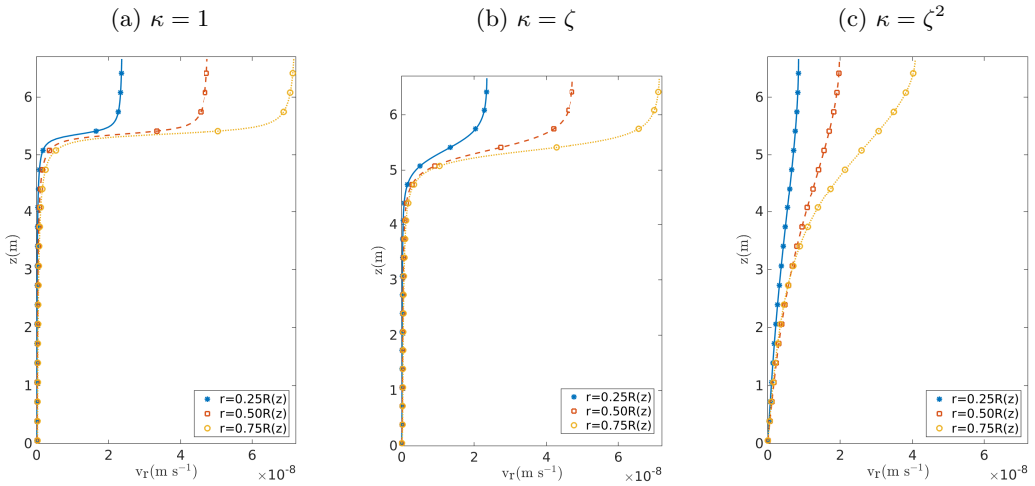

Figure 4.11: Effect of anisotropy ($\kappa = 1$, ζ, ζ^2) on the computed velocity in a non-tapered stem with $\alpha = 0$ and $\gamma = 0$. The radial velocity profiles are simulated numerically using a constant transpiration rate $E_o = 3.94 \times 10^{-8}$, and depicted for $f(z)$ in Figure 4.9.

Chapter 5

The Inverse Problem: Estimating Transpiration from Sap Flux Measurements

Thus far, we have derived formulas for the saturation and velocity inside the tree trunk in terms of a prescribed transpiration function at the trunk surface. Now we turn to the more practical problem of estimating the transpiration function $Q(z,t)$, given discrete measurements of the sap velocity inside the trunk. To do this, we first expand the spatial $f(z)$ and time $E(t)$ components of the transpiration function in terms of its Fourier modes. Then we substitute a truncated version of these representations into our derived saturation formulas (and thus velocities); this in effect turns our estimation problem into a finite dimensional one of estimating the Fourier coefficients. Carefully picking a discrete set of height and time points for velocity measurement, we obtain a linear algebraic system set of equations that recovers $f(z)$ given $E(t)$ or vice versa. Finally, in order to recover both $f(z)$ and $E(t)$ simultaneously we propose an energy functional formulation that performs well in this respect. Before all this let us start with a general discussion of why measurement of parameters in trees is problematic.

5.1 Measurements of Relevant Physical Quantities

So are our model variables, parameters and empirical relationships such as pressure-saturation relationship readily measurable? The answer is yes and no (see [30] for a recent review of some measurement methods and associated difficulties). Many of the practical measurement techniques are destructive, invasive and of low resolution, and the non-invasive high resolution techniques are expensive and not practical for the field. Measuring the pressure-saturation (or pressure-volume ([31] uses pressure chamber)) relationship is destructive, as the trees need to be harvested before the measurement (see [30] for some difficulties in mea-

suring the pressure). [68] and [47] propose methods to measure water content (or saturation) without harvesting the tree. This is also the case for measuring the hydraulic conductivity (see [17]). As for the measurement of the sap flow velocity, probes are inserted into the tree trunk, which may disrupt the flow, and is limited to low spatial resolution (see [41] and [68] which use a heat pulse method). It is also limited by the minimum velocity it can measure (see [64] and [19] for low velocities determination). Although cavitation is not accounted for by our model, we indicate that [65] measures the acoustic emissions generated during cavitation events, which does not show the location of the cavitation. Branches and leaves distributions could conceivably be measured through photographing from multiple angles and subsequent image processing. Measuring transpiration can be done using a porometer as described by [56]. Finally, for non-invasive measurements using plant dedicated MRI techniques, see [67].

5.2 Deriving the Linear Algebraic System

Consider the case of isotropic hydraulic conductivity $K = 1$, with exponential trunk taper function (2.20). The question is how can we estimate the leaf area density $f(z)$ (i.e. the vertical transpiration profile) from sap flux $v_z|_{z=z_i,t=t_i}$ measurements at multiple heights and times. We begin with a simplifying assumption that changes in leaf density with height are negligible near the bottom and top of the stem, with Fourier expansion

$$f(z) = \sum_n b_n \cos(n\pi z), \tag{5.1}$$

where the b_n are constants to be determined. Now v_z is given in (4.50) to first order as

$$v_z = K_0 \left(-1 + \frac{\delta}{\mu} \frac{dS_0}{dz} \right),$$

and the z derivative of saturation is given by (4.30) as

$$\frac{dS_0}{dz} = \Re \left[\sum_m d_m \frac{dS_0^m}{dz} e^{imt} \right],$$

where the S_0^m have already been derived in (4.28), (4.34) and (4.35). Thus we obtain (using $d_0 = 1$)

$$\begin{aligned}
\frac{d\bar{S}_0}{dz} &= \frac{\phi}{\delta}\sum_n b_n W_n^1(z) + \frac{\mu}{\delta},\\
\frac{dS_{0,h}^m}{dz} &= A_0^1 W_m^2(z),\\
\frac{dS_{0,p}^m}{dz} &= \frac{\phi}{\delta}\sum_n b_n W_{nm}^3(z),\\
A_0^1 &= \frac{\phi}{\delta}\sum_n b_n W_{nm}^4,
\end{aligned}$$

where

$$\begin{aligned}
W_n^1(z) &= e^{2\alpha z}\int_z^1 \cos(n\pi z')e^{-\alpha z'}dz',\\
W_m^2(z) &= \left(\varrho_m^+ e^{\varrho_m^+ z} - \varrho_m^- e^{\varrho_m^- z}\right),\\
W_{nm}^3(z) &= -\frac{1}{2P_m}\left(\left[\int_0^z \cos(n\pi z')e^{-P_m z'}dz'\right]\varrho_m^+ e^{\varrho_m^+ z}\right.\\
&\quad \left. - \left[\int_0^z \cos(n\pi z')e^{P_m z'}dz'\right]\varrho_m^- e^{\varrho_m^- z}\right),\\
W_{nm}^4 &= \frac{\varrho_m^+\left[\int_0^1 \cos(n\pi z')e^{-P_m z'}dz'\right]e^{\varrho_m^+} - \varrho_m^-\left[\int_0^1 \cos(n\pi z')e^{P_m z'}dz'\right]e^{\varrho_m^-}}{2P_m\left[\varrho_m^+ e^{\varrho_m^+} - \varrho_m^- e^{\varrho_m^-}\right]}.
\end{aligned}$$

Thus assuming b_n and d_m are both real

$$\frac{dS_0}{dz} = \frac{\mu}{\delta} + \Re\left[\sum_m d_m\left(\frac{\phi}{\delta}\sum_n b_n W_{nm}(z)\right)e^{imt}\right] = \frac{\mu}{\delta} + \frac{\phi}{\delta}\sum_{n,m} b_n d_m \Re\left[W_{nm}(z)e^{imt}\right],$$

where

$$W_{nm}(z) = \begin{cases} W_n^1(z) & ; m = 0,\\ W_m^2(z)W_{nm}^4 + W_{nm}^3(z) & ; m > 0, \end{cases}$$

and finally the vertical velocity is

$$v_z(z,t) = K_0\frac{\phi}{\mu}\sum_{n,m} b_n d_m \Re\left[W_{nm}(z,t)e^{imt}\right]. \tag{5.2}$$

Note that the velocity is bilinear in the Fourier coefficients b_n and d_m. Thus if we are given the temporal component of transpiration $E(t)$ (or equivalently d_m) and a spatially uniform set of velocity measurements $\{v_z(z_k,t_0)\}_k$ for $0 < z < 1$ at some fixed time t_0, we

can use least squares to estimate the spatial component of transpiration $f(z)$ (or equivalently b_n). Similarly, if we are given the spatial component of transpiration $f(z)$ (or equivalently b_n) and a temporally uniform set of velocity measurements $\{v_z(z_0', t_l')\}_l$ at some fixed height z_0 and for $0 < t < \pi$, we can use least squares to estimate the temporal component of transpiration $E(t)$ (or equivalently d_m). This naturally leads to the algorithm we will use next to estimate both b_n and d_m when we have both sets of velocity measurements.

5.3 Optimizing to Determine the Transpiration Function

Next we will describe an algorithm to estimate the transpiration function $Q(z,t) = f(z)E(t)$ from a finite set of velocity measurements. We will assume that the spatial component of transpiration $f(z)$ has zero derivatives at $z = 0, 1$ (or equivalently has a cosine Fourier expansion (5.1)), and that the temporal component $E(t)$ is symmetric about π (i.e., the Fourier coefficients d_m are real). These assumptions are not restrictive physically as we expect low leave density at the stem extremities and some kind of temporal symmetry about some point in the day. So we want to estimate the Fourier coefficients b_n and d_m given a set of velocity measurements, where the measurements are divided into two sets as proposed at the end of Section 5.2.

First we rewrite (5.2) as

$$v_z(z,t) = K_0 \frac{\phi}{\mu} \sum_n \sum_m b_n G_{nm}(z,t) d_m = K_0 \frac{\phi}{\mu} b^T G(z,t) d, \tag{5.3}$$

with

$$G_{nm}(z,t) = \Re \left[W_{nm}(z) e^{imt} \right].$$

Now define the following four matrices and two column vectors

$$(M_{bz}(d))_{k,n} = \left(G(z_k, t_0)d\right)^T, \quad (M_{dz}(b))_{k,m} = b^T G(z_k, t_0), \quad (V_z)_k = \frac{\mu}{K_0 \phi} v_z(z_k, t_0),$$

and

$$(M_{bt}(d))_{l,n} = \left(G(z_0', t_l')d\right)^T, \quad (M_{dt}(b))_{l,m} = b^T G(z_0', t_l'), \quad (V_t)_l = \frac{\mu}{K_0 \phi} v_z(z_0, t_l),$$

where the two sets of measurements points $\{z_k, t_0\}_{k=1}^N$ and $\{z_0', t_l'\}_{l=1}^M$ are as defined in Section 5.2. Thus

$$V_z = M_{bz}(d)b = M_{dz}(b)d \qquad \text{and} \qquad V_t = M_{dt}(b)d = M_{bt}(d)b. \tag{5.4}$$

Now consider the following energy functional

$$E_{bd} = E_b + \omega E_d,$$

where ω is a free parameter and

$$E_b = \frac{1}{2}\left\|V_z - M_{bz}(d)b\right\|^2 \qquad \text{and} \qquad E_d = \frac{1}{2}\left\|V_t - M_{dt}(b)d\right\|^2.$$

Here, E_b is the energy for the least squares problem for determining b given d and uses the spatially uniform set of measurements $\{z_k, t_0\}_{k=1}^N$, while E_d is the energy for the least squares problem for determining d given b and uses the temporally uniform set of measurements $\{z_o, t_l\}_{l=1}^M$. Thus we combine both these energies into E_{bd} in order to estimate both b and d.

We seek to solve the following optimization problem (which is convex in each of b and d separately)

$$\min_{Bb\geq 0, Dd\geq 0} E_{bd}(b,d),$$

where B and D are matrices that transform from the Fourier cosine coefficients b and d to the discretized transpiration functions $f(z_k)$ and $E(t_l')$ respectively (see Equations (5.1) and (2.16)).

$$B_{kn} = \cos(\pi n z_k) \qquad \text{and} \qquad D_{lm} = \Re\left[e^{imt_l'}\right].$$

Taking the derivatives of the energy E_{bd} and to zero gives

$$0 = \frac{\partial E_{bd}}{\partial b} = -M_{bz}^T(d)V_z + M_{bz}^T(d)M_{bz}(d)b - \omega M_{bt}^T(d)V_t + \omega M_{bt}^T(d)M_{bt}(d)b, \tag{5.5}$$

$$0 = \frac{\partial E_{bd}}{\partial d} = -\omega M_{dt}^T(b)V_t + \omega M_{dt}^T(b)M_{dt}(b)d - M_{dz}^T(b)V_z + M_{dz}^T(b)M_{dz}(b)d. \tag{5.6}$$

Now we start with an initial random b and d pairs (uniformly sampling each element), and solve the first equation for b assuming d is known, and the second equation for d assuming b is known, in an iterative Gauss-Seidel fashion. In each step we ensure that $f(z_k)$ and $E(t_l')$ are positive by transforming from the Fourier coefficients b and d, projecting the result by changing any negative values into zero, and then transforming back into b and d

$$b = (B^TB)^{-1}B^T\max(Bb, 0) \qquad \text{and} \qquad d = (D^TD)^{-1}D^T\max(Dd, 0).$$

We tested our algorithm for $\alpha = 1.42$, $\eta = 1$ and $N = M = 5$ (we lumped $K_0\phi/\mu$ with the velocity measurements in (5.2)). Since we do not have a dataset where both velocity and transpiration measurements are available, we generated random Fourier coefficients b and d by uniformly sampling each coefficient from the interval $[-1, 1]$ then shifting the resulting functions $f(z)$ and $E(t)$ to become positive. We then checked the resulting matrices M_{bz}

and M_{dt} and found out that with proper choices of t_0 and z_0 we can always get the condition numbers of these matrices to about 35 or less. We can sometimes get significantly better condition numbers by further choosing a nonuniform spatial and temporal distribution of the velocity measurement points.

To illustrate the algorithm, we start with a known b and d (red curves in Figures 5.1 and 5.2), calculate the velocities V_z and V_t using (5.4) (the forward problem), and then multiply by a normally distributed noise of mean 1 and standard deviation 3% and 10%. Next we use the algorithm to recover $f(z)$ and $E(t)$ (blue curves) from the noisy V_z and V_t. We tested with 5 coefficients in both space b and time d, and for square matrices M_{bz} and M_{dt} (i.e. the number of measurement points is equal to the number of coefficients for both b and d). For B and D, we used 200 uniformly spaced points in space and in time. First, we notice that the accuracy of the recovery depends on the the location of our measurement points, with the best points being in general the ones that give values of v_z that are well separated and distributed over a wide range, which makes them less sensitive to noise. Second, there were no problems as far as convergence since the the energy E_{bd} is separably convex in (b, d).

(a) $f(z)$ (b) $E(t)$

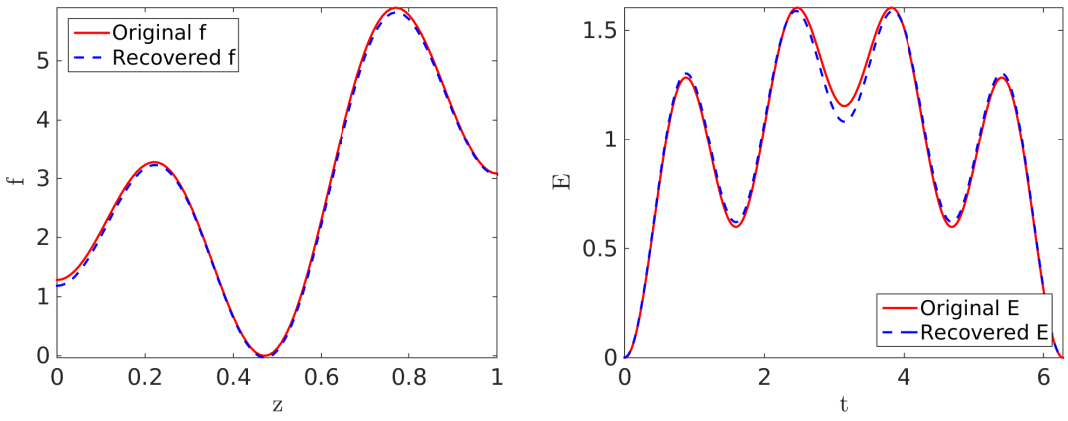

Figure 5.1: (a) transpiration vertical profile function $f(z)$, (b) leaf transpiration flux function $E(t)$ (right). We start from a known $f(z)$ and $E(t)$ (red), we then add 3% noise and attempt to recover the functions (blue).

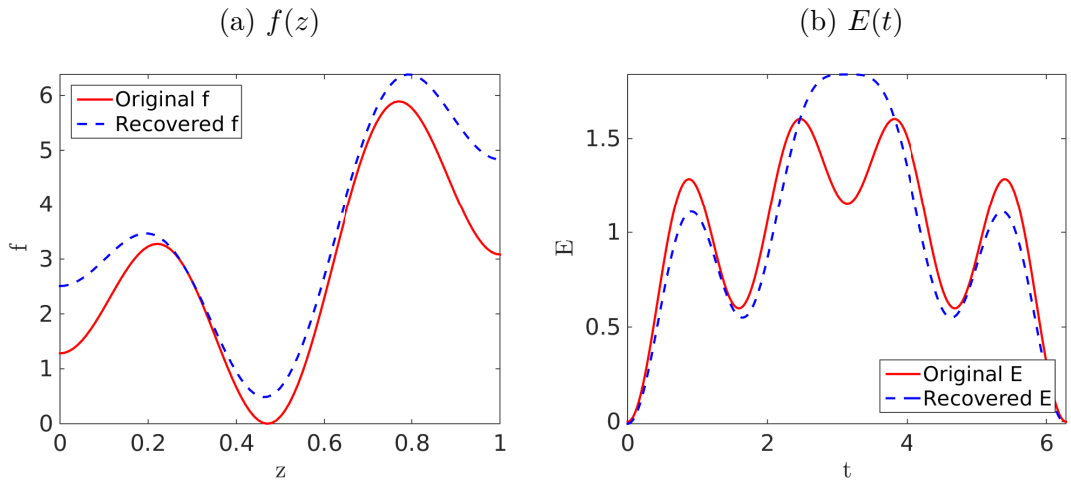

Figure 5.2: (a) transpiration vertical profile function $f(z)$, (b) leaf transpiration flux function $E(t)$ (right). We start from a known $f(z)$ and $E(t)$ (red), we then add 10% noise and attempt to recover the functions (blue).

Chapter 6

Experimental Verification

6.1 Norway Spruce

In addition to verifying our asymptotic solution, we compare our results to Chuang et al. [12], especially to the experimental data they used. Figure 6.1 shows a simulation result that is compared with their experimental data. The deviation of our curves from the data points is mainly due to the simplifying assumption that the transpiration function $Q(z,t)$ can be factored along the coordinates z and t, and our approximation of the factors $f(z)$ and $E(t)$ by digitizing figures.

6.2 Douglas fir

An attractive tree to compare our model to is the Douglas fir, since the authors in [18] and [19] produce the values of most of the model parameters for this tree, and also have indirect measurements of the radial conductivity and the radial velocity. The experimental relationship between pressure and saturation, as shown in Figure 4 of [19], is linear

$$\psi(s) = \psi_0(s - s_0),$$

where ψ_0 is the reciprocal of the slope multiplied by the factor $\frac{100 s_0}{\rho g}$; this gives $\psi_0 \approx 1.8 \times 10^3$. As for the hydraulic conductivity, it is highly anisotropic, and the axial component K_z ranges between 2.5×10^{-5} and 5.3×10^{-5}, according to [19, Tab. 1], while the radial component K_r ranges between 1×10^{-8} and 2.2×10^{-8} (depending on the radial depth in the trunk). As for the stem dimensions, $r_0 = 0.1$, $z_0 = 16$ and $\gamma \approx 0.485$. Figure 2 in [25] gives some idea of the variability in the leaf distribution. Figure 1 in [19] gives the vapour pressure deficit diurnal variation which is roughly correlated with the diurnal variation of transpiration $E(t)$. The measurements in [19] for the radial sap flow, radial pressure gradients, and hydraulic conductivity is made at a height of 1 m above the ground.

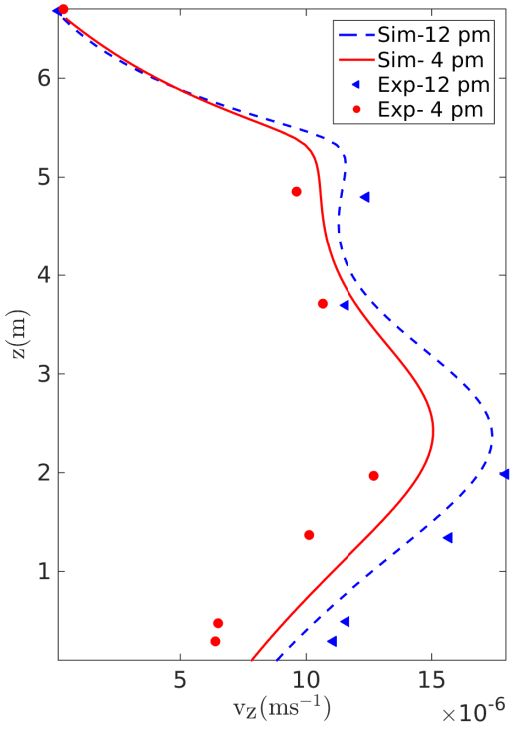

Figure 6.1: Comparison of 3D numerical simulations with the experimental data in Chuang et al. [12] for Norway spruce. Vertical sap flux from simulations (Sim) and experiments (Exp) at two different times, converted to SI units.

Now amending the numerical code to allow for the approximation of a linearly decaying tree trunk radius with respect to height (consistent with [25, Fig. 2])

$$R(z) = \frac{r_0}{z_0}\,(z_0 - z)\,,$$

which can be done by replacing C by $-\frac{\zeta}{R(z)}$ in the transformed equations in Section 3.1. The simulations for parameter values $K_z = 3.22 \times 10^{-5}$ and $K_r = 1.13 \times 10^{-8}$ from [19] (see Figure 6.2a) give an ellipse that is nearly a straight line, which is traversed in the clockwise direction. Reducing the hydraulic conductivity by an order of magnitude (i.e., multiplying by 0.1), gives a pattern in Figure 6.2b very similar to what can be seen at the bottom of [19, Fig. 5] (replicated below at the bottom of Figure 6.3); in both cases, the ratio of the maximum radial gradient to the maximum axial gradient (the tip of the ellipse) is about 20, which is close to the value that can be extracted from [19, Fig. 5], which is about 25. However, we were not able to obtain the deviation from the elliptic shape shown at the top of Figure 6.3 for transpiration at a different day. In any case, the leaf distribution was assumed to decay linearly with height, and the transpiration scaling parameter E_0 was a free parameter; the results were not sensitive to these unknowns, as long as we assume that the branches (and leaves) do not appear at heights below 1 m. Above the lower limit of branches, various other patterns do appear (not shown) when we plot the axial versus the radial pressures gradients, and at some heights we get a knot, and two different points for the maxima of the radial and axial pressure gradients.

(a) Large K (b) Small K

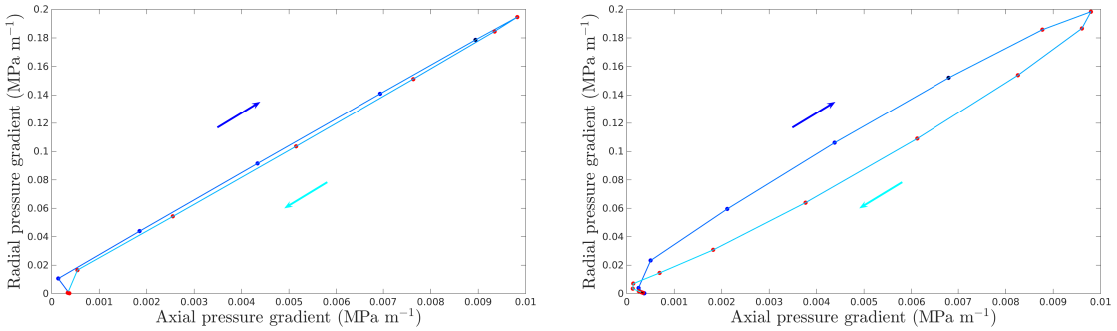

Figure 6.2: Average axial pressure gradient (calculated between the bottom and top of the tree) versus the radial pressure gradient simulation results at $z = 1$ m through a diurnal cycle, for parameter values (a) $K_z = 3.22 \times 10^{-5}$ and $K_r = 1.13 \times 10^{-8}$ [19], and (b) one tenth of these values. Hourly pressure gradients up till noon (blue circles) and in the afternoon (red circles). Note the clockwise cycle (not as prominent in the left plot).

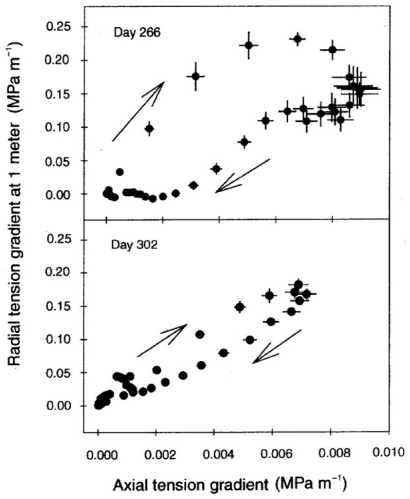

Figure 6.3: Experimental results from Domec [19] at two different days with the similar parameter values as the ones used to generate Figure 6.2.

Chapter 7

Conclusion

In this paper, we extended and generalized the work done by Chuang et al. [12] to a 3D axisymmetric porous medium model, with general radius dependence on height, periodic transpiration function and smooth nonlinear pressure head function, using only minimal assumptions. Using the two leading terms of the asymptotic expansion, and thus capturing the nonlinearity of the pressure head, we were able to derive formulas for saturation and velocity spatial and temporal dependence; we were also able to describe the various possible flow regimes by means of several dimensionless parameters of the model. Using asymptotic results and simulations, we were able to study the effects of hydraulic conductivity anisotropy in relation to radial variation of the sap vertical velocity component, which gives a possible explanation to the observed radial variations in the experimental results of [52] and [29]. As for the inverse problem of determining the transpiration functions from a spatially and temporally discrete set of noisy measurements of the sap flux inside the tree trunk, we devised an optimization technique that uses the formulas of the forward problem, and performs well even with a significant amount of noise added to the signal. The vertical mass flux was shown to replicate the results of the 1D model, which agree with the experimental results quoted in [12] for *Picea abies*; our model also has the ability to explain some experimental results about cyclic patterns in radial versus vertical velocity components, as given in [19]. The asymptotic analysis was verified through a second order numerical scheme to be valid in general (i.e., for large saturation variations), as long as we do not reach the low pressures at which embolisms start to form, at which point the model assumptions break. The asymptotic results for the steady state case were shown to conform with a resistance circuit model.

7.1 Future Work

First, some work remains to be done to specify the conditions under which we can get good recovery in the inverse problem optimization algorithm we proposed in Chapter 5 to obtain

the transpiration function from sap flux measurements in the tree trunk. Furthermore, the symmetry assumption for $E(t)$ should ideally be removed. Related to this problem is the interesting inverse problem of determining the spatial variation in the hydraulic conductivity, through stem sap flux and leaves transpiration flux measurements. Next, we only considered the trunk for our domain, and instead of the branches, we specified a flow boundary condition. The next step is to consider the branches as mini-trunks, and couple the flow inside the branches to the flow inside the trunk; this could be potentially useful especially in trees that have a lot of large branches emanating from the trunk. Furthermore, in our work, we neglected the angular component of the flow and assumed an axisymmetric flow; we also assumed the hydraulic conductivity eigenvectors to be aligned with the vertical and radial directions. This could be another possibility for future work, as in some trees, angular flow patterns were observed [10]; this in addition to the fact that the alignment of the tracheids changes near branching points in a tree.

As for embolism formation and recovery, we assumed that embolized tracheids are predetermined, and that there is no change in the embolism status of tracheids with time. Since embolism is an important factor in tree hydraulic functionality and tree death, including it in our model should be useful (see [1] and [2] for a model of unsaturated porous medium flow). Embolism formation at the cell level [11] and its effects on transport at the tree level [26], is an interesting multiphysics problem.

There are many other effects that we neglected in our model and could be important in determining the xylem flow. One is the effect of water withdrawal through the tree root system on the water distribution in the soil, which is important in water stress conditions [58]. Another is the effect of vertical and lateral growth of the stem through the apical and lateral meristems [60] on the domain size over time scales larger than the diurnal cycle. Yet another is the effect of the flow in the phloem, which transports sugars, on the flow in the xylem [16]. Furthermore, water loss from the leaves is intimately connected to photosynthesis through the stomata CO_2 gain, as we explained in the introduction, so one possible extension is to couple water transport to photosynthesis. Moreover, hormones and minerals are transported through the xylem, and these affect growth and photosynthesis.

Finally, now that we have a model for sap transport at the tree level, a next step that could be useful for environmental studies, is to average the interactions of a plot of trees or a forest on the surrounding environment, in terms of mass and energy exchanges [44].

Part II

Heat Transport

Chapter 8

Background: Heat Transport in Trees

Transport phenomena in general, and heat transport in particular, are well developed disciplines, with many applications in engineering [5], physical sciences, and biology [4]. The discipline is well-developed mathematically, with books that discuss generalized transport equations with multiple phases [59]. The different modes of heat transfer are also studied extensively: pure heat conduction in a material leads to the heat diffusion equation, with thermal conductivities, densities, and specific heat capacities that may be spatially and temporally dependent. In the case of the presence of more than one material with contrasting thermal parameters, the effective governing equations, boundary conditions and parameters can be derived using an averaging technique called homogenization [43]. Heat is also transferred in a moving fluid by convection (or advection), which is particularly important for engineering applications, as for example in the case of engine cooling systems. Radiative energy transfer is a well studied problem in physics and engineering [57] and is also important in environmental studies [45].

Heat transfer in trees is usually studied in the context of micrometeorology in order to estimate the energy storage change in a tree, and thus its effect on the energy storage in a canopy [27] and subsequent exchange with the atmosphere. Inside a tree we note that heat is transferred by two mechanisms: one is conduction, which is anisotropic due to anisotropy of the tree vascular tissue [49]; and the other is convection due to the movement of sap inside the tree. The thermal conductivity and heat capacity parameters also have spatial and temporal variations owing to the varying local composition of wood tissue, tree sap and air, and thus homogenization techniques are particularly helpful in obtaining properly averaged effective transport coefficients. Now considering the surface of the tree, there are multiple factors affecting the heat transfer: interfacial heat convection is one such factor, which could be either natural or forced, depending on the wind speed; another factor is

radiative heat transfer to and from the surface of the tree, which depends on the properties of the surface and the interception of radiation by leaves [45].

In the context of trees, the first question that should be tackled is what kind of geometry should we consider. Taking into account the detailed tree geometry and including trunk, branches and leaves would produce a mathematically intractable model and turn the problem into more of a computational exercise with no foreseeable gains. Thus one simplification we exploit here is to consider the tree trunk only as a right circular cylinder with a cross-section of constant radius. This will allow us to use many results from previous studies on this simpler geometry. With simple boundary conditions and assumptions about symmetry and constant material properties, the problem becomes more easily amenable to analytical techniques [9]. Taking into account spatial and temporal dependence in material properties, or the anisotropy of the diffusion, or the lack of symmetry of the problem due to directionally dependent boundary conditions (as for example with solar radiation), the problem is no longer separable and one must resort to other tools such as asymptotic analysis or numerical solution. In [51] for example, the tree is treated as a 2D disk with no vertical dependence on temperature; this study also takes into account the angular dependence of incident radiation but neglects the height dependence and only obtains a numerical solution. In the [27] study, the authors consider a temperature that has only radial dependence in each horizontal slice of the canopy (as in many micrometeorology papers, they usually divide the domain into horizontal slices and average) so that any directionality in wind speed and radiation is lost, but the paper manages to derive some analytical results. In both papers just mentioned, heat diffusion is the only mechanism of heat transfer. As for [3], the author gives a fully 3D model of the tree as a porous medium that includes trunk, branches and surroundings, but does not offer any analysis, and only offers a numerical tool to solve the problem.

Studying the temperature distribution inside a tree, the boundary conditions pose a fundamental problem: the many aspects contributing to the boundary conditions and the variability during the day and throughout the year makes it difficult to specify the boundaries in a mathematically simple yet physically useful way. The main contributing factors include direct solar radiation, diffuse radiation, free and forced convection, evapo-transpiration and root uptake of groundwater through the roots. In [51], the authors derive some formulas for the convective heat transfer coefficients (both free and forced) and take into account direct and diffuse solar radiation. The diffusivity inside the tree is assumed to be constant, and the effect of sap flow inside the tree is neglected. The authors of [27] attempt to model the energy changes in a tree canopy and give a more comprehensive picture of the boundary conditions, taking into account a detailed model of radiation, transpiration and air moisture effects.

In our modeling of the heat transport inside a tree, we assume a cylindrical tree stem and ignore the branch and canopy structure, with diffusion and advection as the heat

transport mechanism. Both convective and radiative boundary conditions are considered with a constant interfacial heat convection coefficient. Later the model will be modified to include the effects of sap flow on the heat diffusivity. Note that some aspects of the following analysis bear resemblance to the results in [9].

Chapter 9

Governing Equations for Heat Transport

We start this chapter by a discussion of how the various environmental conditions determine the heat flux at the boundaries of the tree, and obtain a sense of the orders of magnitudes of these fluxes. We next derive the model equations, nondimensionalize and discuss the possible values of the dimensionless parameters as discussed in the literature.

9.1 Boundary Conditions

If we consider a tree as a cylinder then we need to specify three boundary conditions for temperature. The bottom at $z = 0$ will more or less have the soil temperature, which is a Dirichlet boundary condition. This is easily justified: if we assume that the soil is wet and the convective heat transfer coefficient is much larger for water than for air. Thus heat transfer to the soil occurs much faster than to surrounding air. So on the time scales of interest it is sufficient to assume the bottom temperature of the tree is the same as the soil temperature.

The more interesting boundary condition is at the outer (lateral) surface of the tree, where the heat flux [W/m^2] crossing the outer stem boundary can be divided into five physical types [27]:

- **Natural convection:** the tree surface heats or cools the air near the surface, thus causing a change in its density compared with the surrounding air, thus causing surface air to rise or sink and be replaced by the air further from the surface. The case of natural convection from the surface of a vertical cylinder at $r = r_0$ is discussed in [28], where the formula for heat flux due to natural convection is

$$J_n = h_n \left(u_a - u \right), \tag{9.1}$$

where h_n [W/m^2 K] is the natural convection coefficient that depends on the both the trunk surface temperature $u|_{r=r_0}$ and the surrounding air temperature u_a. For an isothermal vertical cylinder, [34] provides an empirical formula for the average $\bar{h}_n$ in both laminar (for $10 < \text{Gr Pr} < 10^8$) and turbulent ($10^9 < \text{Gr Pr}$) flow regimes for air

$$\bar{h}_n = \frac{k_a}{z_0} \begin{cases} 0.68 \frac{\text{Pr}^{\frac{1}{2}} \text{Gr}^{\frac{1}{4}}}{(0.952+\text{Pr})^{\frac{1}{4}}}, & \text{if} \qquad 10 < \text{Gr Pr} < 10^8, \\ 0.13 \, (\text{GrPr})^{\frac{1}{3}}, & \text{if} \qquad 10^9 < \text{Gr Pr}, \end{cases}$$

where Gr is the Grashof number, which represents the ratio of buoyant to viscous forces

$$\text{Gr} = \frac{g\beta}{\nu^2} \left| u - u_a \right| z_0^3,$$

Pr ≈ 0.71 is the Prandtl number, $k_a \approx 0.025$ [W/m K] is the thermal conductivity, $\beta = \frac{1}{u_a} \approx 3.66 \times 10^{-3}$ [1/K] is the volumetric expansion coefficient for an ideal gas, $\nu \approx 1.51 \times 10^{-5}$ [m^2/s] is the kinematic viscosity, and u_a [K] is the ambient temperature of the surrounding air [45]. These estimates are made assuming air temperature is approximately 293 [K]. Notice that u appears in the factor $|u_a - u|^{1/4}$ in the laminar regime and as $|u_a - u|^{1/3}$ in the turbulent regime (through the Grashof number), but we are already multiplying by $u_a - u$ in the natural convection flux term J_n [W/m^2]; thus the net effect is to increase the exponent of the temperature difference from 1 to 1.25 and 1.33 respectively, which may be potentially important as the temperature difference increases. We will nonetheless ignore this effect in the asymptotic analysis to obtain a linear boundary condition. To get a sense of the magnitude of $\bar{h}_n$, we calculate it using the above parameter values, assuming that $|u_a - u| = 1$ [K] to get Gr $= 47.3 \times 10^9$ so that $\bar{h}_n \approx 1.57$ [W/m^{2}K].

- **Forced convection due to wind:** the formula is of similar form to the natural convection case

$$J_f = h_f(\theta) \, (u_a - u) \, , \tag{9.2}$$

but with a different forced convection coefficient h_f is a function of wind speed and angular position along the trunk surface. According to [34, 42, 24], for the forward laminar portion of the cylinder

$$h_f(\theta) = 1.14 \left(\frac{k_a}{2r_0} \right) \left(\frac{2r_0 V_\infty}{\nu} \right)^{0.5} \text{Pr}^{0.4} \left[1 - \left(\frac{2\theta}{\pi} \right)^3 \right], \tag{9.3}$$

for $0 < \theta \lesssim \frac{\pi}{2}$ where θ is the polar angle around the trunk measured from the stagnation point and where V_∞ is the free stream air velocity. This empirical formula

is valid for only part of the cylinder (turbulence may arise on the rear side). Notice that there is both an angular dependence and a time dependence (through V_∞) in h_f; to simplify the analysis in the following chapters, we will assume that V_∞ is fixed and we will ignore any angular dependence. If we substitute the parameter values above into (9.3) with $\theta = 0$, we get the relation $h_f = 17.8V_\infty^{0.5}$. Now for velocities of 1, 10 and 100 [km/hour], the resulting h_f values are 9.38, 29.7 and 93.8 [W/m^2K] respectively.

- **Long wave radiation:** given by the Stefan-Boltzmann law [27, 45]

$$J_L = \epsilon_{tr}\sigma\left(\epsilon_a u_a^4 - \epsilon_{tr}u^4\right) + \epsilon_{tr}\sigma\left(\epsilon_{soil}u_{soil}^4 - \epsilon_{tr}u^4\right),$$

where $\sigma = 5.67 \times 10^{-8}$ W/m^{2}K^4 is Stefan-Boltzmann's constant, $\epsilon_a \approx 0.74$ is the apparent emissivity of a hemisphere of air radiating towards the trunk [45], $\epsilon_{tr} \approx 0.9$ is the emissivity of the trunk surface [57], and $\epsilon_{soil} \approx 0.38$ is the soil emissivity [57]. The value of ϵ_a corresponds to a clear sky and could vary otherwise, while ϵ_{soil} value is for a plowed soil and could also vary. Note that we can employ the following linear approximation $u^4 = (u_a + (u - u_a))^4 \approx u_a^4 + 4u_a^3(u - u_a)$, since the temperatures measured in Kelvin are close to each other, assuming the conditions are not too extreme, leading to

$$J_L = \epsilon_{tr}\sigma u_a^4(\epsilon_a - \epsilon_{tr}) + \epsilon_{tr}\sigma\left(\epsilon_{soil}u_{soil}^4 - \epsilon_{tr}u_a^4\right) - 4\sigma\epsilon_{tr}^2 u_a^3(u - u_a). \tag{9.4}$$

Substituting the above parameter values and assuming $u_a = u_{soil} = 293$ [K] we get $J_L = -256 - 5.13(u - u_a) \approx -256$ [W/m^2] for small temperature differences.

- **Short wave direct sun radiation:** as given by Beer's law [39, 36]

$$J_S = (1 - \alpha_{tr})\, S_t \tau_s^{\sec(Z)} \cos(i), \tag{9.5}$$

where $S_t = 1368$ W/m^2 is the total solar irradiance [51], $\tau_s \approx 0.76$ is the atmospheric transmissivity [51], Z is the solar zenith angle, and i is the solar incidence angle on the trunk surface. Here the surface properties of the tree play a role in how much radiation is absorbed through the reflectance value $\alpha_{tr} \approx 0.2$ [27]. In any case, this flux can not exceed the value of S_t.

- **Diffuse sun radiation:** for which one rough model is [51, 39, 38]

$$J_D = \frac{1}{3}S_t \cos(Z)\,(1 + \cos(Z))\left(\eta_s - \tau_s^{\sec(Z)}\right), \tag{9.6}$$

where $\eta_s \approx 0.8$ [51]. Note that S_t is the energy flux from the sun before entering the atmosphere, with part of this flux J_s reaching the earth surface directly, while the

other part gets scattered and forms the diffuse flux J_D. Of course part of S_t is lost back to outer space. Thus the sum $J_S + J_D$ is strictly less than S_t [45].

Now the tree leaves and branches have a shading effect, that causes a decay in the amount of radiation reaching the tree trunk surface; this can be modelled by Beer-Lambert law of decay; thus the amount of radiation reaching the tree trunk surface is an attenuated version of the incident radiation on the canopy before getting absorbed by the leaves and branches (see [27] for details). The attenuation factor is

$$e^{k_d \xi_s},$$

where k_d is the vegetative extinction factor, and ξ_s is the cumulative vegetation in the radiation path. Thus long wave (J_L), short wave J_S and diffuse (J_D) radiation fluxes must be multiplied by such a factor.

In any case, the sum of the above heat fluxes $J_n + J_f + J_L + J_s + J_D$ from (9.1)-(9.2) and (9.4)-(9.6) can be approximated by

$$J_{\text{total}} = h\left(u(1,\theta,z,t) - u_a(\theta,z,t)\right) + W(\theta,z,t),$$

where h depends on u_a, h_n, h_f and the decay attenuation factor, while W depends on u_a, u_{soil} and the direct solar radiation. Note that h has both a spatial (angular) and time dependence due to the spatial and time dependence of h_f and u_a. Thus the lateral boundary condition can be written as a Robin condition

$$k\frac{\partial u^*}{\partial r}\bigg|_{r=r_0} = -hu^* + W^*,$$

where $u^* = u - u_a$ is the temperature difference, and W^* is the resulting source at the boundary after this transformation. We drop the * for the rest of the heat transport part.

9.2 Model for Heat Advection-Diffusion in a Tree with Spatially Dependent Saturation

There are three main factors that affect heat transport in a tree: for one, spatially and temporally varying porosity and saturation values in the tree mean that the diffusivity is not constant because it depends on relative proportions of the various phases (solid wood, liquid sap and air); second, the heat diffusion may be anisotropic due to the vertical orientation of tracheids; third, there may be spatial and temporal variations in the boundary conditions.

The heat flux V_H [W/m^2] in the anisotropic case comes from a combination of diffusion and advection

$$V_H = -D(s)\nabla u + uv$$

Table 9.1: Variables and parameters used in the governing equations for the heat transport problem. Any parameters not listed here are instead in Table 2.1.

Symbol	Description	Units	Value	Ref.
C_0	Heat generation scaling=$\frac{W_0 r_0}{u_0(2k+hr_0)}$	–	0.509	(10.5)
D_g	thermal diffusivity of air	m^2/s	2.2×10^{-5}	[34]
D_l	thermal diffusivity of sap (water)	m^2/s	1.43×10^{-7}	[34]
$D_r(s)$	radial thermal diffusivity	m^2/s	–	(9.9)
D_{r0}	average diffusivity in the radial direction	m^2/s	1×10^{-7}	Fig.9.1
D_w	thermal diffusivity of spruce wood	m^2/s	1.24×10^{-7}	[34]
$D_z(s)$	vertical thermal diffusivity	m^2/s	–	(9.8)
D_{z0}	average diffusivity in the vertical direction	m^2/s	1.5×10^{-6}	Fig.9.1
$D_{\theta 0}$	average diffusivity in the angular direction	m^2/s	1×10^{-7}	Fig.9.1
h	natural convection heat transfer coefficient	W/m^2 K	10	
k	average radial thermal conductivity	W/m K	0.32	[27]
$N(r,\theta)$	soil temperature	K	–	
N_0	order of magnitude of soil temperature	K	–	
u	trunk temperature	K	–	
u_0	maximum trunk temperature=W_0/h	K	293	(9.19)
v_{r0}	magnitude of radial velocity= $\frac{K_0 \phi \zeta}{\mu}$	m/s	1.95×10^{-7}	(4.49)
v_{z0}	magnitude of vertical velocity= $\frac{K_0 \phi}{\mu}$	m/s	1.95×10^{-5}	(4.51)
$W(\theta,z)$	thermal heat flux from the lateral boundary	W/m^2	–	
W_0	maximum thermal heat flux	W/m^2	200	
ϕ_p	porosity of tree wood (max. saturation)	–	0.5735	
θ	cylindrical coordinate angle	radian	–	

where $D(s)$ is the saturation dependent diffusivity, $u(r,\theta,z,t)$ [K] is the temperature at location given by the cylindrical coordinates (r,θ,z) in the stem and at time t, and $v(r,\theta,z,t)$ is the sap velocity in the stem. The continuity equation gives

$$\frac{\partial u}{\partial t} = -\nabla \cdot V_H. \tag{9.7}$$

The thermal diffusivity matrix $\mathbb{D}$ in cylindrical coordinates is assumed to be anisotropic and diagonal:

$$\mathbb{D} = \begin{pmatrix} D_r & 0 & 0 \\ 0 & D_\theta & 0 \\ 0 & 0 & D_z \end{pmatrix}.$$

Here we assume that heat dissipation is negligible, which is achieved when we have local thermal equilibrium between the different phases [66], while the case of local non-equilibrium effects [61] is much more complicated and is not considered here. The diffusivities D_r and D_z are assumed to be appropriate phase averages of the diffusivities of wood D_w, sap D_s and air D_a, and vary as the saturation s varies in time at each point. The average to be used depends on the layering of the three phases: if the phases are to large extent layered parallel to the vertical direction, then the thermal diffusivities in the vertical direction should be

combined as a weighted arithmetic average

$$D_z = D_w\,(1-\phi_p) + D_a\,(\phi_p - s) + D_s(s), \tag{9.8}$$

so that the largest diffusivity (air in this case) dominates [43] as the heat is transported through the connected air pathway. In contrast, in the radial and angular directions, heat is transported across the layers so that the appropriate average is the harmonic average [43]

$$D_r = D_\theta = \left(\frac{1-\phi_p}{D_w} + \frac{\phi_p - s}{D_a} + \frac{s}{D_s}\right)^{-1}. \tag{9.9}$$

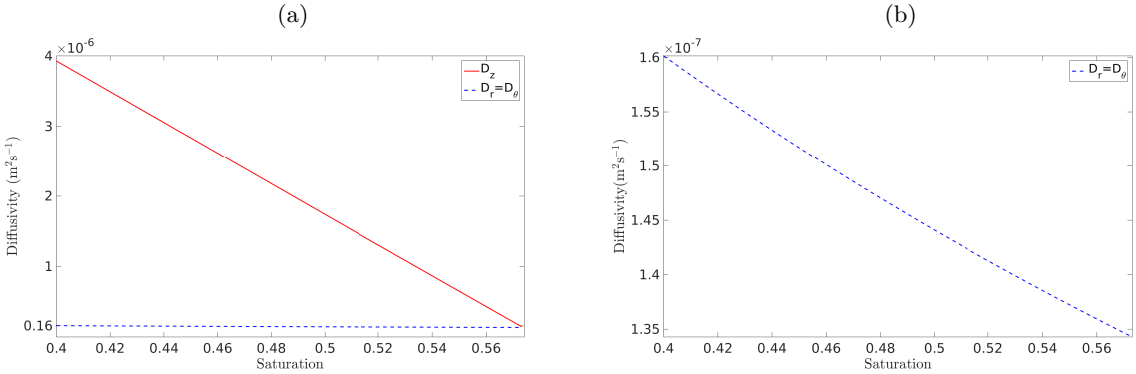

Figure 9.1: (a) Diffusivity saturation dependence for the radial/angular $D_r = D_\theta$ (blue) and vertical D_z (red) diffusion components, using formulas (9.9) and (9.8) and the values in Table 9.1. (b) Zoom in of the radial/angular diffusivity which varies over a much small range than the vertical diffusivity.

In this case, the smallest diffusivity (wood) dominates. Figure 9.1 shows a plot of D_r and D_z over a typical range of saturations, using (9.9) and (9.8). Notice that $D_r \sim 1\times10^{-7}$ [m^2/s] while D_z varies over an order of magnitude with an average $D_z \sim 1.5\times10^{-6}$ [m^2/s], so that $D_z/D_r \sim 10$. Although the layering of wood and water is obvious due to the vertical orientations of tracheids, it may be the case that the air does not form a continuous third layer spanning the entire stem, since embolized tracheids may not be connected vertically. Thus air, which has a much higher diffusivity than wood and sap, may not be able to facilitate heat diffusion in the vertical direction. This could explain the measurements made on wood for various saturation levels, that show that there is only a factor of 2 difference between the diffusivities in the transverse and vertical directions [40], so that anisotropy is not a major contributor. In any case, in the following analysis, we do not rely on any assumptions regarding anisotropy and so for the most part we assume the diffusivity is constant and scalar.

The boundary conditions are

$$k \left.\frac{\partial u}{\partial r}\right|_{r=1} = -h\, u|_{r=1} + W(\theta, z, t), \tag{9.10}$$

$$k \left.\frac{\partial u}{\partial z}\right|_{z=1} = -h\, u|_{z=1} + W(\theta, 1, t), \tag{9.11}$$

$$u|_{z=0} = N(r, \theta, t), \tag{9.12}$$

$$u|_{\theta=0} = u|_{\theta=2\pi}\,, \tag{9.13}$$

where k is the thermal conductivity, h is the convective heat transfer coefficient, W includes the heat flux due to radiation (and it also includes the air temperature variation), and N is the soil temperature (see Figure 9.2). Note here that the boundary conditions at $r = r_0$ will drop out from the outer solution in the case that advection effects dominate diffusion because sap entering from the roots at $z = 0$ exits from the leaves at this boundary. Note also that the boundary condition at $z = z_0$ diminishes in significance as we move away from the boundary due to the relatively small magnitude of vertical diffusion, as we will see in Section 9.3, and thus will be dropped out from our model when considering the asymptotic solutions.

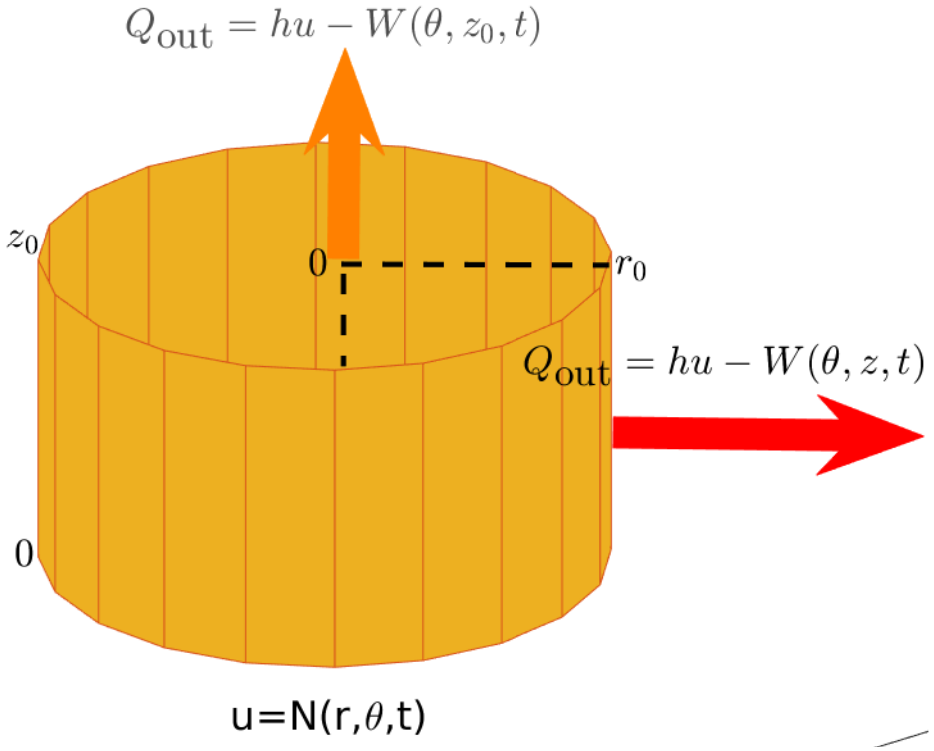

Figure 9.2: The boundary conditions for the heat transport problem: the Dirichlet boundary condition at the bottom, and the outgoing heat fluxes from the lateral side and the top of the tree. The upper boundary condition will be dropped out from our model when considering the asymptotic solutions.

9.3 Non-Dimensionalized Heat Transport Equations

Considering the advection-diffusion equation (9.7) in cylindrical coordinates, we get

$$\begin{aligned}\frac{\partial u}{\partial t} =& \nabla \cdot (D(s)\nabla u) - \nabla \cdot (u\vec{v}), \\ =& \frac{1}{r}\frac{\partial}{\partial r}\left(D_r r \frac{\partial u}{\partial r}\right) + \frac{1}{r^2}\frac{\partial}{\partial \theta}\left(D_\theta \frac{\partial u}{\partial \theta}\right) + \frac{\partial}{\partial z}\left(D_z \frac{\partial u}{\partial z}\right) - \frac{1}{r}\frac{\partial}{\partial r}(r v_r u) - \frac{\partial}{\partial z}(v_z u).\end{aligned}$$

In the following development, we will assume that the sap flow velocity follows the equations given in Part I of the thesis in Section 2.3 for the isotropic case $\kappa = 1$, and as will be shown below it suffices to consider the constant transpiration steady state case for the sap flow discussed in Section 4.5.

We use the following definitions for the dimensionless variables (starred variables)

$$\begin{aligned} r &= r_0 r^*, & z &= z_0 z^*, & u &= u_0 u^*, \\ N &= N_0 N^*, & v_r &= v_{r0} v_r^*, & v_z &= v_{z0} v_z^*, \\ D_r &= D_{r0} D_r^*, & D_\theta &= D_{\theta 0} D_\theta^*, & D_z &= D_{z0} D_z^*, \\ W &= W_0 W^*, & t &= \tau t^*, \end{aligned} \tag{9.14}$$

where r_0 and z_0 are the tree radius and height respectively, $\tau = 86400$ is the number of seconds per day, N_0 is the maximum temperature at the boundary $z = 0$ from (9.10), W_0 is the maximum of W at the boundary $r = 1$ from (9.10), u_0 is the order of magnitude of u defined in (9.19), D_{r0}, $D_{\theta 0}$ and D_{z0} are the average values of the diffusivities in the radial, angular and vertical directions respectively and v_{r0} and v_{z0} are the orders of magnitudes of the velocity components v_r and v_z respectively (which will be defined in the next chapter in (10.2)). Nondimensionalizing the advection-diffusion equation we get

$$\begin{aligned}\left(\frac{u_0}{\tau}\right)\frac{\partial u}{\partial t} = &\left(\frac{D_{r0}u_0}{r_0^2}\right)\frac{1}{r}\frac{\partial}{\partial r}\left(D_r r \frac{\partial u}{\partial r}\right) + \left(\frac{D_{\theta 0}u_0}{r_0^2}\right)\frac{1}{r^2}\frac{\partial}{\partial \theta}\left(D_\theta \frac{\partial u}{\partial \theta}\right) \\ &+ \left(\frac{D_{z0}u_0}{z_0^2}\right)\frac{\partial}{\partial z}\left(D_z \frac{\partial u}{\partial z}\right) - \left(\frac{v_{r0}u_0}{r_0}\right)\frac{1}{r}\frac{\partial}{\partial r}(r v_r u) - \left(\frac{v_{z0}u_0}{z_0}\right)\frac{\partial}{\partial z}(v_z u),\end{aligned}$$

where we have used the same letters for the non-dimensional variables, and the letters with 0 subscript denote scaling constants for the corresponding variables.

Now due to diffusion across layers of air, sap and wood, we expect similar diffusivities in the radial and angular directions. Rearranging under the assumption that $D_{r0} = D_{\theta 0}$, we get

$$M_0\frac{\partial u}{\partial t} = \frac{1}{r}\frac{\partial}{\partial r}\left(D_r r \frac{\partial u}{\partial r}\right) + \frac{1}{r^2}\frac{\partial}{\partial \theta}\left(D_\theta \frac{\partial u}{\partial \theta}\right) + M_1\frac{\partial}{\partial z}\left(D_z \frac{\partial u}{\partial z}\right) - M_2\frac{1}{r}\frac{\partial}{\partial r}(r v_r u) - M_3\frac{\partial}{\partial z}(v_z u), \tag{9.15}$$

where the dimensionless parameters are

$$M_0 = \left(\frac{r_0^2}{D_{r0}\tau}\right), \qquad M_1 = \left(\frac{D_{z0}}{D_{r0}}\zeta^2\right), \tag{9.16}$$
$$M_2 = \left(\frac{v_{r0}r_0}{D_{r0}}\right), \qquad M_3 = \left(\frac{v_{z0}r_0}{D_{r0}}\zeta\right),$$

Notice that the Péclet numbers $M_2 = M_3$ are equal because $\zeta = \frac{v_{r0}}{v_{z0}}$, as will be seen in Section 10.1.

It is worth mentioning some possible physical ranges of these parameters. First for the Norway spruce (Picea abies) using the parameter values in Table 2.1 with $v_{z0} \sim K_0\phi/2\mu \sim 10^{-5}$ [m/s] (see (4.51) and Figure 4.2 for $\gamma = 0$ case), we get the orders of magnitude $M_0 \sim 1$, $M_1 \sim 10^{-3}$ and $M_2 = M_3 \sim 10^{-1}$, so that the temporal, radial and angular diffusion terms dominate. Next, if we consider the data provided in [19], where the authors consider also spruce trees of radius $r_0 = 0.055$ [m] at breast height, height $z_0 = 10.5$ [m], and with $v_{z0} \approx 4 \times 10^{-4}$ [m/s], we obtain $M_0 \sim 1$, $M_1 \sim 10^{-4}$ and $M_3 \sim 1$, so that advection terms are now of the same order as the radial and angular diffusion terms. In both of the two cases just described, the vertical diffusion is negligible. So in the next chapter we will ignore the vertical diffusion contribution to heat transport, as incorporating it into our model does not alter our leading order solutions, but introduces the unnecessary complication of having to deal with the boundary layer at $z = 1$. We will also study two cases when advection is insignificant ($M_3 \ll 1$) and when it is important ($M_3 \sim 1$). The case of $M_3 \gg 1$ where advection dominates will also be considered briefly for completeness, despite the fact that we do not yet have experimental evidence to support its existence.

Next if we take a look at the above $M_0 \sim 1$ values, we notice that the temporal effects are present at leading order (considering a diurnal period) which means that both temperature and velocity variations in small radius stems ($r_0 \sim 1$) vary over the same time scale, where the time scale of the sap velocity variations is given by (4.4) as

$$\eta = \frac{s_0 z_0}{\tau K_0}\mu \sim 1,$$

where we redefine η by dividing by 2π so that the definitions of the dimensionless time t for both temperature and sap variation coincide. Note that the time variation in temperature scales quadratically with radius, while the sap velocity variation scales linearly with radius assuming fixed aspect ratio $\zeta = r_0/z_0$ (recall that μ defined in (4.4) does not scale with z_0 due to the restriction (4.27)). Thus for larger trees ($r_0 \sim 1$), assuming that the value of D_{r0} is more or less fixed (according to the discussion in Section 9.2), it should be the case that $M_0 \sim 10^2$ while $\eta \sim 10$ (assuming all other parameters are fixed). This means that the temperature variations will occur more much slowly than sap velocity variations, and thus only the average effect of velocity variations will matter. In this case the continuity

equation (2.6) reduces to

$$\nabla \cdot v \approx 0,$$

which simplifies the analysis in Section 10.2.1.

Next we nondimensionalize the boundary conditions (9.10) to get

$$\left.\frac{\partial u}{\partial r}\right|_{r=1} = -\left(\frac{hr_0}{k}\right) u|_{r=1} + \left(\frac{r_0 W_0}{k u_0}\right) W(\theta, z, t), \tag{9.17}$$

$$u|_{z=0} = \left(\frac{N_0}{u_0}\right) N(r, \theta). \tag{9.18}$$

where we have dropped out the boundary condition at $z = 1$ as it is insignificant due to the vertical diffusion being negligible ($M_1 \ll 1$). Note that we assume both of the flux terms on the right-hand side of the boundary condition at $r = 1$ affect the solution at leading order by requiring (see Tables 9.1 and 2.1)

$$u_0 = \frac{W_0}{h} \tag{9.19}$$

Chapter 10

Fourier-Bessel Series Solutions

In this chapter we set out to derive asymptotic and Fourier-Bessel series solutions to our model equations. We start by deriving leading order steady-state solutions for the time-constant boundary conditions for three asymptotic limits: advection and diffusion comparable ($M_2 \sim 1$), advection dominated ($M_2 \gg 1$) and diffusion dominated ($M_2 \ll 1$). Next we build on the steady state solutions to solve the equations when the boundary conditions are time-varying. Finally, we discuss the effect of a saturation dependent thermal diffusivity on the solutions.

10.1 Steady Heat Transport with Constant Transpiration

We first consider the constant-in-time boundary conditions case; as for the velocities of the advection terms, we assume the constant axisymmetric steady state transpiration case in Part I, with constant isotropic hydraulic conductivity K. Thus using the expressions for velocity and saturation from (4.48), (4.50) and (4.28), we get the dimensionless velocities (to first order)

$$v_z = \int_z^1 f(w)dw \qquad \text{and} \qquad v_r = \frac{1}{2} r f(z),$$

which may be written in the alternate form

$$v_z = g(z) \qquad \text{and} \qquad v_r = -\frac{1}{2} r g'(z), \tag{10.1}$$

where we have defined

$$g(z) = \int_z^1 f(w)dw.$$

The dimensional velocity magnitudes are given by (4.49) and (4.51) as

$$v_{r0} = \frac{K_0 \phi \zeta}{2\mu} \qquad \text{and} \qquad v_{z0} = \frac{K_0 \phi}{2\mu}, \tag{10.2}$$

so that $M_2 = M_3$. Note that the above velocity field is identically divergence free, so that the heat equation (9.15) simplifies to

$$0 = L(u), \tag{10.3}$$

where

$$L(u) \;=\; \frac{1}{r}\frac{\partial}{\partial r}\left(D_r r \frac{\partial u}{\partial r}\right) \;+\; \frac{1}{r^2}\frac{\partial}{\partial \theta}\left(D_\theta \frac{\partial u}{\partial \theta}\right) \;-\; M_2\left[-\left(\frac{r}{2}\right) g'(z)\frac{\partial u}{\partial r} + g(z)\frac{\partial u}{\partial z}\right]. \tag{10.4}$$

Now we transform the problem into one with homogeneous boundary conditions in r so that we can apply separation of variables, by defining a new temperature variable

$$U = u - C_0 r^2 W(\theta, z),$$

where

$$C_0 = \frac{W_0 r_0}{u_0\,(2k + h r_0)}. \tag{10.5}$$

This transforms equation (10.3) into

$$0 = L(U) + C_0 L(r^2 W), \tag{10.6}$$

and the boundary conditions into

$$\left(\frac{k}{r_0}\right)\left.\frac{\partial U}{\partial r}\right|_{r=1} = -h\; U|_{r=1}\,, \tag{10.7}$$

$$U|_{z=0} = \tilde{N}(r, \theta), \tag{10.8}$$

where

$$\tilde{N}(r, \theta) = \left(\frac{N_0}{u_0}\right) N(r, \theta) - C_0 r^2 W(\theta, 0). \tag{10.9}$$

In the following three sections, we assume that the diffusivities have no dependence on saturation or space, so that the dimensionless diffusivities are

$$D_r = D_\theta = D_z = 1$$

and we consider several cases:

- advection and diffusion are comparable ($M_2 \sim 1$),
- diffusion dominates ($M_2 \ll 1$),
- and advection dominates ($M_2 \gg 1$).

10.1.1 Advection and Diffusion Comparable in Magnitude

Here we consider the case where horizontal diffusion and vertical advection are comparable ($M_2 \sim 1$), which corresponds to relatively high transpiration rate, large radius and/or low stem aspect ratio. We will assume the following in the analysis below

$$\begin{aligned} g_0(z) &= O(1), \\ g(z) &= 1 + \chi g_0(z), \\ \chi &\sim M_1^{\frac{1}{2}} \ll 1, \\ \zeta &= 10^{-2}. \end{aligned}$$

We assume the velocity profiles correspond to the case of the sap flow problem we solved in Part I of the thesis, with transpiration occurring mainly from the uppermost lateral tree surface, with low transpiration rate from the rest of the lateral surface. This means that the flow is nearly constant and in the vertical direction, with a small perturbation of magnitude χ and form $g_0(z)$.

Proceeding with a regular asymptotic expansion in χ

$$U = U_0 + U_1\chi + ...,$$

we get the following leading order equation from (10.6):

$$0 = \frac{1}{r}\frac{\partial}{\partial r}\left(r\frac{\partial U}{\partial r}\right) + \frac{1}{r^2}\frac{\partial^2 U}{\partial \theta^2} - M_2\frac{\partial U}{\partial z} + M_2 G(r,\theta,z),$$

where

$$G(r,\theta,z) = \frac{C_0}{M_2}\left(4W + \frac{\partial^2 W}{\partial \theta^2} - M_2 r^2\frac{\partial W}{\partial z}\right).$$

Note that since we will be only considering the leading order solution in this chapter (see the appendix for the first correction to this solution) we will be using U instead of U_0 to simplify the notation. This equation can be written as

$$\frac{\partial U}{\partial z} = \frac{1}{M_2}\left[\frac{1}{r}\frac{\partial}{\partial r}\left(r\frac{\partial U}{\partial r}\right) + \frac{1}{r^2}\frac{\partial^2 U}{\partial \theta^2}\right] + G(r,\theta,z), \tag{10.10}$$

with boundary conditions at $z = 0$

$$U|_{z=0} = \tilde{N}(r,\theta), \tag{10.11}$$

and at $r = 1$

$$\left(\frac{k}{r_0}\right) \left.\frac{\partial U}{\partial r}\right|_{r=1} = -h\, U|_{r=1}\,. \tag{10.12}$$

In the following we will assume that the left hand side is of lower order of magnitude, which corresponds to the case of high convective flux due to windy conditions for example, and so

$$U|_{r=1} = 0. \tag{10.13}$$

Other cases can be treated similarly, and the only difference is in the equation that determines the eigenvalues γ_{nm} (see below).

Now the solution can be written as a sum of solutions $U = U^A + U^B$ to the following two subproblems

$$\frac{\partial U^A}{\partial z} = \frac{1}{M_2}\left[\frac{1}{r}\frac{\partial}{\partial r}\left(r\frac{\partial U^A}{\partial r}\right) + \frac{1}{r^2}\frac{\partial^2 U^A}{\partial \theta^2}\right], \tag{10.14}$$

$$U^A|_{r=1} = 0, \tag{10.15}$$

$$U^A|_{z=0} = \tilde{N}(r,\theta), \tag{10.16}$$

and

$$\frac{\partial U^B}{\partial z} = \frac{1}{M_2}\left[\frac{1}{r}\frac{\partial}{\partial r}\left(r\frac{\partial U^B}{\partial r}\right) + \frac{1}{r^2}\frac{\partial^2 U^B}{\partial \theta^2}\right] + G(r,\theta,z), \tag{10.17}$$

$$U^B|_{r=1} = 0, \tag{10.18}$$

$$U^B|_{z=0} = 0. \tag{10.19}$$

Using separation of variables, the first problem has solution

$$U^A(r,\theta,z) = \sum_{n,m=0}^{\infty} J_n(\gamma_{nm} r) e^{-\frac{\gamma_{nm}^2}{M_2} z} \left(A_{nm}\cos(n\theta) + B_{nm}\sin(n\theta)\right),$$

where J_n is the Bessel function of nth order, while A_{nm} and B_{nm} are determined by the boundary condition at $z = 0$

$$\tilde{N}(r,\theta) = \sum_{n,m=0}^{\infty} J_n(\gamma_{nm} r) \left(A_{nm}\cos(n\theta) + B_{nm}\sin(n\theta)\right), \tag{10.20}$$

(see later formulas (10.24)) and γ_{nm} for $m = 0, 1, ...$ are the roots of J_n (boundary condition at $r = 1$)

$$J_n(\gamma_{nm}) = 0,$$

where $n = 0, 1, \cdots$.

As for the second problem, we will temporarily assign $t^* = z$, so that

$$\begin{aligned}
\frac{\partial U^B}{\partial t^*} &= \frac{1}{M_2}\left[\frac{1}{r}\frac{\partial}{\partial r}\left(r\frac{\partial U^B}{\partial r}\right) + \frac{1}{r^2}\frac{\partial^2 U^B}{\partial \theta^2}\right] + G(r,\theta,t^*),\\
U^B|_{r=1} &= 0,\\
U^B|_{t^*=0} &= 0,
\end{aligned}$$

which is just the nonhomogeneous heat equation on a disk with Dirichlet BC and homogeneous initial condition.

Now consider the following problem for $t^* > s$

$$\begin{aligned}
\frac{\partial U^s}{\partial t^*} &= \frac{1}{M_2}\left[\frac{1}{r}\frac{\partial}{\partial r}\left(r\frac{\partial U^s}{\partial r}\right) + \frac{1}{r^2}\frac{\partial^2 U^s}{\partial \theta^2}\right],\\
U^s(1,\theta,t^*) &= 0,\\
U^s(r,\theta,s) &= G(r,\theta,s).
\end{aligned}$$

Then by Duhamel's principle

$$U^B(r,\theta,t^*) = \int_0^{t^*} U^s(r,\theta,t^*)ds,$$

and letting $t = t^* - s$ and $V^s(r,\theta,t) = U^s(r,\theta,t+s)$ yields for $t > 0$

$$\begin{aligned}
\frac{\partial V^s}{\partial t} &= \frac{1}{M_2}\left[\frac{1}{r}\frac{\partial}{\partial r}\left(r\frac{\partial V^s}{\partial r}\right) + \frac{1}{r^2}\frac{\partial^2 V^s}{\partial \theta^2}\right],\\
V^s(1,\theta,t) &= 0,\\
V^s(r,\theta,0) &= G(r,\theta,s).
\end{aligned}$$

Proceeding with separation of variables we get

$$V^s(r,\theta,t) = \sum_{n,m=0}^{\infty} J_n(\gamma_{nm}r)e^{-\frac{\gamma_{nm}^2}{M_2}t}\left(A_{nm}^s\cos(n\theta) + B_{nm}^s\sin(n\theta)\right),$$

where A_{nm}^s and B_{nm}^s are determined by the equations

$$G(r,\theta,s) = \sum_{n,m=0}^{\infty} J_n(\gamma_{nm}r)\left(A_{nm}^s\cos(n\theta) + B_{nm}^s\sin(n\theta)\right)$$

and again γ_{nm} are roots of

$$J_n(\gamma_{nm}) = 0.$$

Formulas for A^s_{nm} and B^s_{nm} can be found in (10.23). Thus for $t^* > s$

$$U^s(r,\theta,t^*) = \sum_{n,m=0}^{\infty} J_n(\gamma_{nm}r)e^{-\frac{\gamma_{nm}^2}{M_2}(t^*-s)}\left(A^s_{nm}\cos(n\theta) + B^s_{nm}\sin(n\theta)\right),$$

and

$$U^B(r,\theta,z) = \int_0^z \sum_{n,m=0}^{\infty} J_n(\gamma_{nm}r)e^{-\frac{\gamma_{nm}^2}{M_2}(z-s)}\left(A^s_{nm}\cos(n\theta) + B^s_{nm}\sin(n\theta)\right) ds.$$

Thus the leading order approximation of the original problem (10.10), (10.11) and (10.13) is

$$u(r,\theta,z) = C_0 r^2 W(\theta,z) + \sum_{n,m=0}^{\infty} J_n(\gamma_{nm}r)e^{-\frac{\gamma_{nm}^2}{M_2}z}\left(A_{nm}\cos(n\theta) + B_{nm}\sin(n\theta)\right) \tag{10.21}$$

$$+ \int_0^z \sum_{n,m=0}^{\infty} J_n(\gamma_{nm}r)e^{-\frac{\gamma_{nm}^2}{M_2}(z-s)}\left(A^s_{nm}\cos(n\theta) + B^s_{nm}\sin(n\theta)\right) ds. \tag{10.22}$$

Formulas for Series Coefficients

To obtain explicit formulas for the coefficients A_{nm}, B_{nm}, A^s_{nm}, B^s_{nm} above, we start by writing $G(r,\theta,z)$ in a simpler form

$$G(r,\theta,z) = W_1(\theta,z) + W_2(\theta,z)r^2,$$

where

$$W_1(\theta,z) = \frac{C_0}{M_2}\left(4W + \frac{\partial^2 W}{\partial\theta^2}\right),$$
$$W_2(\theta,z) = \frac{C_0}{M_2}\left(-M_2\frac{\partial W}{\partial z}\right).$$

Thus the Fourier-Bessel series coefficients of G are

$$\begin{aligned} A^s_{nm} &= \left(\frac{\int_0^1 rJ_n(\gamma_{nm}r)dr}{\int_0^1 rJ_n(\gamma_{nm}r)^2dr}\right)\left(\frac{\int_0^{2\pi}\cos(n\theta)W_1(\theta,s)d\theta}{\int_0^{2\pi}\cos^2(n\theta)d\theta}\right) \\ &\quad + \left(\frac{\int_0^1 r^3J_n(\gamma_{nm}r)dr}{\int_0^1 rJ_n(\gamma_{nm}r)^2dr}\right)\left(\frac{\int_0^{2\pi}\cos(n\theta)W_2(\theta,s)d\theta}{\int_0^{2\pi}\cos^2(n\theta)d\theta}\right), \\ B^s_{nm} &= \left(\frac{\int_0^1 rJ_n(\gamma_{nm}r)dr}{\int_0^1 rJ_n(\gamma_{nm}r)^2dr}\right)\left(\frac{\int_0^{2\pi}\sin(n\theta)W_1(\theta,s)d\theta}{\int_0^{2\pi}\sin^2(n\theta)d\theta}\right) \\ &\quad + \left(\frac{\int_0^1 r^3J_n(\gamma_{nm}r)dr}{\int_0^1 rJ_n(\gamma_{nm}r)^2dr}\right)\left(\frac{\int_0^{2\pi}\sin(n\theta)W_2(\theta,s)d\theta}{\int_0^{2\pi}\sin^2(n\theta)d\theta}\right), \end{aligned} \tag{10.23}$$

Now considering the definition of $\tilde{N}$ in (10.9), and assuming that N can be decomposed as

$$N(r,\theta) = N_1(r)N_2(\theta),$$

the expressions for the coefficients A_{nm} and B_{nm} in (10.20) simplify to

$$\begin{aligned} A_{nm} =& \frac{N_0}{u_0}\left(\frac{\int_0^1 rJ_n(\gamma_{nm}r)N_1(r)dr}{\int_0^1 rJ_n^2(\gamma_{nm}r)dr}\right)\left(\frac{\int_0^{2\pi}\cos(n\theta)N_2(\theta)d\theta}{\int_0^{2\pi}\cos^2(n\theta)d\theta}\right) \\ &- C_0\left(\frac{\int_0^1 r^3J_n(\gamma_{nm}r)dr}{\int_0^1 rJ_n^2(\gamma_{nm}r)dr}\right)\left(\frac{\int_0^{2\pi}\cos(n\theta)W(\theta,0)d\theta}{\int_0^{2\pi}\cos^2(n\theta)d\theta}\right), \\ B_{nm} =& \frac{N_0}{u_0}\left(\frac{\int_0^1 rJ_n(\gamma_{nm}r)N_1(r)dr}{\int_0^1 rJ_n^2(\gamma_{nm}r)dr}\right)\left(\frac{\int_0^{2\pi}\sin(n\theta)N_2(\theta)d\theta}{\int_0^{2\pi}\sin^2(n\theta)d\theta}\right) \\ &- C_0\left(\frac{\int_0^1 r^3J_n(\gamma_{nm}r)dr}{\int_0^1 rJ_n^2(\gamma_{nm}r)dr}\right)\left(\frac{\int_0^{2\pi}\sin(n\theta)W(\theta,0)d\theta}{\int_0^{2\pi}\sin^2(n\theta)d\theta}\right). \end{aligned} \tag{10.24}$$

Figure 10.1 shows the effect of the lateral flux $W(z) = 1/2\,(1+\cos(\pi(z-1)))$ on the temperature distribution inside the stem, where the bottom boundary condition effect is insignificant. As the ratio r_0h/k in (9.17) increases above 1, the maximum temperature increases towards the ratio $u_0 = W_0/h$ from (9.19).

Figure 10.2 shows the effect of the temperature at the roots (the Dirichlet boundary condition at $z = 0$ in (9.17)) on the stem temperature at steady state, where we set $W = 0$ to eliminate the effect of the lateral flux. Notice that the ratio r_0h/k determines the smallest root γ_0 of (10.12) when $U = J_0(\gamma r)$. The temperature at $z = 0$ decays to 37% of its value at $z \approx z_0/\gamma_0^2$.

Figure 10.3 shows the temperature distribution along horizontal and vertical slices of the stem for the general case of a flux with angular variation $W(\theta,z) = 1/2\,(1-\cos(\pi z))\cos(\theta)$, which simulates the case of a tree which is exposed to the sun from one side (mainly at the top since the lower stem is shaded by leaves) yet effected by wind cooling currents from the other side (assuming the ambient temperature is below zero). In all the above cases, we

assumed a ratio $u_0 = W_0/h = 20$, so that the temperature inside the stem does not exceed 20 C.

(a) $W_0 = 100$ (b) $W_0 = 200$ (c) $W_0 = 400$

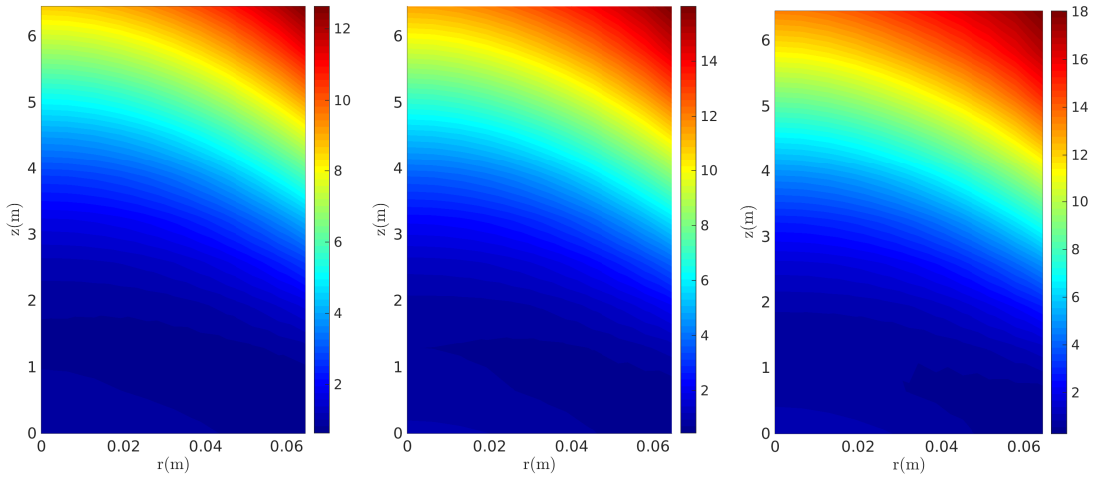

Figure 10.1: Steady state temperature distribution for the advection-diffusion case, for an axisymmetric lateral heat flux $W(z) = 1/2\,(1 + \cos(\pi(z-1)))$ and a Dirichlet bottom boundary temperature $N = J_0(\gamma_0)$. Here $W_0 = 100, 200, 400$ (left to right), $N_0 = 1$, $h = 5, 10, 20$, $k = 0.32$, $r_0 = 0.129/2$, $z_0 = 6.7$, $M_2 = 1$. Here the lowest eigenvalue $\gamma_0 = 1.26, 1.60, 1.91$. $r_0 h/k = 1.01, 2.02, 4.03$. This simulates the sun affecting the upper part of the tree.

10.1.2 Advection Dominated Heat Transport

Here we consider the case of $M_2 \gg 1$, which means that advection is more important than diffusion at leading order. The influx is from the bottom of the trunk at $z = 0$, and the outflux is from the branches at $r = 1$ and $z = 1$. In this case, the leading order equation (9.15) and boundary condition (9.17) (only the influx at $z = 0$) are

$$0 = -\left(\frac{r}{2}\right) g'(z)\frac{\partial u}{\partial r} + g(z)\frac{\partial u}{\partial z},$$
$$u|_{z=0} = \left(\frac{N_0}{u_0}\right) N(r,\theta).$$

Note here that we are not considering the boundary condition at $r = 1$, since we assume this to be an outflux boundary. Thus we are only considering the outer solution. We will briefly describe at the end of this section how to obtain the inner solution and the uniformly valid solution but will not go into details, as we did not verify our results numerically.

Since diffusion is not present in the leading order equation, sap moving from the roots at $z = 0$ to the branches at $r = 1$ and $z = 1$ maintains its temperature unchanged throughout

(a) $h = 5$ (b) $h = 10$ (c) $h = 20$

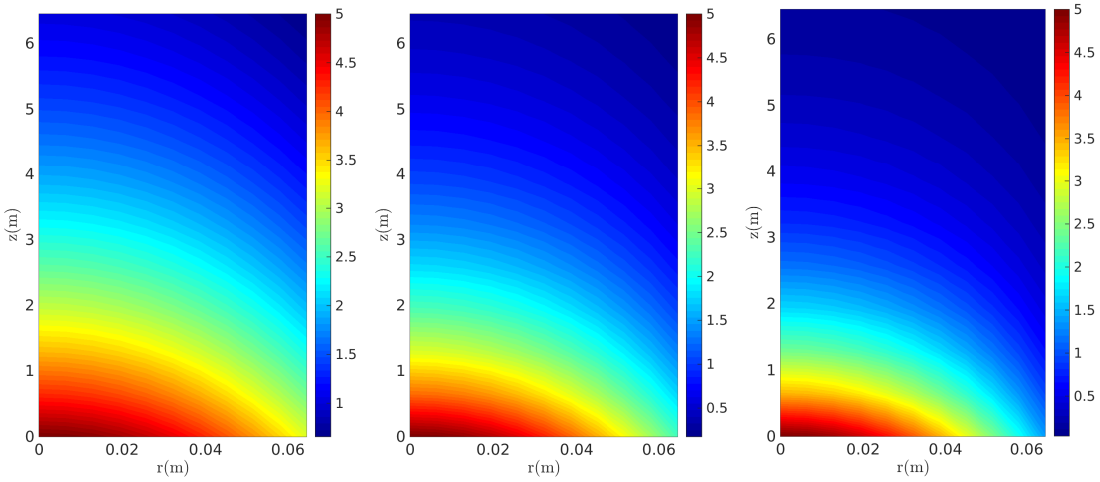

Figure 10.2: Steady state temperature distribution for the advection-diffusion case, for an axisymmetric lateral heat flux $W(z) = 0$ and a Dirichlet bottom boundary temperature $N = J_0(\gamma_0)$. Here $W_0 = 0$ (left to right), $N_0 = 5$, $h = 5, 10, 20$, $k = 0.32$, $r_0 = 0.129/2$, $z_0 = 6.7$, $M_2 = 1$. Here the lowest eigenvalue $\gamma_0 = 1.26, 1.60, 1.91$. $r_0 h/k = 1.01, 2.02, 4.03$.

its journey. Next we employ the method of characteristics [20] to solve the resulting advection equation. Let s be the distance along the path $(r(s), \theta(s), z(s))$, where a sap parcel has travelled along its journey starting from the roots at $(r(0), \theta(0), 0)$ where we set $z(0) = 0$. Since sap flow follows the velocity field, we expect that

$$\begin{aligned} \dot{r}(s) &= -\frac{1}{2} r g'(z), \\ \dot{\theta}(s) &= 0, \\ \dot{z}(s) &= g(z), \end{aligned} \tag{10.25}$$

where the second equation is a consequence of axisymmetry.

Next we set the temperature of the parcel $f(s)$ at distance s along the path to

$$f(s) = u(r(s), \theta(s), z(s)),$$

and since this is constant along the path, it should be the same as the temperature at the roots at $s = 0$

$$f(s) = f(0) = u(r(0), \theta(0), 0) = \left(\frac{N_0}{u_0}\right) N(r(0), \theta).$$

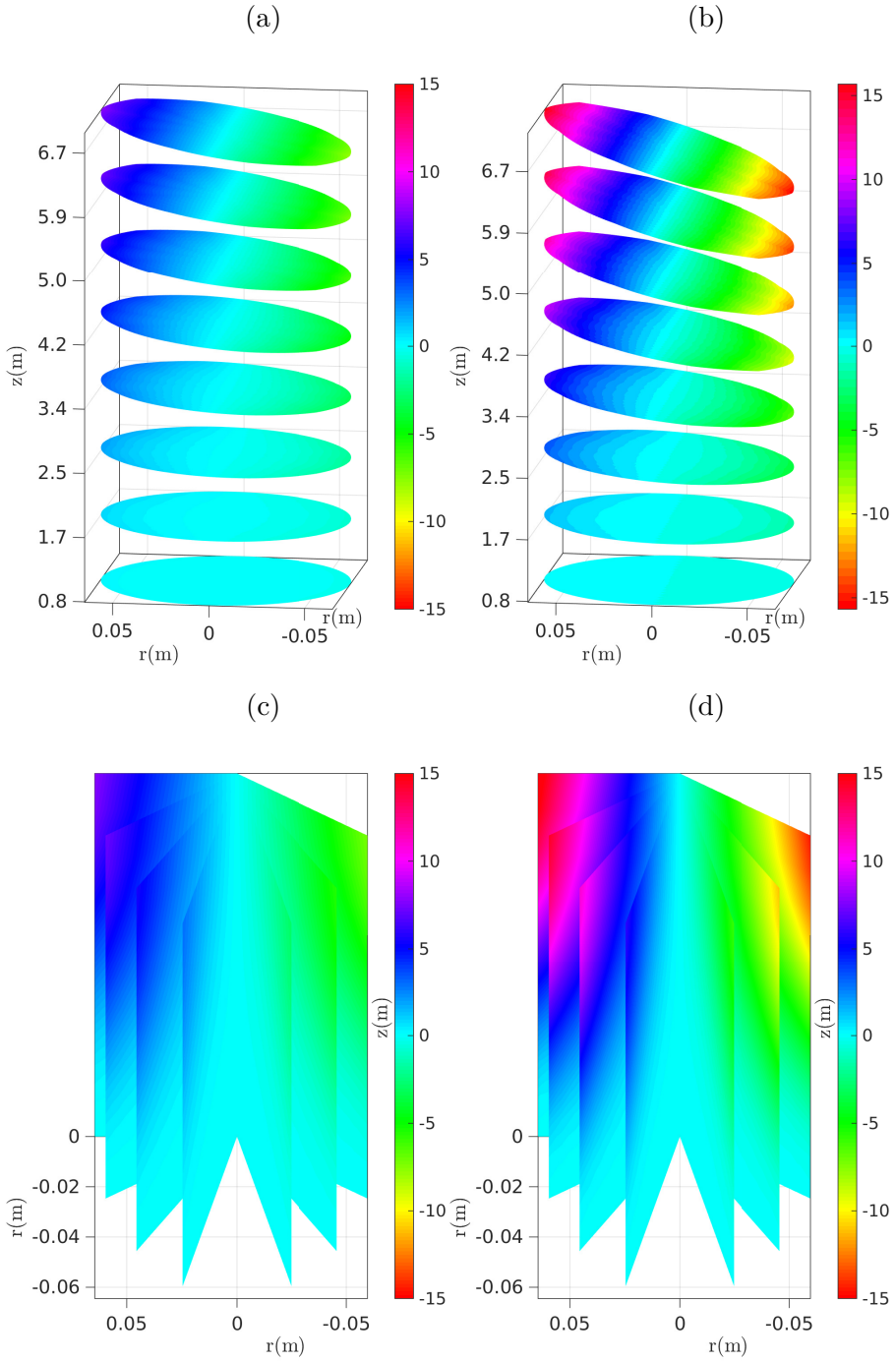

Figure 10.3: Steady state temperature distribution for the advection-diffusion case, for the lateral heat flux $W(\theta, z) = 1/2\,(1 - \cos(\pi z))\cos(\theta)$ and a Dirichlet bottom boundary temperature $N = r^2 W(\theta, 0)$. Here $W_0 = 100, 400$ (left to right), $N_0 = C_0 u_0$ (so that $\tilde{N} = 0$), $h = 5$, $k = 0.32$, $r_0 = 0.129/2$, $z_0 = 6.7$, $M_2 = 1$. Here the lowest eigenvalue $\gamma_0 = 1.26, 1.91$. $r_0 h/k = 1.01, 4.03$. (top) Horizontal cross-sections at $z = jz_0/8$ for $j = 1, ..., 8$. (bottom) vertical cross-sections at $\theta = j\pi/8$ for $j = 0, 1, ..., 7$.

Now using (10.25) we obtain

$$\dot{f}(s) = -\left(\frac{r}{2}\right) g'(z)\frac{\partial u}{\partial r} + g(z)\frac{\partial u}{\partial z} = 0.$$

The resulting differential equation governing the characteristic curve $r(z)$ is then

$$\frac{dr}{dz} = -\frac{rg'(z)}{2g(z)},$$

with θ constant. Solving gives the characteristic equation

$$r(s)^2 g(z(s)) = r^2(0)g(0),$$

which describes the relationship between the coordinates r and z along the path that starts at $(r(0), \theta(0), 0)$ and follows the velocity field. Thus

$$f(s) = u\left(r(s), \theta(s), z(s)\right) = \left(\frac{N_0}{u_0}\right) N\left(\sqrt{\frac{g(z(s))}{g(0)}} r(s), \theta\right),$$

or after eliminating s we get the outer solution

$$u_{\text{outer}}(r, \theta, z) = \left(\frac{N_0}{u_0}\right) N\left(\sqrt{\frac{g(z)}{g(0)}} r, \theta\right). \tag{10.26}$$

Thus if $g(z)$ is a decreasing function, then $g'(z) < 0$, which means according to (10.1) that the radial velocity component $v_r > 0$; consequently, the radius $r(s)$ increases along characteristics as the height $z(s)$ increases, as is clearly indicated by the factor $\sqrt{g(z)/g(0)}$ in formula (10.26). Notice that if v_z in (10.1) is constant in z and $v_r = 0$ (i.e. $g(z) = g(0) = 1$), we get

$$u_{\text{outer}}(r, \theta, z) = \left(\frac{N_0}{u_0}\right) N\left(r, \theta\right),$$

which is the expected vertical translation of the lower boundary temperature through the trunk when the lateral side at $r = 1$ is insulated.

Until now we were considering the outer asymptotic solution for our problem, which only satisfies the boundary condition at $z = 0$. Next we provide a brief description of how to obtain the inner solution at $r = 1$, where we expect the heat flux from the surroundings to diffuse to some depth from the lateral boundary. Since $M_2^{-1} \ll 1$, we can use it to expand the region around the singularity at $r = 1$ through the transformation

$$r = 1 - \epsilon r^* \tag{10.27}$$

The resulting leading order equation will include the effect of radial diffusion, which when solved gives the inner solution. Next we match the inner and outer solutions by taking limits as they approach each other, and the resulting uniform solution shows an effective lateral penetration depth of M_2^{-1}. The details have not been worked out yet, but would form an interesting area for future research.

10.1.3 Diffusion Dominated Heat Transport

Here we consider the case of $M_2 \ll 1$, where the velocities are small enough so that diffusion dominates over advection in (9.15). The resulting leading order equation is

$$0 = \frac{1}{r}\frac{\partial}{\partial r}\left(r\frac{\partial U}{\partial r}\right) + \frac{1}{r^2}\frac{\partial^2 U}{\partial \theta^2} + G(r,\theta,z),$$

where

$$G(r,\theta,z) = C_0\left(4W + \frac{\partial^2 W}{\partial \theta^2}\right),$$

and boundary condition at $r = 1$

$$\left(\frac{k}{r_0}\right)\left.\frac{\partial U}{\partial r}\right|_{r=1} = -h\left.U\right|_{r=1}.$$

In the following we will assume that the left hand side is of lower order of magnitude than the right hand side ($hr_0/k \gg 1$), and so

$$\left.U\right|_{r=1} = 0.$$

Other cases can be treated similarly, and the only difference is in the equation that determines the eigenvalues γ_{nm}.

Note that the resulting problem is nothing but the steady state heat diffusion problem on a disk with Dirichlet BC. Here the temperature of each horizontal disk section of the tree evolves independently from the rest of the tree. The solution of this problem is presented at the end of Section 10.2.2 as the limit as $t \to \infty$ of the time dependent case solution. Note also that the boundary at $z = 0$ is dropped out since we are considering the outer solution away from this boundary.

10.1.4 Comparing the Three Cases

In this section, we have discussed the steady state leading order solution of the heat transport problem in a tree. We discovered that the order of magnitude of M_2 determines the importance of advection relative to horizontal diffusion of heat, with $M_2 \sim 1$ giving the more interesting case where both diffusion and advection are equally significant. The so-

lution of this case given by (10.21) shows the effects of the bottom (first summation) and lateral (second summation) boundaries on the stem temperature. The effect of the bottom boundary on the temperature of the stem decays exponentially with height, with a time constant $\approx M_2/\gamma_0^2$ (assuming axisymmetry). As we saw in Figure 10.2, this effect could be quite substantial. Since the soil temperature can be different than the ambient temperature, this can potentially help the tree to mitigate extremes of the air temperature. Compare this with the pure horizontal diffusion case of $M_2 \ll 1$, with the solution given by (10.33),where the effects of the bottom boundary are constrained to a small boundary layer at the bottom, with the lateral flux dominating. Similarly, the effect of the lateral flux in the $M_2 \sim 1$ case (second summation in (10.21)) on the temperature at a certain height in the stem is not constrained to the flux at that particular height. Instead, the temperature at height z is affected by the lateral flux at all lower sections of the tree due to the vertical advection effect. This may act to reduce the more extreme weather effects at the tree top. Compare this with the case of pure diffusion $M_2 \ll 1$, where only the lateral heat flux affects only the horizontal section at that height. Now these two cases are the most probable cases. As for the pure advection case $M_2 \gg 1$, with the solution given by (10.26), if it exists in the context of trees, then it isolates the tree completely from lateral flux effects, and the temperature inside the stem will then be solely dependent on the soil temperature.

10.2 Time Varying Cases Asymptotic Analysis

10.2.1 Advection-Diffusion with Time-Dependent Boundary Conditions

This section is similar to Section 10.1.1, but with a slight modification to incorporate the time variation of the boundary conditions. This means that $W = W(\theta, z, t)$ and $N = N(r, \theta, t)$ in (9.17). Here we will assume that the velocity field is at steady state as given by (10.1), which is a good approximation for large trees ($r_0 \sim 1$) on the time scale of heat diffusion as explained at the end of Section 9.3. Now if we set

$$\tilde{L}(u) = L(u) - M_0 \frac{\partial u}{\partial t},$$

where $L(u)$ is defined by (10.4), then the time varying version of equation (10.6) has the same form:

$$0 = \tilde{L}(U) + C_0 \tilde{L}(r^2 W), \tag{10.28}$$

with $U = u - C_0 r^2 W(\theta, z, t)$. The boundary conditions are also modified by redefining $\tilde{N}(r, \theta, t) = (N_0/u_0)\, N(r, \theta, t) - C_0 r^2 W(\theta, 0, t)$ at $z = 0$. The initial condition $u(r, \theta, z, 0) = u_I(r, \theta, z)$ becomes after the transformation $U(r, \theta, z, 0) = U_I(r, \theta, z) = u_I - C_0 r^2 W(\theta, z, 0)$.

We will assume that $U_I = 0$ to simplify the formulas in the following analysis (so we are ignoring the initial transient behaviour).

The leading order equation we get from (10.28) is then

$$\left(\frac{M_0}{M_2}\right)\frac{\partial U}{\partial t} + \frac{\partial U}{\partial z} = \frac{1}{M_2}\left[\frac{1}{r}\frac{\partial}{\partial r}\left(r\frac{\partial U}{\partial r}\right) + \frac{1}{r^2}\frac{\partial^2 U}{\partial \theta^2}\right] + G(r,\theta,z,t), \tag{10.29}$$

where

$$G(r,\theta,z,t) = \frac{C_0}{M_2}\left(4W + \frac{\partial^2 W}{\partial \theta^2} - M_2 r^2\frac{\partial W}{\partial z} - M_0 r^2\frac{\partial W}{\partial t}\right).$$

Next we transform the leading order equation using

$$T = t - \frac{M_0}{M_2}z,$$

to get

$$\frac{\partial U}{\partial z} = \frac{1}{M_2}\left[\frac{1}{r}\frac{\partial}{\partial r}\left(r\frac{\partial U}{\partial r}\right) + \frac{1}{r^2}\frac{\partial^2 U}{\partial \theta^2}\right] + G\left(r,\theta,z,T + \frac{M_0}{M_2}z\right).$$

Similarly the boundary conditions (10.7) become

$$\left(\frac{k}{r_0}\right)\left.\frac{\partial U}{\partial r}\right|_{r=1} = -h\left.U\right|_{r=1}, \tag{10.30}$$

$$\left.U\right|_{z=0} = \tilde{N}(r,\theta,T). \tag{10.31}$$

Similar to the steady state case, we will only consider the following case for the boundary condition at $r = 1$, with other cases treated similarly

$$\left.U\right|_{r=1} = 0. \tag{10.32}$$

Notice that T can be treated as a parameter. This problem for each fixed T is now similar to the steady state problem we solved in Section 10.1.1, and the solution is also similar:

$$U(r,\theta,T,z) = \sum_{n,m=0}^{\infty} J_n(\gamma_{nm}r)e^{-\frac{\gamma_{nm}^2}{M_2}z}\left[A_{nm}(T)\cos(n\theta) + B_{nm}(T)\sin(n\theta)\right]$$
$$+\int_0^Z \sum_{n,m=0}^{\infty} J_n(\gamma_{nm}r)e^{-\frac{\gamma_{nm}^2}{M_2}(z-s)}\left[A_{nm}^s\left(T + \frac{M_0}{M_2}s\right)\cos(n\theta) + B_{nm}^s\left(T + \frac{M_0}{M_2}s\right)\sin(n\theta)\right]ds,$$

where A^s_{nm}, B^s_{nm} and γ_{nm} are determined by the equations

$$G(r,\theta,s,T) = \sum_{n,m=0}^{\infty} J_n(\gamma_{nm} r)\left(A^s_{nm}(T)\cos(n\theta) + B^s_{nm}(T)\sin(n\theta)\right),$$
$$J_n(\gamma_{nm}) = 0,$$

while A_{nm}, B_{nm} are determined by

$$\tilde{N}(r,\theta,T) = \sum_{n,m=0}^{\infty} J_n(\gamma_{nm} r)\left(A_{nm}(T)\cos(n\theta) + B_{nm}(T)\sin(n\theta)\right)$$

for $T > 0$. Thus

$$\begin{aligned} u(r,\theta,t,z) &= C_0 r^2 W(\theta,r,t) \\ &+ \sum_{n,m=0}^{\infty} J_n(\gamma_{nm} r) e^{-\frac{\gamma^2_{nm}}{M_2} z}\left[A_{nm}\left(t - \frac{M_0}{M_2} z\right)\cos(n\theta) + B_{nm}\left(t - \frac{M_0}{M_2} z\right)\sin(n\theta)\right] \\ &+ \int_0^z \sum_{n,m=0}^{\infty} J_n(\gamma_{nm} r) e^{-\frac{\gamma^2_{nm}}{M_2}(z-s)}\left[A^s_{nm}\left(t - \frac{M_0}{M_2}(z-s)\right)\cos(n\theta)\right. \\ &\qquad \left. + B^s_{nm}\left(t - \frac{M_0}{M_2}(z-s)\right)\sin(n\theta)\right] ds, \end{aligned}$$

where A_{nm}, B_{nm}, A^s_{nm} and B^s_{nm} are zero for negative arguments. The only difference from the steady state case solution (10.21) is the presence of the $M_0 z/M_2$ and $M_0(z-s)/M_2$ terms in the arguments of A_{nm}, B_{nm}, A^s_{nm} and B^s_{nm}. These terms take into account the time delay for temperature at one horizontal level to affect temperature at a higher position within the stem. Figure 10.4 shows the time variation ($\Delta t = 1/8$) in temperature for time periodic lateral flux $W(\theta,z) = 1/2\,(1-\cos(\pi z))\cos(\theta)\cos(2\pi t)$ for a horizontal cross section at $z = z_0/2$ and for a vertical cross section at $\theta = 0$. Notice the delay between the maximum values of W and temperature.

10.2.2 Diffusion-Dominated Heat Transport with Time-Dependent Boundary Condition

Here, we consider the case of $M_2 \ll 1$ but with $M_0 = 1$, so that the quasi-steady state assumption is no longer valid, and there is a significant relaxation time. In this case, equation (10.29) simplifies to

$$\frac{\partial U}{\partial t} = \frac{1}{r}\frac{\partial}{\partial r}\left(r\frac{\partial U}{\partial r}\right) + \frac{1}{r^2}\frac{\partial^2 U}{\partial \theta^2} + G(r,\theta,z,t).$$

(a) $z = z_0/2$ (b) $\theta = 0$

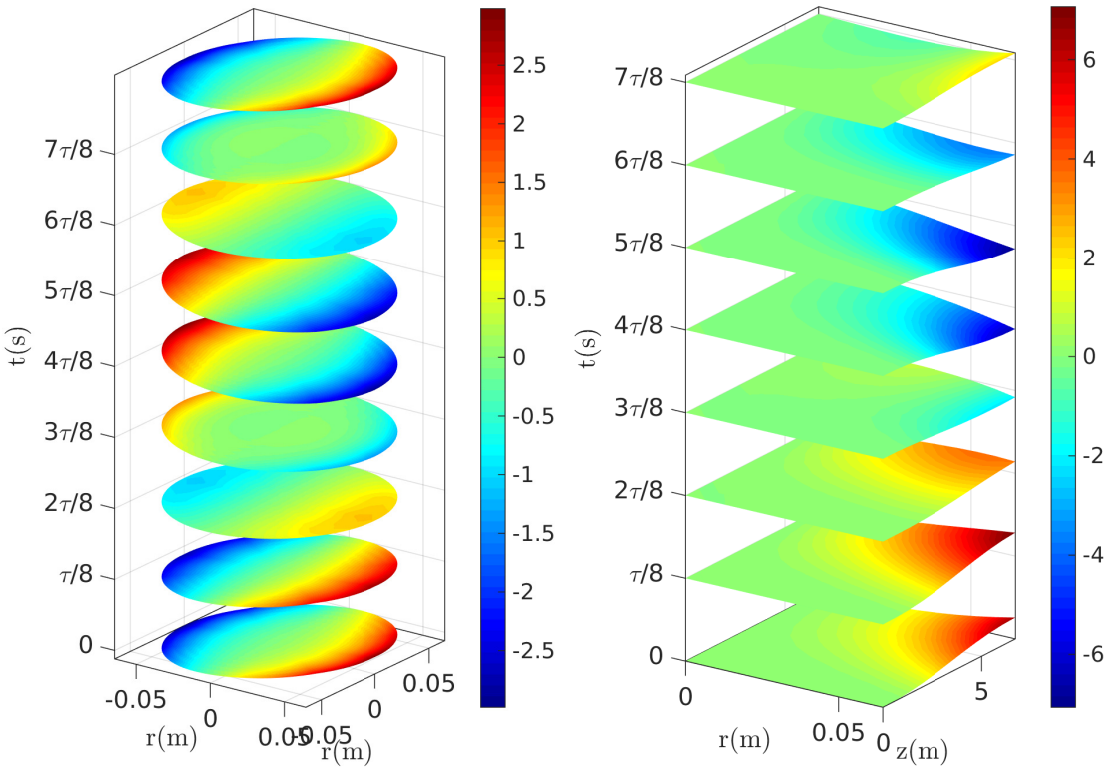

Figure 10.4: Steady state temperature distribution for the advection-diffusion case, for the lateral heat flux $W(\theta, z) = 1/2\,(1 - \cos(\pi z))\cos(\theta)\cos(2\pi t)$ and a Dirichlet bottom boundary temperature $N = r^2 W(\theta, 0)$. $W_0 = 100$, $N_0 = C_0 u_0$ (so that $\tilde{N} = 0$), $h = 5$, $k = 0.32$, $r_0 = 0.129/2$, $z_0 = 6.7$, $M_2 = 1$, $M_0 = 1$. The lowest eigenvalue $\gamma_0 = 1.26$. $r_0 h/k = 1.01$. (a) Horizontal cross-section at $z = z_0/2$. (b) Vertical cross-sections at $\theta = 0$. We assume that the initial transient behaviour has passed, and we are in a time periodic regime.

Assuming a similar choice for boundary condition (10.32) at $r = 1$, and with

$$U(r, \theta, z, 0) = U_I(r, \theta, z),$$

where U_I is the initial condition, then our problem at each fixed height z is similar to the problem (10.10), (10.11) and (10.13). This has the solution

$$\begin{aligned} U(r, \theta, t) = &\int_0^t \sum_{n,m=0}^{\infty} J_n(\gamma_{nm} r) e^{-\gamma_{nm}^2 (t-s)} \left(A_{nm}^z(s) \cos(n\theta) + B_{nm}^z(s) \sin(n\theta) \right) ds \\ &+ \sum_{n,m=0}^{\infty} J_n(\gamma_{nm} r) e^{-\gamma_{nm}^2 t} \left(C_{nm}^z \cos(n\theta) + D_{nm}^z \sin(n\theta) \right), \end{aligned}$$

where A_{nm}^z and B_{nm}^z are determined by the series expansion of G at each z

$$\begin{aligned} G(r, \theta, z, t) &= \sum_{n,m=0}^{\infty} J_n(\gamma_{nm} r) \left(A_{nm}^z(t) \cos(n\theta) + B_{nm}^z(t) \sin(n\theta) \right), \\ J_n(\gamma_{nm}) &= 0, \end{aligned}$$

while C_{nm}^z and D_{nm}^z are determined by the series expansion of U_I at each z

$$U_I(r, \theta, z) = \sum_{n,m=0}^{\infty} J_n(\gamma_{nm} r) \left(C_{nm}^z \cos(n\theta) + D_{nm}^z \sin(n\theta) \right).$$

In the case of time independence of G due to the time independence of the boundary condition at $r = 1$, the transient behaviour simplifies to

$$\begin{aligned} U(r, \theta, t) = &\sum_{n,m=0}^{\infty} J_n(\gamma_{nm} r) \left(\frac{1}{\gamma_{nm}^2} \left(1 - e^{-\gamma_{nm}^2 t} \right) \right) \left(A_{nm}^z \cos(n\theta) + B_{nm}^z \sin(n\theta) \right) \\ &+ \sum_{n,m=0}^{\infty} J_n(\gamma_{nm} r) e^{-\gamma_{nm}^2 t} \left(C_{nm}^z \cos(n\theta) + D_{nm}^z \sin(n\theta) \right), \end{aligned}$$

and as $t \to \infty$, this expression reaches the steady state limit

$$U(r, \theta, t) = \sum_{n,m=0}^{\infty} J_n(\gamma_{nm} r) \left(\frac{1}{\gamma_{nm}^2} \right) \left(A_{nm}^z \cos(n\theta) + B_{nm}^z \sin(n\theta) \right). \tag{10.33}$$

Thus at each height z the temperature is determined solely by the boundary condition at that height.

10.3 Saturation Dependent Thermal Diffusivities

Let's consider the case of $M_2 \ll 1$ where we also choose the time scale τ such that $M_0 = 1$. We assume that the sap saturation is constant in time, which is a good approximation in the case of large radius $r \sim 1$ (see Section 9.3). Now the saturation has only vertical dependence to first order if we consider the isotropic hydraulic conductivity case (see 4.2). Thus if we consider the saturation dependent thermal diffusivity (9.9), then the heat equation (10.28) give the leading order diffusion equation

$$\frac{\partial U}{\partial t} = D_r(s(z)) \left[\frac{1}{r} \frac{\partial}{\partial r} \left(r \frac{\partial U}{\partial r} \right) + \frac{1}{r^2} \frac{\partial^2 U}{\partial \theta^2} \right] + D_r(s(z)) G(\theta, z, t),$$

where

$$G(\theta, z, t) = C_0 \left(4W + \frac{\partial^2 W}{\partial \theta^2} \right),$$

Now z can be treated as a parameter in this equation, and thus if we define $t^* = D_r(s(z))t$, then the equation we get is similar to what we got in Section 10.2.2, and the solution is

$$\begin{aligned} U(r, \theta, z, t) = &\int_0^{t^*} \sum_{n,m=0}^{\infty} J_n(\gamma_{nm} r) e^{-\gamma_{nm}^2 (t^* - s)} \left(A_{nm}(z, s) \cos(n\theta) + B_{nm}(z, s) \sin(n\theta) \right) ds \\ &+ \sum_{n,m=0}^{\infty} J_n(\gamma_{nm} r) e^{-\gamma_{nm}^2 t^*} \left(C_{nm}^z \cos(n\theta) + D_{nm}^z \sin(n\theta) \right). \end{aligned}$$

Consequently, the thermal diffusivity variation acts to rescale the time variation at each height z; that is the larger $D(s(z))$ is, the smaller the relaxation time at height z.

Chapter 11

Numerical Simulations

11.1 Brief Algorithm Description

To avoid unnecessary repetition, the numerical discretization for the heat transport model is similar to the sap flow scheme, and so we will only provide a brief description of the method here. To simplify the code, we only considered the circular cylindrical axisymmetric case, where the boundary conditions have no angular dependence. For each cell, we calculate the physical variables at the edge (or face) as follows: temperature, saturation and sap flow velocities are taken at cell centers from the previous time step, so we calculate the diffusivities at cell centers then take an arithmetic average to get the diffusivities at cell edges. We also average the velocities at from cell centers to get values at cell edges. As for the heat flux, we use centered finite differences to calculate the temperature gradient, and then multiply by the edge diffusivity to calculate the diffusive heat flux along edges. The advection heat flux is just the product of the edge diffusivity and sap velocity. The Dirichlet boundary condition at $z = 0$ is dealt with in a manner similar to the sap flow problem, where we used fictitious cells at the boundary. The lateral boundary condition is a flux condition, so we just assign this flux to the edge. The upper boundary condition is similar. In the case of larger velocities in the vertical direction, we just extend the domain in the vertical direction and thus do not assign a boundary condition there.

11.2 Numerical Verification of Asymptotics

To verify the asymptotic solution for the advection-diffusion time-varying case in Section 10.2.1 we set $M_0 = 1$, $M_1 = 1 \times 10^{-4}$, $M_3 = 1$ and $hr_0/k = 2.9$, and take $W = 1/2\,(1 - \cos(2\pi z))\sin(2\pi t)$ and $N = 0$. We run the code on a 400×400 grid and compare the resulting solution to the leading order asymptotic solution. We consider two cases: one is $\chi = 0$ (i.e., constant vertical velocity v_z and zero radial velocity v_r) while in the other we have $\chi = M_1^{1/2}$ with $g(z) = -z + \sin(2\pi z)/(2\pi)$. In the first case, we expect a relative

error of order M_1 (or $O(10^{-4})$) and we get an error that ranges between 1×10^{-4} and 3.5×10^{-3} as shown in Figure 11.3. A detailed look at the error in Figure 11.2 reveals that the error originates from the lower left corner (see the numerical solution in Figure 11.1). In the second case, we expect an error of order $M_1^{1/2}$ (or $O(10^{-2})$), and this is what we get. Second, to check the pure diffusion case in Section 10.2.2, we make the change $M_3 = M_1^{1/2}$. The expected relative error is M_3 (or $O(10^{-2})$), which is what we get.

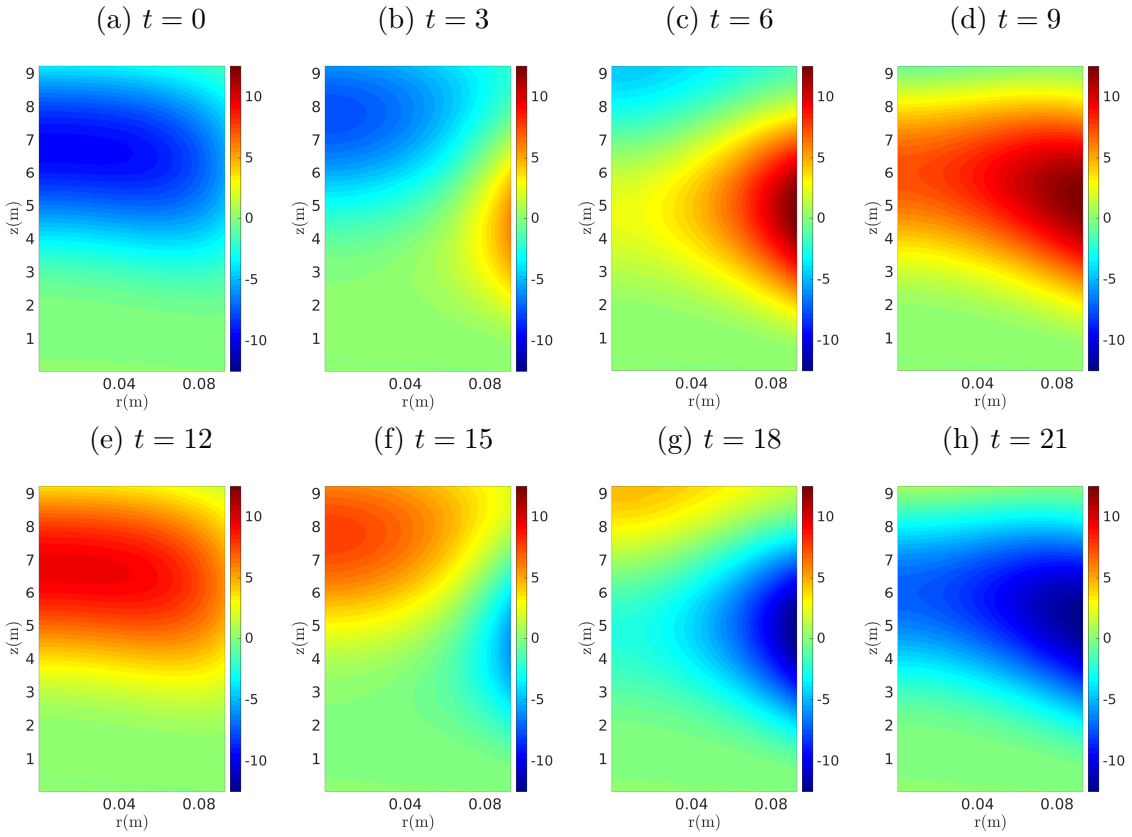

Figure 11.1: Numerical solution when $\chi = 0$ for the time varying $W = 1/2\,(1 - \cos(2\pi z))\sin(2\pi t)$ and $N = 0$.

11.3 Large Variation of Vertical Velocity

The numerical code allows us to further explore the case where $\chi \sim 1$. Other parameters are set as in the previous section for the advection-diffusion case with $M_3 = 1$. First notice the vertical velocity profile in Figure 11.4. With such a velocity variation we expect that any change in temperature due to heat flux from the lateral boundary will eventually be advected vertically to the region $z > 5$ were $v_z \sim 0$. This is indeed what we observe in the numerical simulations as shown in Figure 11.5. This could be potentially relevant to the case of a tree in winter (or summer), where the lower parts which are exposed to less severe

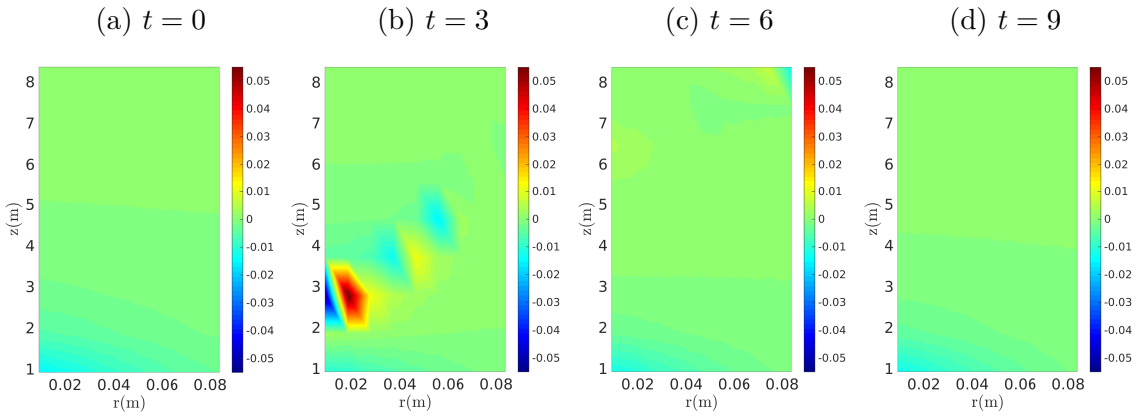

Figure 11.2: Difference between numerical and asymptotic solutions relative to the numerical solution when $\chi = 0$ for the time varying $W = 1/2\,(1 - \cos(2\pi z))\sin(2\pi t)$ and $N = 0$.

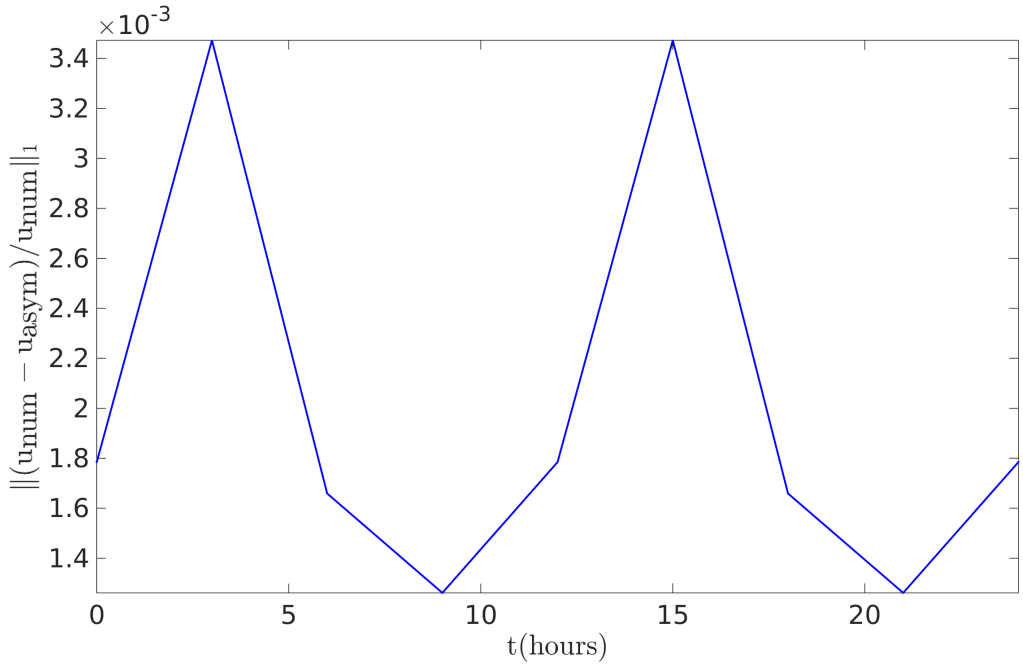

Figure 11.3: L1-norm of difference between numerical and asymptotic solutions relative to the numerical solution when $\chi = 0$ for the time varying $W = 1/2\,(1 - \cos(2\pi z))\sin(2\pi t)$ and $N = 0$.

weather conditions may be warmer (cooler), thus the warmth (coolness) is advected to the upper more exposed part of the tree and settles down.

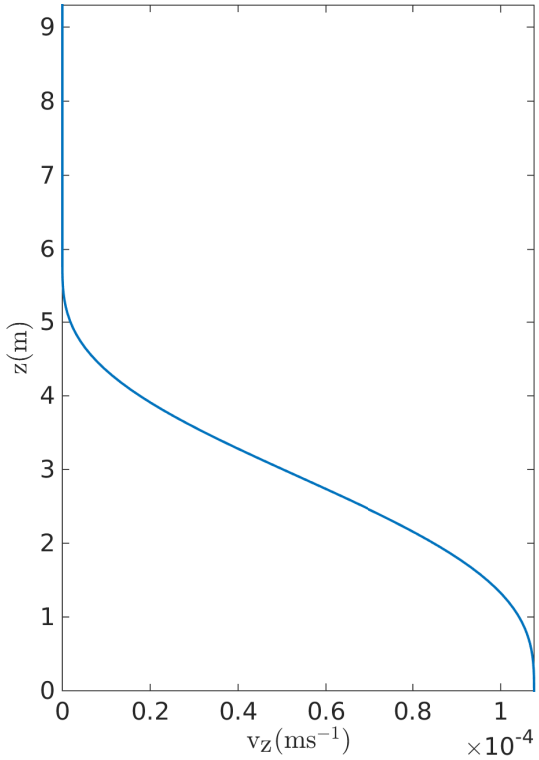

Figure 11.4: Vertical velocity component profile for $\chi = 1$ case. This represents the situation where there is a larger leaves concentration at the lower part of the tree.

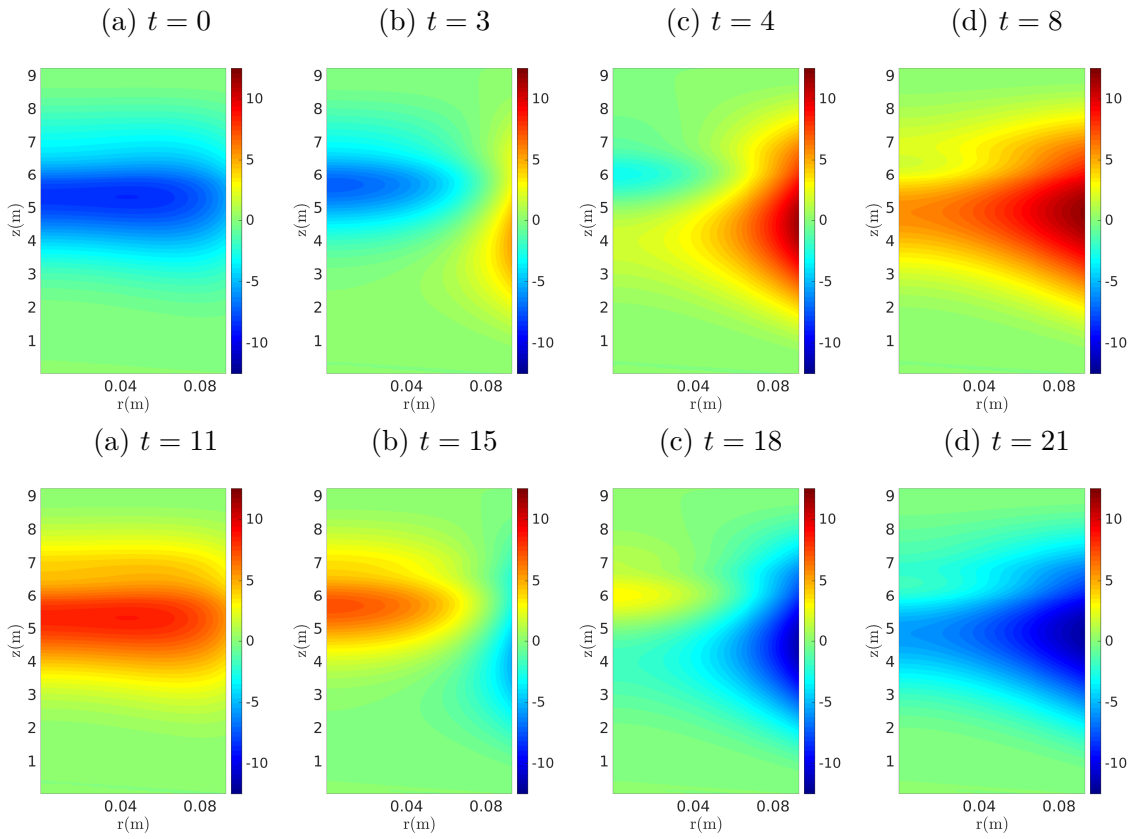

Figure 11.5: Effect of large variations in vertical velocity profile ($\chi = 1$) on temperature distribution time variation for the advection-diffusion case ($M_3 = 1$).

Chapter 12

Conclusion

We considered the heat transport problem in trees, with both diffusion and advection effects, and general boundary conditions. For the steady state time constant boundary conditions and constant flow case (which we argued is justifiable due to the difference in time scales between heat transport and sap flow), we derived series solutions assuming a mainly vertical constant sap flow with a constant perturbation, and assuming constant anisotropic diffusivities. In this case, we had three possibilities: diffusion dominated, diffusion-advection, and advection dominated heat transport. We also derived time varying solutions for the case of time varying heat transport boundary conditions. Next we considered the case of saturation dependent thermal diffusivities, where the saturation has only a vertical dependence. Finally, we verified our asymptotic solutions using a finite difference numerical code, and using this code we further explored the effect of varying vertical velocity profile on heat transport. In all of the above, we made only some minimal assumptions about the forms for the boundary conditions.

Bibliography

[1] C. A. Aumann and E. D. Ford. Modeling tree water flow as an unsaturated flow through a porous medium. *Journal of Theoretical Biology*, 219(4):415–429, 2002.

[2] C. A. Aumann and E. D. Ford. Parameterizing a model of Douglas fir water flow using a tracheid-level model. *Journal of Theoretical Biology*, 219(4):431–462, 2002.

[3] J. R. Ballard Jr. *A Three-dimensional Heat and Mass Transport Model for a Tree Within a Forest*. PhD thesis, Mississippi State University, 2011.

[4] S. M. Becker and A. V. Kuznetsov, editors. *Transport in Biological Media*. Elsevier, Boston, MA, 2013.

[5] R. B. Bird, W. E. Stewart, and E. N. Lightfoot. *Transport Phenomena*. John Wiley & Sons, New York, NY, 2007.

[6] G. Bohrer, H. Mourad, T. A. Laursen, D. Drewry, R. Avissar, D. Poggi, R. Oren, and G. G. Katul. Finite element tree crown hydrodynamics model (FETCH) using porous media flow within branching elements: A new representation of tree hydrodynamics. *Water Resources Research*, 41(11):W11404, 2005.

[7] C. Brodersen and A. McElrone. Maintenance of xylem network transport capacity: a review of embolism repair in vascular plants. *Frontiers in Plant Science*, 4:108, 2013.

[8] H. R. Brown. The theory of the rise of sap in trees: some historical and conceptual remarks. *Physics in Perspective*, 15(3):320–358, 2013.

[9] H. S. Carslaw and J. C. Jaeger. *Conduction of Heat in Solids*, volume 2. Clarendon Press Oxford, London, UK, 1959.

[10] J. Čermák, E. Cienciala, J. Kučera, and J.-E. Hällgren. Radial velocity profiles of water flow in trunks of Norway spruce and oak and the response of spruce to severing. *Tree Physiology*, 10(4):367–380, 1992.

[11] M. Ceseri and J. M. Stockie. A mathematical model of sap exudation in maple trees governed by ice melting, gas dissolution, and osmosis. *SIAM Journal on Applied Mathematics*, 73(2):649–676, 2013.

[12] Y.-L. Chuang, R. Oren, A. L. Bertozzi, N. Phillips, and G. G. Katul. The porous media model for the hydraulic system of a conifer tree: Linking sap flux data to transpiration rate. *Ecological Modelling*, 191(3):447–468, 2006.

[13] G. L. Comstock. Directional permeability of softwoods. *Wood and Fiber*, 1(4):283–289, 1970.

[14] G. L. Comstock. Directional permeability of softwoods. *Wood and Fiber Science*, 1(4):283–289, 2007.

[15] P. Cruiziat, H. Cochard, and T. Améglio. Hydraulic architecture of trees: main concepts and results. *Annals of Forest Science*, 59(7):723–752, 2002.

[16] F.-A. Daudet, A. Lacointe, J. Gaudillere, and P. Cruiziat. Generalized Münch coupling between sugar and water fluxes for modelling carbon allocation as affected by water status. *Journal of Theoretical Biology*, 214(3):481–498, 2002.

[17] J. Domec and B. Gartner. Age-and position-related changes in hydraulic versus mechanical dysfunction of xylem: inferring the design criteria for Douglas-fir wood structure. *Tree Physiology*, 22(2-3):91–104, 2002.

[18] J.-C. Domec and B. L. Gartner. Cavitation and water storage capacity in bole xylem segments of mature and young Douglas-fir trees. *Trees*, 15(4):204–214, 2001.

[19] J.-C. Domec, F. Meinzer, B. Gartner, and D. Woodruff. Transpiration-induced axial and radial tension gradients in trunks of Douglas-fir trees. *Tree Physiology*, 26(3):275–284, 2006.

[20] L. Evans. *Partial Differential Equations*. Graduate Studies in Mathematics. American Mathematical Society, Providence, RI, 1998.

[21] X. Frank, G. Almeida, and P. Perré. Multiphase flow in the vascular system of wood: From microscopic exploration to 3-D Lattice Boltzmann experiments. *International Journal of Multiphase Flow*, 36(8):599–607, 2010.

[22] T. Früh and W. Kurth. The hydraulic system of trees: theoretical framework and numerical simulation. *Journal of Theoretical Biology*, 201(4):251–270, 1999.

[23] B. L. Gartner. *Plant Stems: Physiology and Functional Morphology*. Academic Press, San Diego, CA, 1995.

[24] S. Goldstein. *Modern Developments in Fluid Dynamics: an Account of Theory and Experiment Relating to Boundary Layers, Turbulent Motion and Wakes*, volume 1. Clarendon Press, London, UK, 1938.

[25] P. J. Gould and C. A. Harrington. Extending sapwood-leaf area relationships from stems to roots in Coast Douglas-fir. *Annals of Forest Science*, 65(8):802–802, 2008.

[26] I. Graf, M. Ceseri, and J. M. Stockie. Multiscale model of a freeze–thaw process for tree sap exudation. *Journal of The Royal Society Interface*, 12(111):20150665, 2015.

[27] V. Haverd, M. Cuntz, R. Leuning, and H. Keith. Air and biomass heat storage fluxes in a forest canopy: calculation within a soil vegetation atmosphere transfer model. *Agricultural and Forest Meteorology*, 147(3):125–139, 2007.

[28] Y. Jaluria. *Natural Convection: Heat and Mass Transfer*, volume 5. Pergamon, 1980.

[29] S. A. James, F. C. Meinzer, G. Goldstein, D. Woodruff, T. Jones, T. Restom, M. Mejia, M. Clearwater, and P. Campanello. Axial and radial water transport and internal water storage in tropical forest canopy trees. *Oecologia*, 134(1):37–45, 2003.

[30] K. H. Jensen, K. Berg-Sørensen, H. Bruus, N. M. Holbrook, J. Liesche, A. Schulz, M. A. Zwieniecki, and T. Bohr. Sap flow and sugar transport in plants. *Reviews of Modern Physics*, 88(3):035007, 2016.

[31] R. J. Joly and J. B. Zaerr. Alteration of cell-wall water content and elasticity in Douglas-fir during periods of water deficit. *Plant Physiology*, 83(2):418–422, 1987.

[32] W. Kang and W. Y. Chung. Liquid water diffusivity of wood from the capillary pressure–moisture relation. *Journal of Wood Science*, 55:91–99, 2009.

[33] J. Kevorkian and J. D. Cole. *Perturbation Methods in Applied Mathematics*, volume 34. Springer-Verlag, New York, NY, 1981.

[34] F. Kreith, R. M. Manglik, and M. S. Bohn. *Principles of Heat Transfer*. Cengage Learning, Stamford, CT, 2012.

[35] R. Li and A. R. Weiskittel. Comparison of model forms for estimating stem taper and volume in the primary conifer species of the North American Acadian Region. *Annals of Forest Science*, 67:302, 2010.

[36] K.-N. Liou. *An Introduction to Atmospheric Radiation*, volume 84. Academic Press, San Diego, CA, 2002.

[37] D. Loustau, J.-C. Domec, and A. Bosc. Interpreting the variations in xylem sap flux density within the trunk of maritime pine (Pinus pinaster Ait.): application of a model for calculating water flows at tree and stand levels. 55(1-2):29–46, 1998.

[38] W. P. Lowry. Direct and diffuse solar radiation: variations with atmospheric turbidity and altitude. Technical report, Institute for Environmental Studies, University of Illinois, Urbana, IL, 1980.

[39] W. P. Lowry and P. P. Lowry. *Fundamentals of Biometeorology: Interactions of Organisms and the Atmosphere*. Peavine Publications, St. Louis, MO, 1989.

[40] T. Maku. Studies on the heat conduction in wood. *Bulletin of the Wood Research Institute*, 13:1–80, 1954.

[41] D. Marshall. Measurement of sap flow in conifers by heat transport. *Plant Physiology*, 33(6):385–396, 1958.

[42] R. Martinelli, A. Guibert, E. Morrin, and L. Boelter. An investigation of aircraft heaters VIII–a simplified method for the calculation of the unit thermal conductance over wings. Technical report, National Advisory Committee for Aeronautics, Washington, DC, 1943.

[43] C. C. Mei and B. Vernescu. *Homogenization Methods for Multiscale Mechanics*. World Scientific, Singapore, 2010.

[44] G. Mirfenderesgi, G. Bohrer, A. M. Matheny, S. Fatichi, M. Frasson, R. Prata, and K. V. Schäfer. Tree level hydrodynamic approach for resolving above ground water storage and stomatal conductance and modeling the effects of tree hydraulic strategy. *Journal of Geophysical Research: Biogeosciences*, 121(7):1792–1813, 2016.

[45] J. Monteith and M. Unsworth. *Principles of Environmental Physics: Plants, Animals, and the Atmosphere*. Academic Press, Oxford, UK, 2013.

[46] J. Morgan and M. G. Cannell. Shape of tree stems–A re-examination of the uniform stress hypothesis. *Tree Physiology*, 14(1):49–62, 1994.

[47] A. Nadler and M. T. Tyree. Substituting stem's water content by electrical conductivity for monitoring water status changes. *Soil Science Society of America Journal*, 72(4):1006–1013, 2008.

[48] K. J. Niklas. Size-dependent allometry of tree height, diameter and trunk-taper. *Annals of Botany*, 75:217–227, 1995.

[49] P. S. Nobel. *Physicochemical and Environmental Plant Physiology*. Academic Press, Oxford, UK, 1999.

[50] W. F. Pickard. The ascent of sap in plants. *Progress in Biophysics and Molecular Biology*, 37:181–229, 1981.

[51] B. E. Potter and J. A. Andresen. A finite-difference model of temperatures and heat flow within a tree stem. *Canadian Journal of Forest Research*, 32(3):548–555, 2002.

[52] R. Poyatos, J. Čermák, and P. Llorens. Variation in the radial patterns of sap flux density in pubescent oak (Quercus pubescens) and its implications for tree and stand transpiration measurements. *Tree Physiology*, 27(4):537–548, 2007.

[53] A. L. Redman, H. Bailleres, I. Turner, and P. Perré. Mass transfer properties (permeability and mass diffusivity) of four Australian hardwood species. *BioResources*, 7(3):3410–3424, 2012.

[54] F. E. Rockwell, J. K. Wheeler, and N. M. Holbrook. Cavitation and its discontents: opportunities for resolving current controversies. *Plant Physiology*, 164(4):1649–1660, 2014.

[55] P. J. Schulte and D. G. Costa. A mathematical description of water flow through plant tissues. *Journal of Theoretical Biology*, 180(1):61–70, 1996.

[56] E.-D. Schulze, A. Hall, O. Lange, and H. Walz. A portable steady-state porometer for measuring the carbon dioxide and water vapour exchanges of leaves under natural conditions. *Oecologia*, 53(2):141–145, 1982.

[57] R. Siegel and J. Howell. *Thermal Radiation Heat Transfer*. Hemisphere Publishing, Washington, DC, third edition, 1992.

[58] M. Siqueira, G. Katul, and A. Porporato. Onset of water stress, hysteresis in plant conductance, and hydraulic lift: scaling soil water dynamics from millimeters to meters. *Water Resources Research*, 44(1):W01432, 2008.

[59] J. C. Slattery, L. Sagis, and E.-S. Oh. *Interfacial Transport Phenomena*. Springer Science & Business Media, New York, NY, 2007.

[60] K. Steppe, D. J. De Pauw, R. Lemeur, and P. A. Vanrolleghem. A mathematical model linking tree sap flow dynamics to daily stem diameter fluctuations and radial stem growth. *Tree Physiology*, 26(3):257–273, 2006.

[61] B. Straughan. *Convection with Local Thermal Non-equilibrium and Microfluidic Effects*, volume 32. Springer International Publishing, Cham, Switzerland, 2015.

[62] A. Szymkiewicz. *Modelling Water Flow in Unsaturated Porous Media*. GeoPlanet: Earth and Planetary Sciences. Springer-Verlag, Berlin, Germany, 2013.

[63] L. Taiz and E. Zeiger. *Plant Physiology*. Sinaeur Associates Inc, Sunderland, MA, third edition, 2002.

[64] L. Testi and F. J. Villalobos. New approach for measuring low sap velocities in trees. *Agricultural and Forest Meteorology*, 149(3):730–734, 2009.

[65] M. T. Tyree and S. Yang. Water-storage capacity of Thuja, Tsuga and Acer stems measured by dehydration isotherms. *Planta*, 182(3):420–426, 1990.

[66] P. Vadasz et al. *Fluid Flow and Heat Transfer in Rotating Porous Media*. Springer, Cham, Switzerland, 2016.

[67] H. Van As. Intact plant MRI for the study of cell water relations, membrane permeability, cell-to-cell and long distance water transport. *Journal of Experimental Botany*, 58(4):743–756, 2007.

[68] M. W. Vandegehuchte and K. Steppe. Sapflow+: a four-needle heat-pulse sap flow sensor enabling nonempirical sap flux density and water content measurements. *New Phytologist*, 196(1):306–317, 2012.

[69] E. J. Ward, D. M. Bell, J. S. Clark, and R. Oren. Hydraulic time constants for transpiration of loblolly pine at a free-air carbon dioxide enrichment site. *Tree Physiology*, 33(2):123–134, 2013.

[70] Wikimedia Commons. File:xylem cells.svg — wikimedia commons, the free media repository, 2017. [Online; accessed 27-October-2017].

[71] Wikipedia. Kambium — wikipedia, encyclopedia, 2017. [Online; accessed 27-October-2017].

[72] M. H. Zimmermann. *Xylem Structure and the Ascent of Sap*. Springer-Verlag, New York, NY, 1983.

Appendix A

Correction Term for the Advection-Diffusion Case

Proceeding with the expansion in Section 10.1.1 and going on to the next order $O(\chi)$ equation we get

$$\begin{aligned}\frac{\partial U_1}{\partial z} &= \frac{1}{M_2}\left[\frac{1}{r}\frac{\partial}{\partial r}\left(r\frac{\partial U_1}{\partial r}\right) + \frac{1}{r^2}\frac{\partial^2 U_1}{\partial \theta^2}\right] + p(r,\theta,z)\\ U_1|_{r=1} &= 0\\ U_1|_{z=0} &= 0\end{aligned}$$

where

$$p(r,\theta,z) = \left(\frac{r}{2}\right) g_0'(z)\frac{\partial U_0}{\partial r} - g_0(z)\frac{\partial U_0}{\partial z} \tag{A.1}$$

This is similar to the subproblem (10.14) we solved above, with p replacing G as a source term. Thus the solution is

$$U_1(r,\theta,z) = \int_0^z \sum_{n,m=0}^{\infty} J_n(\gamma_{nm} r) e^{-\frac{\gamma_{nm}^2}{M_2}(z-s)} \left(C_{nm}^s \cos(n\theta) + D_{nm}^s \sin(n\theta)\right) ds \tag{A.2}$$

and C_{nm}^s and D_{nm}^s are the series coefficients for $p(r,\theta,s)$ in

$$p(r,\theta,s) = \sum_{n,m=0}^{\infty} J_n(\gamma_{nm} r)\left(C_{nm}^s \cos(n\theta) + D_{nm}^s \sin(n\theta)\right) \tag{A.3}$$

Now assuming there is no θ dependence in either of the boundary functions N and W (thus $\tilde{N}$ and G), so that $n = 0$ (thus will be dropped off as a subscript on J and γ), then the

expressions for A_{nm} in (10.24) and $A_{nm}(s)$ in (10.23) reduce to

$$A_m = \frac{\int_0^1 r\tilde{N}(r)J_0(\gamma_m r)dr}{\int_0^1 rJ_0^2(\gamma_m r)dr}$$
$$A_m^s = \frac{\int_0^1 rG(r,s)J_0(\gamma_m r)dr}{\int_0^1 rJ_0^2(\gamma_m r)dr}$$

which simplifies to

$$A_m = \frac{2}{J_0^2(\gamma_m) + J_1^2(\gamma_m)} \times \left[\frac{N_0}{u_0}\int_0^1 rN(r)J_0(\gamma_m r)dr - C_0W(0)\frac{((\gamma_m^2-4)J_1(\gamma_m)+2\gamma_m J_0(\gamma_m))}{\gamma_m^3}\right]$$

and

$$A_m^s = \frac{2}{J_0^2(\gamma_m) + J_1^2(\gamma_m)}\left(\frac{C_0}{M_2}\right) \times \left[\frac{4W(s)J_1(\gamma_m)}{\gamma_m} - M_2W'(s)\frac{((\gamma_m^2-4)J_1(\gamma_m)+2\gamma_m J_0(\gamma_m))}{\gamma_m^3}\right]$$

Now for the correction term U_1 equation (A.2), first we find the following expressions for the derivatives of U_0

$$\frac{\partial U_0}{\partial r} = -\sum_m \gamma_m A_m J_1(\gamma_m r)e^{-\frac{\gamma_m^2}{M_2}z} - \int_0^z \sum_m \gamma_m A_m^s J_1(\gamma_m r)e^{-\frac{\gamma_m^2}{M_2}(z-s)}ds$$
$$\frac{\partial U_0}{\partial z} = -\sum_m \frac{\gamma_m^2}{M_2}A_m J_0(\gamma_m r)e^{-\frac{\gamma_m^2}{M_2}z} + \sum_m A_m^z J_0(\gamma_m r) - \int_0^z \sum_m \frac{\gamma_m^2}{M_2}A_m^s J_0(\gamma_m r)e^{-\frac{\gamma_m^2}{M_2}(z-s)}ds$$

Now lets assume for the sake of simplicity that the homogeneous boundary condition at $r = 1$ for the correction term is still a Dirichlet boundary condition (similar to the leading order term), which means that the eigenvalues γ_m do not change between the correction term and the leading order term. Then to find an expression for C_m^s in (A.2), we first need the following expressions

$$\int_0^1 r\frac{\partial U_0}{\partial z}J_0(\gamma_m r)dr = \int_0^1 rJ_0^2(\gamma_m r)dr\left[A_m^z - \frac{\gamma_m^2}{M_2}\int_0^z A_m^s e^{-\frac{\gamma_m^2}{M_2}(z-s)}ds - \frac{\gamma_m^2}{M_2}A_m e^{-\frac{\gamma_m^2}{M_2}z}\right] \tag{A.4}$$

and

$$\int_0^1 r^2\frac{\partial U_0}{\partial r}J_0(\gamma_m r)dr = -\sum_{m'}\gamma_{m'}\int_0^1 r^2 J_0(\gamma_m r)J_1(\gamma_{m'}r)dr\left[\int_0^z A_{m'}^s e^{-\frac{\gamma_{m'}^2}{M_2}(z-s)}ds + A_{m'}e^{-\frac{\gamma_{m'}^2}{M_2}z}\right] \tag{A.5}$$

Next using (A.1) and (A.3), we get

$$C_m^s = \frac{\int_0^1 rp(r,s)J_0(\gamma_m r)dr}{\int_0^1 rJ_0^2(\gamma_m r)dr} \tag{A.6}$$
$$= \frac{\frac{1}{2}g_0'(s)\int_0^1 r^2\frac{\partial U_0}{\partial r}(r,s)J_0(\gamma_m r)dr - g_0(s)\int_0^1 r\frac{\partial U_0}{\partial z}(r,s)J_0(\gamma_m r)dr}{\int_0^1 rJ_0^2(\gamma_m r)dr}$$

Noting that in the axisymmetric case (A.2) simplifies to

$$U_1(r,z) = \sum_m J_0(\gamma_m r)e^{-\frac{\gamma_m^2}{M_2}z}\int_0^z C_m^s e^{\frac{\gamma_m^2}{M_2}s}ds$$

then the final expression we need is

$$\int_0^z C_m^s e^{\frac{\gamma_m^2}{M_2}s}ds =$$
$$-\frac{1}{2\int_0^1 rJ_0^2(\gamma_m r)dr}\left[\sum_{m'}\gamma_{m'}\left(\int_0^1 r^2J_0(\gamma_m r)J_1(\gamma_{m'}r)dr\right)\right.$$
$$\left.\times\left(\int_0^z\int_0^s g_0'(s)A_{m'}^{s^*}e^{\frac{-\gamma_{m'}^2+\gamma_m^2}{M_2}s}e^{\frac{\gamma_{m'}^2}{M_2}s^*}ds^*ds + \int_0^z A_{m'}g_0'(s)e^{\frac{-\gamma_{m'}^2+\gamma_m^2}{M_2}s}ds\right)\right]$$
$$-\int_0^z A_m^s g_0(s)e^{\frac{\gamma_m^2}{M_2}s}ds + \frac{\gamma_m^2}{M_2}\int_0^z\int_0^s A_m^{s^*}g_0(s)e^{\frac{\gamma_m^2}{M_2}s^*}ds^*ds + \frac{\gamma_m^2}{M_2}\int_0^z A_m g_0(s)ds$$

where we have used (A.4), (A.5) and (A.6).